Multiscale Simulation of CO$_2$ Reduction in Solid Oxide Electrolysis Cells

by

Bohua Ren

A thesis

presented to the University of Waterloo
in fulfillment of the
thesis requirement for the degree of
Doctor of Philosophy
in
Chemical Engineering

Waterloo, Ontario, Canada, 2020

Examining Committee Membership

The following served on the Examining Committee for this thesis. The decision of the Examining Committee is by majority vote.

External Examiner	Prof. **Fanglin Che**
	Department of Chemical Engineering, University of Massachusetts Lowell
Supervisors	Prof. **Eric Croiset**
	Department of Chemical Engineering, University of Waterloo
	Prof. **Luis Ricardez-Sandoval**
	Department of Chemical Engineering, University of Waterloo
Internal Member	Prof. **Yuning Li**
	Department of Chemical Engineering, University of Waterloo
Internal Member	Prof. **Zhongwei Chen**
	Department of Chemical Engineering, University of Waterloo
Internal-external Member	Prof. **Holger Kleinke**
	Department of Chemistry, University of Waterloo

Author's Declaration

This thesis consists of materials all of which I authored or co-authored: see Statement of Contributions included in the thesis. This is a true copy of the thesis, including any required final revisions, as accepted by my examiners.

I understand that my thesis may be made electronically available to the public.

Statement of Contributions

The body of this thesis is based upon a combination of published papers. Various chapters are adapted from the following list of publications.

<u>Chapter 3</u> of this thesis consists of the following paper that was co-authored by myself, my supervisors (Prof. Eric Croiset and Prof. Luis Ricardez-Sandoval), two collaborators (Jingde Li and Guobin Wen).

> "First-Principles Based Microkinetic Modeling of CO_2 Reduction at the Ni/SDC Cathode of a Solid Oxide Electrolysis Cell" ***The Journal of Physical Chemistry C***, 2018, 122, 37, 21151–21161. DOI: 10.1021/acs.jpcc.8b05312.

I devised the idea and carried out the calculations and analyses; J. Li and G. Wen reviewed the results and revised the manuscript; E. Croiset and L. Ricardez-Sandoval directed the research.

<u>Chapter 4</u> of this thesis is an unpublished manuscript that was co-authored by myself, my supervisors. I devised the idea and conducted simulations. E. Croiset and L. Ricardez-Sandoval supervised the work.

<u>Chapter 5</u> of this thesis consists of the following paper that was co-authored by myself, my supervisors.

> "A theoretical study on CO_2 electrolysis through synergistic manipulation of Ni/Mn doping and oxygen vacancies in $La(Sr)FeO_3$" ***Journal of Catalysis***, 2020, 383, 273-282. DOI: doi.org/10.1016/j.jcat.2020.01.033.
>
> I devised the idea and conducted simulations. E. Croiset and L. Ricardez-Sandoval supervised this work.

Abstract

Electrochemical CO_2 reduction in solid oxide electrolysis cell (SOEC) is a promising technology to address the global issue of greenhouse emissions. SOEC operates at high temperatures (>873K), possessing high energy efficiency. The products from CO_2 reduction in SOEC, i.e. CO, can be used in the Fischer–Tropsch process by mixing with H_2 (syngas) to produce chemicals and fuels. An efficient cathode electrocatalyst for reducing CO_2 is a pre-requisite in SOEC. However, the main challenges for electrocatalysts are: 1) improvement of the catalytic activity and durability of cathode materials and 2) better understanding of the CO_2 electroreduction mechanism to accelerate the development of SOEC. The objectives of this thesis are to study CO_2 reduction mechanism in SOEC and provide new insights for the design of catalysts through multiscale modelling, i.e. periodic density functional theory (DFT) calculations, microkinetic simulations, and multiphysics modelling. Two different cathode materials were considered in this work: 1) Nickel (Ni)/Samaria Doped Ceria (SDC) and 2) Perovskite La(Sr)FeO$_{3-\delta}$ (LSF).

Ni/SDC has high catalytic activity towards CO_2 electrolysis but suffers from Ni oxidation and carbon deposition. To understand the CO_2 electroreduction mechanism at the three-phase boundary (TPB) of Ni/SDC, two simulation approaches have been performed:

a) DFT combined microkinetic modelling (**Chapter 3**). The effect of oxygen vacancy locations on CO_2 reduction reaction at the TPB have been studied using DFT +U calculations. Based on the DFT results, a micro-kinetic analysis was conducted to determine the rate-controlling step under various SOEC operating voltages at 1000 K. The analysis reveals that interface oxygen vacancy can notably boost CO_2 adsorption and reduction. The rate-controlling step will change from the oxygen spillover step to the CO desorption step with an increase in cathode overpotential on

Ni(111)/SDC surface with non-interface oxygen vacancy. However, CO desorption is the dominating rate-controlling step on Ni(111)/SDC surface with interface oxygen vacancy.

b) DFT based Multiphysics modelling (**Chapter 4**).To further extend the understanding regarding CO_2 electrolysis at of Ni/SDC, the resulting kinetic data from DFT were incorporated into a two-dimensional SOEC multi-physics model. Three reaction mechanisms were proposed to describe the charge transfer steps. The results show that the most likely charge transfer step is $CO_2(s)+(s)+2e^- \leftrightarrow CO(s)+O(s)^{2-}$. Sensitivity analysis results show that CO desorption is the rate-controlling step. The effects of CO/CO_2 ratio and temperature indicates that a temperature of 700 °C or above and CO/CO_2 inlet ratio of 1:1~1:3 are recommended to maintain a low content of carbon deposition, low polarization resistance and high current density.

Compared to Ni/SDC, perovskite $La(Sr)FeO_{3-\delta}$ (LSF) based materials have better coking resistance but lower catalytic activity. To explore the catalytic mechanism and predict active LSF based material, DFT combined microkinetic modelling were also employed (**Chapter 5**). CO_2 adsorption and reduction reaction mechanism were investigated on 12 surface models describing the effects of surface oxygen vacancies and Ni/Mn doping. In particular, a phase diagram was established to find the most stable LSF structure under SOEC operating conditions. Ni-Mn double doping with 2 surface oxygen vacancies of LSF was identified as the most effective electrocatalysts. Experimental studies for this material have yet to be reported in the literature.

Acknowledgements

Contents

List of Figures

List of Tables

Nomenclature

k_m	rate constant for reaction m (cm, mol, s)
A_m	pre-exponential factor for reaction m (cm, mol, s)
c_i	concentration of species i (mol·cm^{-3} or mol·cm^{-2})
D_{ion}	diffusivity of the ionic species (m^2· s^{-1})
D_i^{eff}	effective diffusivity of species i (m^2· s^{-1})
E_m	activation energy (J·mol^{-1})
F	Faraday constant (C·mol^{-1})
G	Gibbs free energy (J·mol^{-1})
ΔG^0	the change of Gibbs free energy at equilibrium state (J·mol^{-1})
i	current density (A·cm^{-2})
J	diffusion flux (kg·m^{-2}·s^{-1})
k	rate constant (cm^3·mol^{-1}·s^{-1})
K	permeability (m)
S_{TPB}	effective triple phase boundary area (m^2·m^{-3})
V	Diffusion volume (m^{-3})
M	molecular weight (g·mol^{-1})
I	identity tensor
P	pressure (Pa)
Q	current source (A·cm^{-3})
r	electrochemical rate (mol·m^{-2}·s^{-1})
r_p	average pore radius (m)
R	gas constant (J·mol^{-1}·K^{-1})
s	species production rate (mol·m^{-2}·s^{-1})
T	temperature (K)
u_{ion}	mobility of the ionic species
W	molecular weight (kg mol-1)
x_i , x_j	molar fraction of gaseous species i and j
z	number of electrons transferred in the electrochemical

Greek symbols

μ_{km}, ε_{km}	coverage dependency of rate constant
α, β	symmetry factor
θ	surface coverage
v_i'	stoichiometric coefficients of products in reaction m
v_i''	stoichiometric coefficients of reactants in reaction m
η	overpotential (V)
u	velocity vector(m·s^{-1})
μ	viscosity (kg·m^{-1}·s^{-1})
v	stoichiometric coefficient
σ	conductivity (S·m^{-1})
t	time (s)
τ	tortuosity
Γ	area-specific density of Ni (mol·m^{-2})
ε	porosity

Subscripts

an	anode
ca	cathode
CT	charge transfer reaction
elec	electronic
elyte	electrolyte
ref	reference
g	gas
i	gas or surface species
ion	ionic
m	reaction

Superscripts

eff	effective coefficient

Chapter 1. Introduction and Motivation

1.1. Background

It is widely accepted that fossil fuels combustion is the main cause of large amounts of CO_2 in the atmosphere that lead to climate change. Among the different options to mitigate CO_2 emissions, CO_2 capture, storage, and utilization technologies are promising solutions to tackle this global problem [1-6]. The present thesis focuses on CO_2 utilization, and more particularly on electrochemical reduction of CO_2 which has recently attracted significant attention as a sustainable future energy technology [7]. In this process, captured CO_2 is electrochemically reduced to CO which can be used in Fischer–Tropsch process by mixing with H_2 (syngas) to produce chemicals and fuels. Compared with other CO_2 conversion strategies (e.g. thermo-catalytic and photocatalytic CO_2 conversion), electrochemical reduction of CO_2 can not only convert CO_2 to fuels [8], but also act as energy storage system for intermittent renewable electricity [9-12] as shown in Figure 1-1.

CO_2 electroreduction includes two main methods: *i)* low temperatures electrolysis (<100°C) in aqueous solutions, *ii)* high temperature electrolysis (>600°C) in solid oxide electrolysis cells (SOECs) [13-16]. SOECs exhibit a low overpotential and superior selectivity to CO formation as well as high current density compared with low temperature CO_2 electroreduction [17, 18]. CO_2 reduction takes place at the triple phase boundaries (TPB) [13, 18, 19] with much lower transport limitation compared to low temperature electrolysis, and also higher operating temperatures result in faster reaction kinetics.

SOEC can also be used for water electrolysis, or combined water and CO_2 electrolysis to produce synthetic gas (i.e. essentially mixture of H_2 and CO). Low temperature alkaline water electrolyzer shows efficiencies exceeding 80% [20, 21]; in comparison, energy efficiencies around 98% are

reported for water electrolysis in SOEC operating at 650 °C [20, 22]. On the other hand, high temperature electrolysis is more cost-effective than lower temperature technologies (~66% lower total cost) [20, 23]. Therefore, solid oxide electrolysis for CO_2 and/or water reduction is a promising technology. However, the catalytic activity and stability of cathode materials are still not sufficient for practical implementation and commercialization, which still need to be further developed.
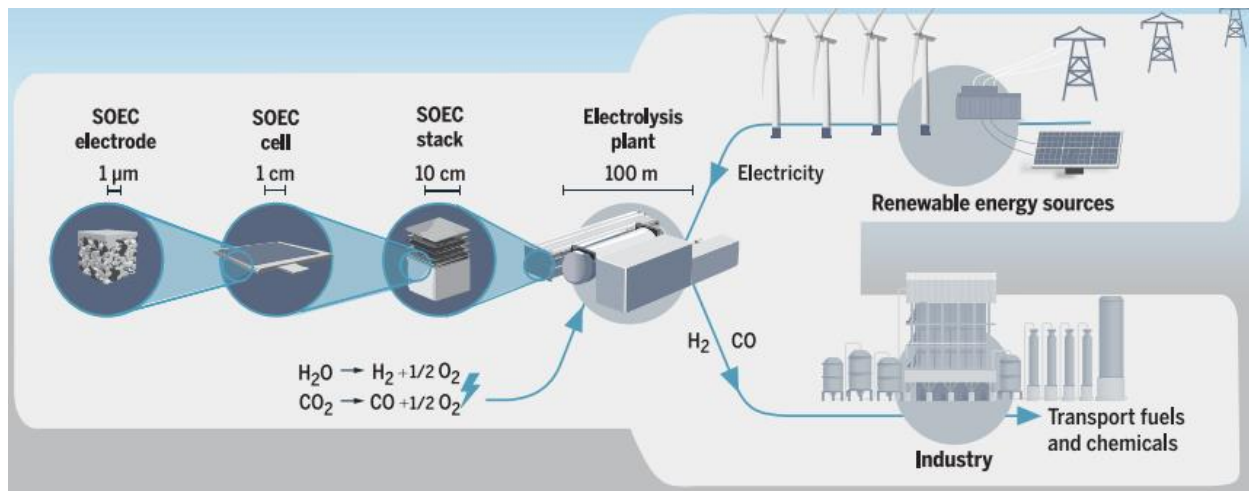
Figure 1-1. SOEC based on renewable energy [6].

SOEC corresponds to the reverse operation of a solid oxide fuel cell (SOFC). Figure 1-2 presents a schematic of (a) solid oxide fuel cell (SOFC), (b) solid oxide electrolysis cell (SOEC) (CO_2 and H_2O co-electrolysis process). The process of CO_2 reduction to CO by using the intermittent renewable electricity in SOEC is shown in Figure 1-2 (c), which can be coupled with CO_2 capture process from power plant [24, 25]. The materials used for solid oxide electrolysis cells are similar to those used for SOFCs [8]. Typical electrolytes contain zirconia-based oxides, ceria-based oxides and lanthanum gallates-based oxides [13]. Due to its high catalytic activity and relatively low cost, conventional nickel/yttria-stabilized zirconia (Ni/YSZ) composites are widely used as cathode materials in SOEC [26, 27].
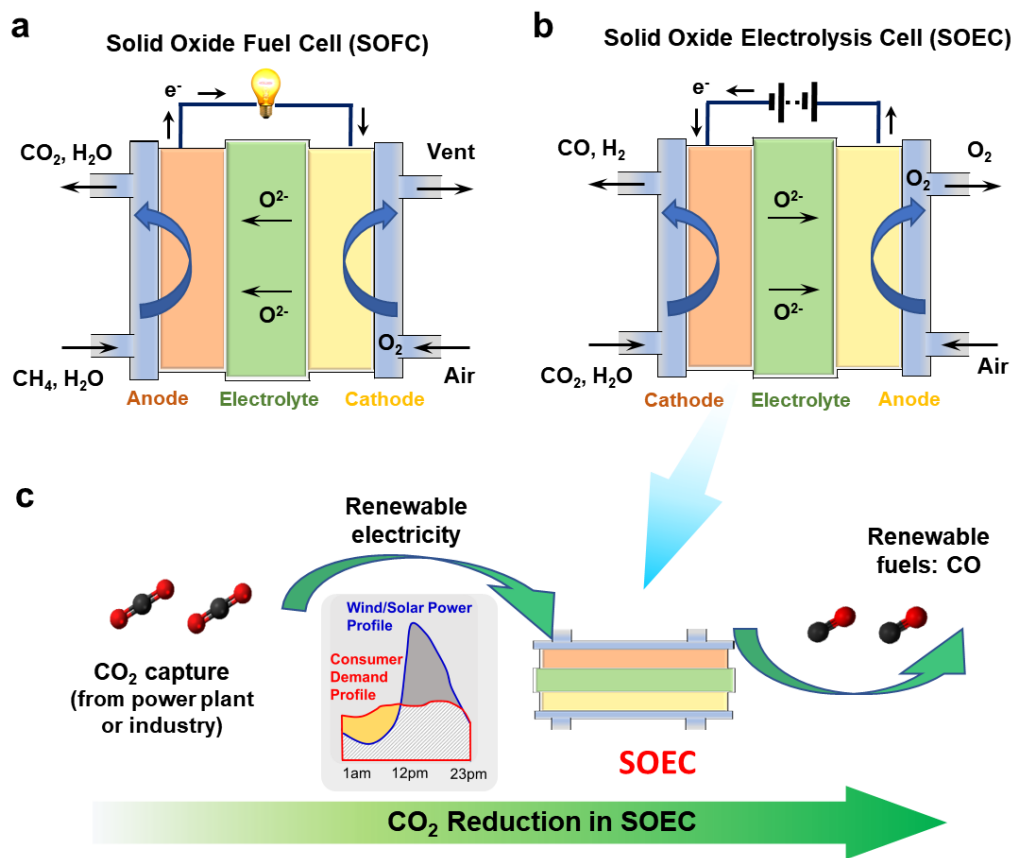
Figure 1-2. Schematic of (a) solid oxide fuel cell (SOFC), (b) solid oxide electrolysis cell (SOEC) and (c) CO_2 reduction to CO process in SOEC.

Ni ensures good electronic conductivity and electrocatalytic activity towards CO_2 and water electrolysis while YSZ provides ionic conductivity. Compared to YSZ, ceria-based electrolyte such as samarium-doped ceria (SDC) and gadolinium-doped ceria (GDC) exhibit higher ionic conductivity at intermediate temperatures (600-750°C) [28-30]. However, these cathodes suffer from severe electrical conductivity loss and deactivation because of the easy re-oxidation of Ni (Ni $\rightarrow$ NiO) and carbon deposition in an atmosphere with highly concentrated CO_2/CO [31]. Perovskite oxides, which takes the form of ABO_3, have been proven to be the most promising replacement to the conventional Ni/YSZ cermet in SOECs [13]. The A-site is usually occupied by rare earth metal ions such as La^{3+}, Gd^{3+}, and Pr^{3+} whereas the B-site is often occupied by small tri- or tetravalent

3

3d transition metal ions, e.g. Fe^{3+}, Co^{3+}, Ni^{3+} [19]. Perovskite oxides are most widely used in the oxygen electrode of solid oxide cells to act as catalysts of oxygen reduction reaction (SOFC) and oxygen evolution reaction (SOEC). In principle, almost all perovskite composite oxides have the potential to be used as cathode materials in SOECs for CO_2 electrolysis because of their property of mixed ionic and electronic conductivity. However, considering the catalytic activity and chemical stability under the condition of electrochemical reduction of CO_2, only a few types of perovskite oxides have been investigated in detail, including $La_{1-x}Sr_xCr_{1-y}Mn_yO_{3-\delta}$, $(Ln_xSr_{1-x})_yTiO_{3-\delta}$ (Ln= lanthanide), $La_{1-x}Sr_xFeO_{3-\delta}$, and other double perovskites such as $PrBaMn_2O_{5+\delta}$, $PrBa_{0.5}Sr_{0.5}Co_{1.5}Fe_{0.5}O_{5+\delta}$, $Sr_2Mg_{1-x}Mn_xMoO_{6-\delta}$, or $Sr_2FeMo_{0.65}Ni_{0.35}O_{6-\delta}$ oxides [13]. Since CO_2 reduction takes place on the SOEC cathode, the focus of this thesis is on the cathode.

1.2. Motivation & Challenges

The prerequisites for being an ideal cathode material for CO_2 electrolysis in high temperature SOEC are: (1) excellent catalytic activity towards CO_2 conversion, (2) good compatibility with electrolyte materials, (3) good coking resistance and long durability, (4) high electrical conductivity to provide electrons for CO_2 reduction and high oxygen ionic conductivity, and (5) porous structure for gas diffusion [31].

The conventional metal–ceramic materials (e.g. Ni/YSZ and Ni/SDC) shows high catalytic activity for the conversion of CO_2 to CO but suffers from Ni oxidation and carbon deposition, leading to the loss of electronic conductivity and cell degradation during high temperature CO_2 electrolysis. Compared to YSZ, SDC exhibits higher ionic conductivity at intermediate temperatures (600-750℃). Thus, Ni/SDC is chosen to be one of the research topics in this thesis. Although many experimental studies have been performed to advance the performance of Ni/SDC in CO_2

4

electrolysis[28-30, 32-34], additional theoretical studies are needed to reveal the unknown CO_2 electroreduction mechanisms, which play a significant role in improving SOEC performance[18], e.g. rate controlling step, oxygen ion conduction, the effects of oxygen vacancy location, charge transfer step and carbon deposition distribution. Perovskite-type oxides have been proven to be the most promising replacement of convential metal–ceramic materials in SOEC. $La_{0.6}Sr_{0.4}FeO_{3-\delta}$ based perovskite oxides (LSF) have been chosen to be the another research topic in the present work because they have shown enhanced coking resistance and good compatibility with electrolyte materials (YSZ or SDC). The perovskites can resist carbon deposition but have lower catalytic activity and faces the problem of segregation of alkaline earth elements. Detrimental effects of such segregation on electrode performance or stability have been experimentally observed, particularly in many Sr-containing materials. Therefore, exploring new $La_{0.6}Sr_{0.4}FeO_{3-\delta}$ based electrocatalysts with both high catalytic activity and stability is still a key challenge. Ni or Mn doped $La_{0.6}Sr_{0.4}FeO_{3-\delta}$ shows high performance as cathode materials for CO_2 electrolysis in SOEC [35-37]. However, the functional mechanism of Ni or Mn doping in $La_{0.6}Sr_{0.4}FeO_{3-\delta}$ on CO_2 electrolysis have not been studied yet, which hindered further exploration of new materials with higher catalytic activity in SOEC. Revealing theoretical insights for the design of this cathode material is important for the development of SOEC.

Nevertheless, modelling the behavior of a SOEC system is challenged by its multiscale nature. Different modelling methods are currently available to describe phenomena occurring at different scales [38-45]. In particular, Density Functional Theory (DFT) based on quantum chemistry attracted extensive research for its capability to study the electronic properties of materials and reaction pathways [46-50]. Micro-kinetic modelling can be used to explore the reaction mechanism (e.g. rate controlling step) under realistic conditions at the micro-scale level [51-55]. Moreover,

multiphysics modelling based on Finite Element Method can be employed to predict the system's performance at the macro scale (e.g. spatial distribution of adsorbate species and current density, inlet gas ratio, applied voltage and temperature effects, etc.) [56-59]. Coupling of these approaches (e.g. DFT based micro-kinetic, DFT based multiphysics modelling) is instrumental to gain new insights that are never reported for CO_2 electrolysis in SOEC.

1.3. Research Objectives

The research objective of this thesis is to provide new insights for the computer aided catalyst design for high temperature CO_2 electrolysis with the aim to reveal reaction mechanism and corresponding kinetic parameters, as well as designing new cathode materials with enhanced catalytic activity. This thesis considers two different routes to design SOEC cathode materials: 1) Ni/SDC-based and 2) perovskite-based.

The specific research objectives pursued in this research are as follows:

1. Elucidate CO_2 electroreduction mechanism for Ni/SDC by developing a multi-scale model consisting of DFT simulations (electronic level), microkinetic modelling (micro level), multiphysics modelling (macro level), as shown in Figure 1-3:

    a) Examine the effect of oxygen vacancy locations on CO_2 reduction reaction using DFT +U calculations, which is critical for improving the performance of SOEC due to the significant role of oxygen vacancy in ionic conductivity and CO_2 adsorption.

    b) Determine the rate-controlling step under SOEC operating conditions using a micro-kinetic analysis using the DFT kinetic data for all the elementary steps occurring in TPB.

    c) Study the charge transfer step, dominant species and carbon deposition distribution by conducting a 2D multi-physics SOEC model (Figure 1-3) using the kinetic data calculated

by DFT along with coupled elementary chemical and electrochemical reactions, ionic/electronic conduction, and transport processes.

2. Predict active perovskite $La_{0.6}Sr_{0.4}FeO_{3-\delta}$-based cathode materials by developing a DFT-based microkinetic modelling:

   a) Investigate CO_2 adsorption and reduction reaction mechanism on $La(Sr)FeO_{3-\delta}$ based surface models in Figure 1-3 describing the effects of surface oxygen vacancies and Ni/Mn doping or co-doping by DFT+U calculations. In particular, to establish a phase diagram in order to find the most stable LSF structure under SOEC operating conditions.

   b) Develop a microkinetic model, simulate polarization curves and compare with experimental data of pure LSF.
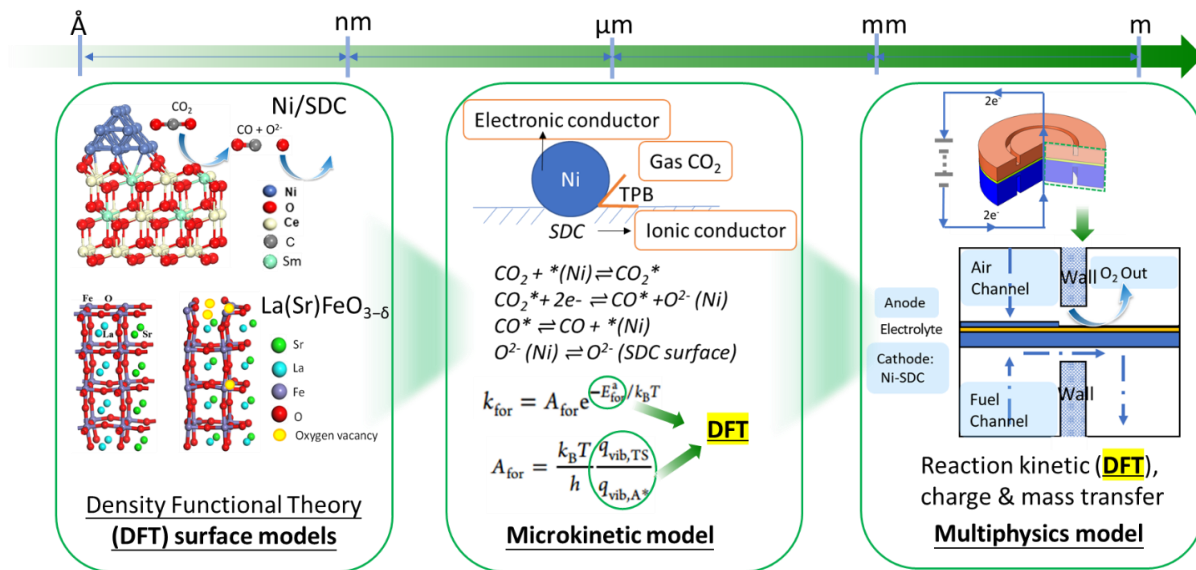
Figure 1-3. Multi-scale modelling of CO_2 electrolysis in SOEC in this thesis.

1.4. Research Contributions

This thesis aims to advance theoretical insights into high temperature CO_2 electroreduction mechanism on conventional Ni/SDC and $La(Sr)FeO_{3-\delta}$ based materials by performing a multi-scale

modelling analysis and predicting new La(Sr)FeO$_{3-\delta}$ based materials with high catalytic activity. The research contributions of this work are as follows:

(a) By developing a multiscale model, the charge transfer reaction for CO$_2$ electroreduction on Ni/SDC was identified; in particular, CO$_2$(Ni)+(Ni)+2e$^-$↔CO(Ni)+O(Ni)$^{2-}$. This is different from previous reported studies that used O^{2-} spillover from Ni to electrolyte, which we found less likely.

(b) Development of a CO$_2$ electroreduction 2D multiphysics model that incorporates microkinetics, whose parameters were obtained from DFT for all the elementary steps on Ni/SDC, and where only 2 sticking coefficients and one pre-exponential factor were determined through fitting experimental data. This model relies on fewer fitted parameters than previously reported models, while accurately matching experimental results over a wider range of operating conditions.

(c) For the first time, the functional mechanism of doping elements Ni and Mn, and their effects during CO$_2$ reduction on the catalytic activity and on oxygen vacancy formation and migration were reported in La(Sr)FeO$_{3-\delta}$ based materials using DFT calculations.

(d) By combining DFT and microkinetic modelling, it was proposed that Ni-Mn double doping with 2 surface oxygen vacancies of LSF is a more effective electrocatalysts than single Ni or Mn doping, and should be investigated experimentally.

1.5. Organization of the Thesis

This thesis is organized as follows: the literature review related to conventional metal–ceramic, perovskite-type oxides cathode materials for CO$_2$ electrolysis in SOEC, and the multiscale modelling methods are presented in **Chapter 2**.

In **Chapter 3**, CO$_2$ electroreduction mechanism on Ni/SDC surface was studied by combining DFT

and micro-kinetic analysis. Effects of oxygen vacancy locations on CO_2 reduction reaction were studied at Ni(111)/SDC surface using periodic DFT+U calculations. A micro-kinetic analysis was developed to determine the rate-controlling step under various solid oxide electrolysis cells operating voltages at 1000 K. Outcomes from this work has been published in ***The Journal of Physical Chemistry C*** [52].

In **Chapter 4**, a 2D DFT-based multiphysics model is presented to reveal some properties of high temperature CO_2 electrolysis at the macro scale using the kinetic data calculated by DFT for Ni/SDC. The aim is to identify the most likely charge transfer step, spatial distribution of adsorbate species, current density, inlet gas ratio, applied voltage and temperature effects.

In **Chapter 5**, CO_2 electroreduction mechanism at La(Sr)FeO$_3$-based cathode in SOEC was studied by combining DFT with a micro-kinetic analysis. Catalytically active species typically reside on the B-site (transition metal sites) of perovskite. Thus, for the B-site, this work focused on the functional mechanism of doping elements Ni and Mn and its effect during CO_2 reduction on the catalytic activity and on oxygen vacancy formation and migration. A micro-kinetic model was developed to determine which dopants achieve the best performance (i.e. highest current density under the same voltage). This is done by simulating polarization curves and comparing with experimental data reported for pure LSF. Outcomes from this work has been published in ***Journal of Catalysis[49]***.

Chapter 6 summarizes the conclusions from this research and outlines future areas of development for this research.

Chapter 2. Literature Review

For the cathode materials of CO_2 electrolysis in SOEC, the most important properties are the catalytic activity, durability, electrical conductivity, and ionic conductivity. Therefore, in this Chapter, with the end goal of multiscale modelling for CO_2 electrolysis at Ni/SDC and La(Sr)FeO$_3$-based based cathode materials in SOEC, a brief review on Ni/YSZ and SDC is presented; in particular, as well as electronic and ionic conduction as well as reported strategies to solve the carbon deposition problem are reviewed since they represent the main challenges in Ni-ceramic materials. The composition, mechanisms of electronic and ionic conduction of perovskite-type materials are reviewed. The current reported strategies used to improve the reactivity of perovskite materials in SOEC are also presented which is the main challenge of perovskite materials. Multiscale modelling can provide new insights for the computer aided catalyst design for high temperature CO_2 electrolysis with the aim to reveal reaction mechanism and predict catalysts' activity. Therefore, a review on multiscale modelling approaches was performed; in particular, those that involve DFT simulation, microkinetic modelling and finite element method studies in solid oxide cells.

2.1. Conventional Metal–ceramic Cathode Materials

SOEC includes electrolyte for ionic transport, anode for the evolution of oxygen and cathode for the electrochemical reduction of CO_2. Conventional metal-ceramic mixtures, e.g. Ni/YSZ and Ni/SDC composites are the most widely used cathode material in SOEC due to its high catalytic activity[15, 16]. For example, the electrochemical performance of CO_2 electrolysis in the microtubular SOEC were reported at different temperatures and various CO_2/CO inlet ratios with Ni/SDC as shown in Figure 2-1 [60]. It can be seen that increasing the temperature from 700°C to

800°C and decreasing the ratio of CO:CO₂ from 2:1 to 1:9, the SOEC performance was improved. The current density could reach approximately 1.5 A·cm² at 1.6 V and 800°C with molar ratio CO/CO₂ of 1. The electrolysis performance of pure CO_2 inlet was lower than those with other gas compositions likely because of partial oxidation of nickel surface in high CO_2 concentration.
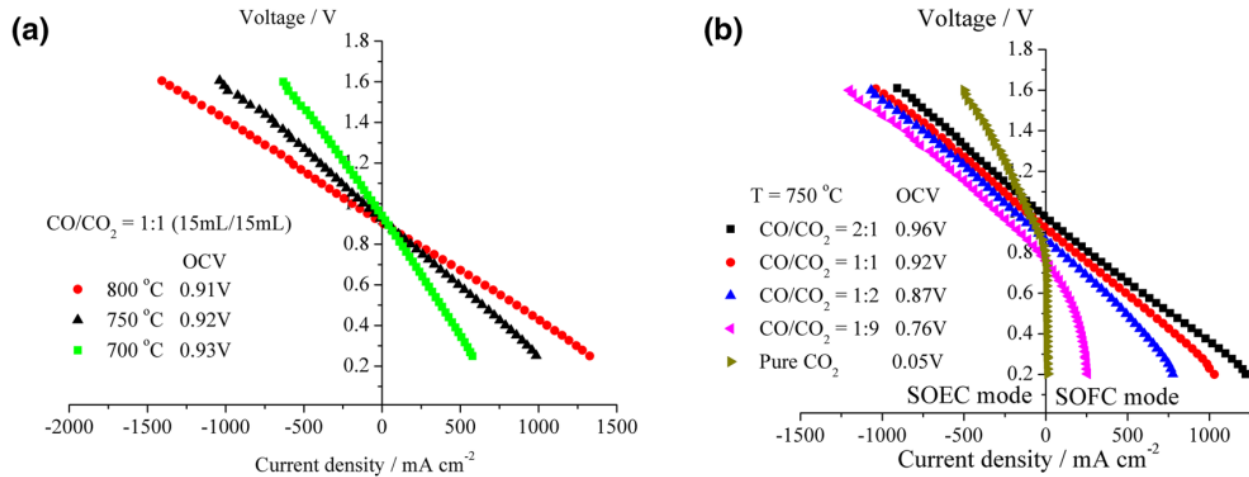
Figure 2-1. Polarization curves of Ni–SDC/YSZ/SDC/ PrBaCo₂O₅₊δ (PBCO) cell under (a) various temperatures at CO/CO₂ ratio of 1; (b) various CO/CO₂ ratios at 750°C [60].

2.1.1. Electronic and Ionic Conduction

In SOEC, with the use of electricity, CO_2 is electrochemically reduced to CO and produce one oxygen ion, which migrates through the electrolyte and transforms into oxygen gas in the anode. Thus, the electrode material should have both high electric and ionic conductivity. The reactions on both anode and cathode take place at the TPB which comprise oxygen ionic conductors, electronic conductors, and the reactant gases. In conventional metal-ceramic mixtures, the metal component provides the electrical conductivity while the ceramic material provides the ionic conductivity of the cathode. Ni-ceramic material in porous fuel electrode is widely used for solid oxide cell applications due to its high electrocatalytic activity, low cost, and appropriate coefficient of thermal expansion (CTE) (in the range $10.0 \sim 12.5 \times 10^{-6}$ K⁻¹) [19, 61]. Ni has good electronic

conductivity of 10^4 S·cm^{-1} at 1123 K [62]. YSZ, a solid solution of around 8% molar ratio of yttria (Y_2O_3) in zirconia (ZrO_2), remains the electrolyte material of choice in solid oxide cells with a satisfactory oxygen-ion conductivity and suitable chemical/physical stability at high temperatures [6, 20]. Figure 2-2 summarizes the ionic conductivity of YSZ and other ion conducting materials used in SOEC such as other zirconia-based, ceria-based, LaGaO$_3$-based, and proton conduction BaCe$_{0.9}$Yb$_{0.1}$O$_{3-\delta}$ [20]. From this figure, one can observe that, when compared to YSZ, ceria-based electrolyte such as samarium-doped ceria (SDC) and gadolinium-doped ceria (GDC) exhibit higher ionic conductivity at intermediate temperatures (600-750°C) [28-30]. The partial reduction of ceria from Ce^{4+} to Ce^{3+} under a reducing atmosphere is accompanied by the appearance of electronic conductivity [13], which is beneficial for a cathode materials but detrimental as electrolyte materials because of partial internal electronic short circuit in the cell.
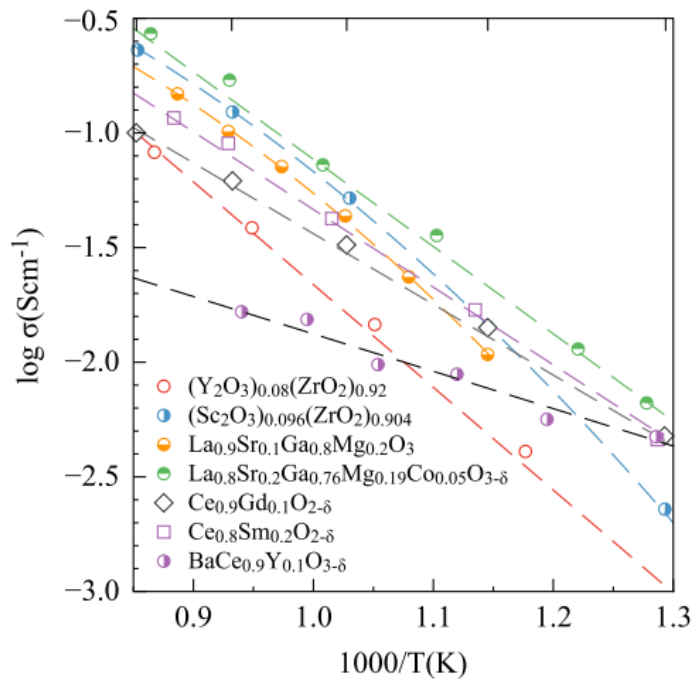
Figure 2-2. Ionic conductivity of electrolyte materials in SOEC [20].

The formation, migration and association of oxygen vacancies dominate the ionic conductivity in

SOFC and SOEC [63-70]. The hopping of charge carrier, i.e. O^{2-}, causes oxide ion conduction. The diffusion of the oxide ion through the lattice can be expressed as follows [71]:

$$D_{O^{2-}} \sim [V_O^{\cdot\cdot}] \cdot a^2 \cdot exp^{-(\Delta H_f + \Delta H_m + \Delta H_a)/RT} \qquad (2\text{-}1)$$

This equation shows that oxide ion diffusion is proportional to the concentration of oxygen vacancies, $[V_O^{\cdot\cdot}]$, the square of the lattice parameter, a, and related with three main processes: formation (ΔH_f), migration (ΔH_m), and association (ΔH_a) of vacancies.

Oxygen vacancy sites can bind adsorbates more strongly than normal oxide sites, and therefore promote adsorbate dissociation in metal oxides catalysts [72]. For example, the interface oxygen vacancy site in Ni/YSZ cermet can enhance the electrochemical reaction in SOFC by allowing H atoms to spillover from the Ni cluster to the Ni/YSZ interface [73]. Moreover, studies of Ni catalyst deactivation in SOFC have shown that CH is more likely trapped at the interface oxygen vacancy at the TPB region of the Ni/YSZ model rather than at the surface of the Ni cluster [74, 75]. These results indicate that surface oxygen vacancies, especially interface oxygen vacancy at the Ni/cermet have significant effects on the catalytic activity of the electrode materials.

2.1.2. Carbon Deposition Problem

Conventional Ni-ceramic materials suffer from a carbon deposition problem that negatively affects the electrode performance because carbon formation and accumulation can block the active sites on Ni and therefore reduce the production of the desired product [32-34]. During CO_2 electrolysis, carbon forms via the disproportionation of CO through the Boudouard reaction ($2CO \rightleftharpoons C + CO_2$)[28].

Different strategies can be employed to diminish the carbon formation, e.g. modification of the traditional Ni/YSZ cermet or using mixed ionic and electronic conductors (perovskites). Table 2-1

13

presents a summary of modification of Ni/YSZ, Ni/GDC and Ni/SDC cermets to address coking poisoning in SOFC. The information provided in Table 2-1 indicates that current strategies to address coking poisoning always have some drawbacks. For example, the addition of Cu in Ni/YSZ increases coking resistance, but this material has lower conductivity . Nano-composite Sn doped Ni/GDC [76] and infiltration of perovskites $BaZr_{0.9}Yb_{0.1}O_{3-\delta}$ and $BaZr_{0.1}Ce_{0.7}Y_{0.1}Yb_{0.1}O_{3-\delta}$ in Ni/SDC [32-34] demonstrated higher coking resistance, but those materials are still not fully resistant to coking. CeO_2 promotes coking resistance of Ni but suffers degradation [77-79].

Table 2-1. Summary of modification of Ni/YSZ cermet to address coking poisoning.

Modification	Benefits	Drawbacks	Ref.
NiCu/YSZ or Cu/YSZ	Cu resists coking formation better than Ni	Lower conductivity; operation at temperature (<700 °C) needed to prevent agglomeration of particles	[77, 80, 81]
Nano-composite Sn doped Ni/GDC	Suppressed carbon deposition, improved cell performance due to its excellent microstructure	Still a small amount of carbon deposition	[76]
Substitution of YSZ by scandia-doped zirconia oxide (Ni/ScSZ)	Improved conductivity	ScSZ has high cost limits application	[77, 82]
Ceria with Ni (Ni/ CeO_2)	CeO_2 promotes coking resistance	Degradation of a CeO_2	[78, 79]
Cu and CeO_2 instead of Ni (Cu/CeO_2/YSZ)	Good electro-catalytic performance and coking resistance	CeO_2 degradation and low temperature of operation due to Cu use	[77-79]
Copper, CeO_2 and cobalt instead of Ni and YSZ (Cu/CeO_2/Co), or NiCo/YSZ	Good electro-catalytic activity	Higher polarization resistance associated	[83]
Gadolinia-doped ceria	Higher performance	GDC is not as an effective sulfur	[84, 85]

with Ni(Ni/GDC)	compared to Ni–YSZ electrode	absorbent as CeO_2.; sulfur tolerance enhanced by higher GDC content which compromises electron transfer, increasing polarization overpotential	
Ni/SDC infiltration of perovskite ($BaZr_{0.9}Yb_{0.1}O_{3-\delta}$) or $BaZr_{0.1}Ce_{0.7}Y_{0.1}Yb_{0.1}O_{3-\delta}$	Higher performance and conductivity and improved performance and diminished coking formation	Not fully resistant to coking formation	[32-34]

Other than the modifications listed by in Table 2-1, Ru, Mo [86], W, Pd [87] and Rh doped Ni-based cermet have also been reported to improve the coking resistance [88]. These modifications involve expensive noble metals which are beyond the scope of this research. The carbon deposition problem of conventional Ni-ceramic materials also triggered the use of other type of materials like perovskite, which has higher coking resistance and is stable at high temperatures with mixed ionic and electronic conductivity.

Besides the experimental studies reviewed in this section, simulation studies for conventional metal-ceramic materials were also reviewed and are presented in Section 2.3 Multiscale Modelling.

2.2. Perovskite-type Oxides

Ni-based materials have drawbacks in terms of significant catalytic activity to promote coke formation from hydrocarbons and CO_2 as well as low redox stability [89]. Mixed ionic and electronic conducting perovskites have been exploited as alternative SOFC anode materials. Perovskites present higher compatibility, stability, and coking tolerance compared to metal components under various fuels conditions [90-96]. Therefore, perovskite oxides are excellent candidate to be used as SOEC cathode materials. However, compared with Ni/YSZ or Ni/SDC, perovskite oxides show lower catalytic activity [31, 97]. Hence, it is highly desirable to develop

catalysts with high catalytic activity capable of efficient conversion of CO_2 into CO.

The general chemical formula for perovskite crystals is ABX_3 (also referred to as "113", named from A: B: X atomic ratios) as shown in Figure 2-3. In SOEC/SOFC field, the A-site of the perovskites is usually occupied by rare earth metal ions, such as La^{3+}, Gd^{3+}, and Pr^{3+} while the B-site is often occupied by small tri- or tetravalent 3d transition metal ions, e.g., Fe^{3+}, Co^{3+}, Ni^{3+} [19]. X site is usually the oxygen atom.
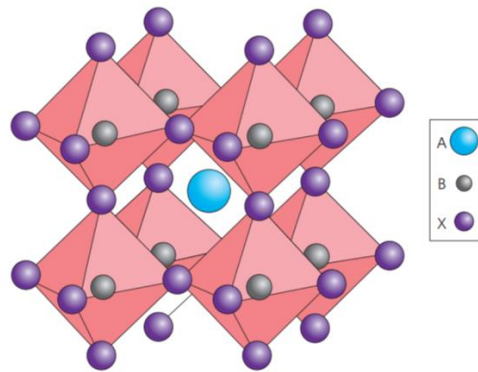
Figure 2-3. The crystal structures of perovskite (ABX_3) [98].

$LaFeO_3$ based perovskite oxides have been extensively investigated as electrodes for both SOFCs and SOECs. The CTE of $La_{0.8}Sr_{0.2}FeO_3$ is 12.2×10^{-6} K^{-1}, which is very close to the CTE of electrolyte materials YSZ or SDC (in the range $10.0 \sim 12.5 \times 10^{-6}$ K^{-1}) [61], indicates that $LaSrFeO_3$ has very good compatibility with electrolyte materials and has potential for extending the thermal cycling of solid oxide cells.

Tatsumi et al. investigated many oxide materials with different structures as cathode materials for CO_2 electrolysis, as shown in Figure 2-4 [99]. That study showed that $La_{0.6}Sr_{0.4}FeO_{3-\delta}$ perovskite presented a much higher electrocatalytic activity than the other materials studied in their work [99]. This is probably due to the high mixed ionic and electronic conductivity and surface activity for the electrochemical dissociation of CO_2 [35]. On the other hand, the electrochemical performance

of these materials is still poor compared to Ni-based materials because of their limited number of active sites (low electrocatalytic activity and insufficient electrical conductivity).
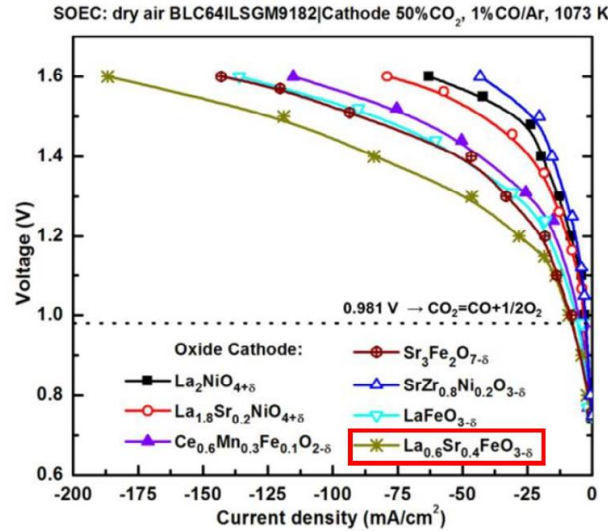
Figure 2-4. I-V curves for the cells using various oxide cathodes at 1073K [99].

To improve the performance of cathode materials, strategies such as A-site and B-site doping, and nanostructured cathode fabrication by *in situ* exsolution, have been explored [89]. Those strategies will be described in the following sections.

2.2.1. Mechanism of Electronic and Ionic Conductions

The development of perovskite materials with mixed electronic and ionic conduction (MIEC) is of great interest for the advance of high temperature electrochemical devices. A better understanding of the mechanism that enables electronic and ionic conduction is key for designing new perovskite materials with enhanced electronic and ionic conductivity.

Electronic conduction: Generally, electronic conduction in perovskites occurs through the B-site of perovskite because B-sites are occupied by cations that are able to adopt multiple oxidation states (e.g., Ti^{4+}/Ti^{3+}, Nb^{5+}/Nb^{4+}, Mn^{4+}/Mn^{3+}, etc.) [36, 37, 100]. Conduction most likely occurs because of electron hopping from low valence cations ($B^{(n-1)+}$) to high valence (B^{n+}) cations via

oxygen bridges, as shown schematically in Figure 2-5(a) and (b). The electronic conductivity is defined in the following equation [64]:

$$\sigma_{e^-} = [B_B'] \cdot e \cdot \mu_{e^-} \qquad\qquad (2\text{-}2)$$

where $[B_B']$ represents the concentration of a B-site ion sitting on a B-site lattice site with single negative charge; e represents the charge of one electron, i.e. 1.602×10^{-19} C. μ_{e^-} is the mobility of the electron charge carriers (e^-). The higher the concentration, $[B_B']$ and higher μ_{e^-}, the higher the conductivity, σ_{e^-} [101-103]. The transfer of electrons is usually promoted by appropriate doping and/or by exposing the materials to a reducing environment which removes oxygen ions from the structure and subsequently reduces B^{n+} to $B^{(n-1)+}$, as described in the following equation:

$$2B_B^X + O_O^X \leftrightarrow 2B_B' + V_O^{\cdot\cdot} + \frac{1}{2}O_2 \qquad\qquad (2\text{-}3)$$

B_B^X and O_O^X are B-site metal ion and oxygen ion on a regular B-site and oxygen lattice site of perovskite, respectively. The prime on the B_B' indicates a decrease in the charge relative to the original B site. $V_O^{\cdot\cdot}$ is an oxygen vacancy.

Ionic conduction: The ionic conductivity of perovskite also involves diffusion of the oxide ion through the lattice as expressed by equation 2-1. When the oxide ion starts hopping from its position, it need to break the bond connected with the adjacent B cations (the A-O bonds are generally very weak compared to the B-O bonds) as shown in Figure 2-5(c) [64, 71, 104].
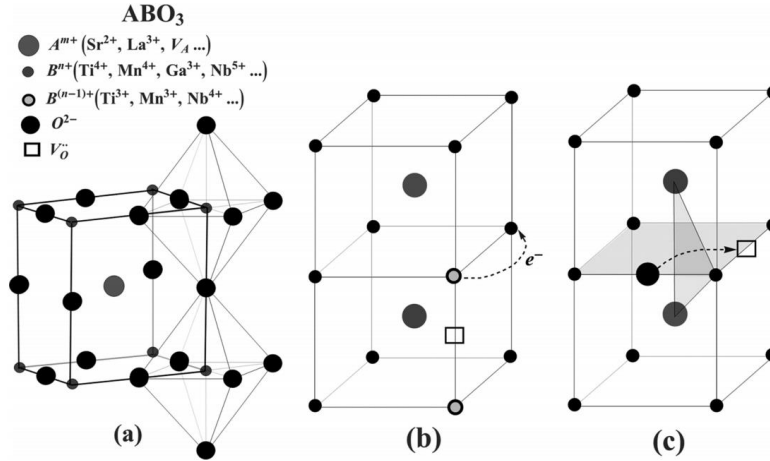
Figure 2-5. (a) Unit cell of perovskite-type oxide together with some typical cations that occupy the A and B sites. (b) Schematic view of the electronic conduction in perovskites. The oxygen lattice is omitted for clarity. (c) Schematic view of the oxide ion conduction in perovskites. Most of the oxygen ions are omitted for clarity [64].

In addition, when the bond breaks the corresponding B cation will decrease its coordination number from 6 to 5. The energy required for the formation of the vacancy ΔH_f is higher when B-O bond is stronger. Some cations, e.g. Mn, Co and Ga are known to be stable in coordination numbers lower than 6 [71] and have been successfully used in perovskites with good electronic and ionic conduction [64, 105].

2.2.2. A-site Doping

Doping chemistry is a promising way to adjust and improve the electrochemical activity and stability of electrode materials for SOECs. In order to increase the electronic and/or ionic conductivity of perovskite oxides, the ions in the A-site can be partially substituted by alkaline earth metal ions such as Ca^{2+}, Sr^{2+}, and Ba^{2+}. When the A-site ion is partially substituted by another ion, oxygen vacancy trapping can occur, mostly because of size mismatch between the host and the substitution ion [106, 107]. Where the size of the host and dopant are similar, for example, when substituting Sr^{2+} (1.44 Å) for La^{3+} (1.36 Å) in lanthanum gallates, ΔH_a (the association of

vacancies) has been calculated to be zero [106] which leads to high ionic conductivity.

Both the electrical conductivity and catalytic activity of lanthanum manganite ($LaMnO_3$) are enhanced considerably when La is substituted partially with Sr ($La_{1-x}Sr_xMnO_{3-\delta}$) [108]. At lower oxygen partial pressures (e.g., $<10^{-10}$ Pa at 900 °C for x = 0.2) [109], the oxides become oxygen deficient and the charge compensation of the positive effective charges of $V_O^{\cdot\cdot}$ is maintained by Mn reduction. The electronic and oxygen-ionic conductivity of $LaFeO_3$ can be enhanced by doping the A site with Sr^{2+}: a moderate amount of dopant increases the concentration of mobile oxygen vacancies and p-type charge carriers, whereas a Sr^{2+} content above 50% results in vacancy clustering, with a detrimental effect on the performance of the material [110].

In summary, A-site can be doped by a variety of cations such as Ca^{2+}, Sr^{2+} and Ba^{2+}. However, for La-based perovskite ($La_{0.6}Sr_{0.4}FeO_{3-\delta}$), Sr is the most widely used A-site doping element due to the high ionic conductivity of Sr doping La-based perovskite. Thus, this research only focused on Sr-doped $LaFeO_3$.

2.2.3. B-site Doping and Exsolution

B-site can be partially substituted by transition metals such as Ni [35], Mn [36], Cr [91] or Fe [35]. If Fe is partially substituted with Ni ($La_{0.6}Sr_{0.4}Ni_{1-x}Fe_xO_{3-\delta}$), especially when x > 0.5, this material shows a high electronic conductivity and thermal expansion coefficient that are close to those of the YSZ electrolytes [111]. The high mixed ionic and electronic conductivity, good compatibility with electrolytes and thermal stability of $La_{0.6}Sr_{0.4}Ni_{1-x}Fe_xO_{3-\delta}$ make it a potential electrode for SOFC.

Luo et al. [35] developed a new Ni-doped $La(Sr)FeO_{3-\delta}$ material, which has been initially designed as a cathode for CO_2 electrolysis in a solid oxide electrolysis cell (SOEC). The ultra-low total

polarization resistance, together with an impressive current density of 1.21 A·cm^2 at 1.55 V and 850°C, demonstrates the superior electrocatalytic activity of $La_{0.6}Sr_{0.4}Fe_{0.8}Ni_{0.2}O_{3-\delta}$ (LSFN) for effectively promoting the cathodic kinetics for the CO_2 electrolytic reaction.

Tatsumi et al. [36] found that $La_{0.6}Sr_{0.4}Fe_{0.8}Mn_{0.2}O_{3-\delta}$ material as cathode shows much higher activity and selectivity toward CO_2 electrolysis than that of LSF and was able to achieve a current density of CO_2 electrolysis of 0.52 A·cm^2 at 1.6 V and 1173 K. Compared with $La_{0.6}Sr_{0.4}FeO_{3-\delta}$ without B-site doping, the performance has been improved. In contrast, substitution of Co, Cu, and Ni decreases the cathodic performance of $LaFeO_3$ resulting in a decrease in electrolysis current as shown in Figure 2-6.

Ye et al. [37] employed synergistic control of A-site deficiency and B-site dual doping strategy to tune $LaSrTiO_{3-\delta}$ cathode surface structures, the resulting optimized $(La_{0.2}Sr_{0.8})_{0.95}Ti_{0.85}Mn_{0.1}Ni_{0.05}O_{3-\delta}$ showed good stability with 100 h operation and 10 redox cycles at 800°C. The excellent performance is attributed to: (*i*) dopant Mn promotes the formation of oxygen vacancies which may facilitate the adsorption of CO_2 and (*ii*) dopant Ni provides metal nanoparticle exsolution promoting the catalytic activity.
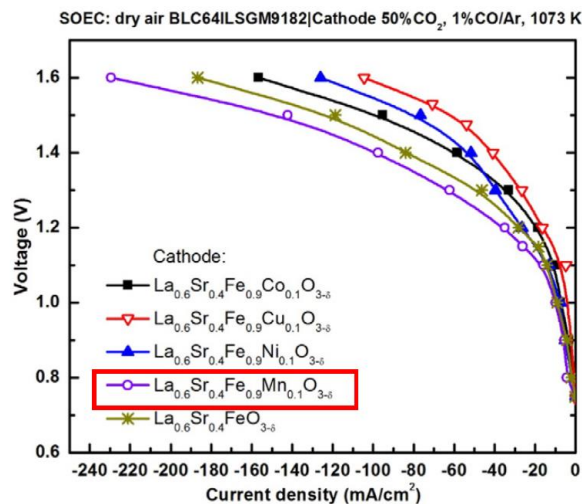
Figure 2-6. I-V curves for CO_2 electrolysis using the cells with $La_{0.6}Sr_{0.4}Fe_{0.8}M_{0.2}O_{3-\delta}$ (M=Co, Cu, Ni, and Mn) cathodes at 1073K [36].

It was reported that $LaSrFeO_{3-\delta}$ based materials have high performance (high current density at similar operating conditions) [113]. This is also the reason why this promising material was selected to be the research topic and used as a basic material to design new materials with improved performance.

Previous studies demonstrated that catalytically active transition metals (B-site of perovskite) can be released (exsolved) on the surface as metal particles following H_2 reduction [114-116]. Liu et al. [31] developed a novel cathode prepared by reducing the Sr and Ni co-doped $LaFeO_3$ perovskite oxide, i.e. $La_{0.6}Sr_{0.4}Fe_{0.8}Ni_{0.2}O_{3-\delta}$ (LSFN), in H_2 atmosphere at 1123 K. The Fe–Ni bimetallic alloy nanoparticles were successfully exsolved *in situ* and uniformly socketed on the oxygen deficient perovskite backbone. The cathode kinetics for CO_2 electrolysis was significantly improved with enhanced current density of $1.78 \ A \cdot cm^{-2}$ and a high Faradic Efficiency of 98.8% at 1.6 V and 1123 K. Similarly, Sun et al. [117] observed the formation of Ni nanoparticles on Ni-doped $(La_{0.7}Sr_{0.3})CrO_3$ perovskites when it was reduced at high temperatures.

In summary, B-site metal doping and exsolution method enhances the electronic conductivity of materials, increase the oxygen vacancy concentration at the reaction interface and facilitate the contact between CO_2 molecules and site-B transition metals, thus enhancing the electrocatalytic activity and improving CO_2 conversion efficiency [118-120].

2.3. Multiscale Modelling

Multiscale modelling aims to predict the behavior of the physical systems by connecting phenomena occurring at different length and time scales. Different modelling methods are currently

available to describe phenomena occurring at different scales [38-42, 121]. As shown in Figure 2-7, DFT and ab initio are commonly used to describe the electronic properties of materials and reaction kinetics [122]. Thermodynamic and transport properties can be depicted by Molecular Dynamics (MD) and Monte Carlo (MC) methods at the atomic scale [123, 124]. The former is often used to estimate time-dependent properties, e.g. thermal conductivity, viscosity and diffusivity coefficients. The latter is applied to estimate equilibrium properties, e.g. potential energy calculations, absorption studies or phase equilibria studies. Mesoscopic modelling methods, such as Kinetic MC methods, Brownian Dynamics are required to simulate the system at larger time and length scale [125-127]. When it comes to the macro-scale modelling, Finite Element Analysis methods are suitable [39, 128].

Multiscale modelling has been widely used to perform computer aided materials design. For example, a multiscale model of thin film formation by chemical vapor deposition was used to generate the training data for the artificial neural networks in the presence of uncertainty [129]. A hybrid first principles/artificial neural network based multiscale modelling approach was developed to simulate a thin film growth process [130]. The first principles based multiscale and multiphysiscs model can be used for systems engineering applied to Li-ion batteries [131]. Multilevel Monte Carlo sampling technique can be employed for uncertainty quantification in stochastic multiscale systems, e.g. catalytic flow reactor [132]. Multiscale systems engineering also has applications to chemical reaction process ranging from the atomistic to the macroscopic [133] and crystal shape/size control [134]. A multiscale framework for ab initio simulation of room temperature CO_2 reduction over an Ag(110) surface was presented to examine three alternative mechanisms [43]. Surface sites of Au-based catalysts in reducing CO_2 to CO at low temperature were simulated by multiscale models, guiding the design of high-performance electrocatalysts.[135]

First-principles multiscale modeling composed by DFT and mesoscopic kinetic Monte Carlo (kMC) was performed to simulate the complex reaction pathway of catalytic CO_2 hydrogenation to methanol, serving as a step towards the rational design of multifaceted copper catalysts.[136]

Despite the efforts mentioned above, an application of multiscale modelling methods to study CO_2 electrolysis in SOEC is not available. Therefore, it is highly desirable to develop a multiscale model that can simulate the properties of the electrochemical cell at different spatial scales. DFT based microkinetic modelling and DFT based multiphysics modelling are used in this thesis. This thesis aims at filling the gap in CO_2 electroreduction theoretical studies, specifically related to reaction mechanism, carbon formation, oxygen ion migration and doping effects. on both conventional Ni/SDC and perovskite $La(Sr)FeO_{3-\delta}$ surfaces. DFT, microkinetic modelling and finite element methods were adopted in this thesis to describe the system properties at the electronic, micro and macro level, respectively, e.g. elementary reaction mechanism, electronic properties of materials, rate controlling step, current density/gas species/adsorbate distributions, etc. These three methods are reviewed in the following discussion.
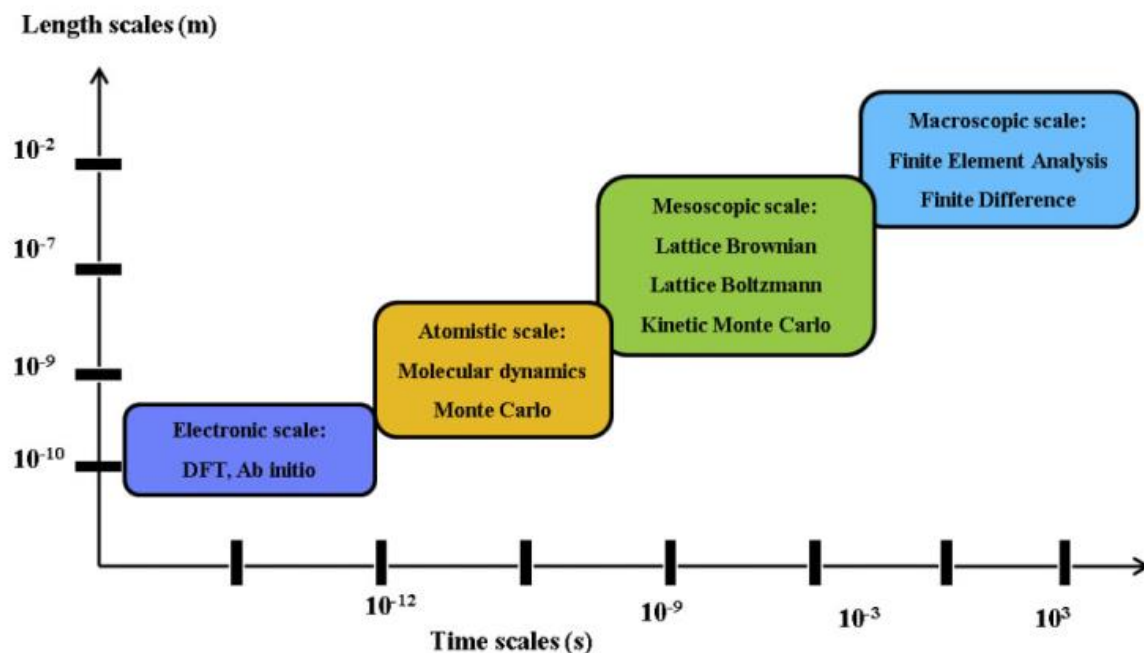
Figure 2-7. Schematic representation of the most representative modelling methods for multiscale modelling analysis [38].

2.3.1. Density Functional Theory (DFT) Studies in Solid Oxide Cells

Density Functional Theory (DFT) is one of the most popular and versatile methods available in condensed-matter physics, computational physics, and computational chemistry to search for a solution of the Schrödinger equation, the fundamental equation that describes the quantum behavior of atoms or molecules. Within this theory, the properties of a many-electrons system can be determined by using functionals, representing spatially dependent electron densities [137].

DFT is a powerful method to study CO_2 electrolysis that can provide key information that cannot be directly obtained from experiments. Theoretical works employing DFT have usually focused on the low temperature CO_2 reduction kinetic mechanism [9, 50, 51, 138-140]. The protonation of CO to CHO was found to be the rate-limiting step for CO_2 reduction to CH_4 on Cu (211) surface [141]. The binding free energy of CO is a descriptor for CO_2 reduction on copper and other transition-

metal surfaces [139, 141].

Multiple DFT simulation studies reported in the SOFC field focused on: 1) adsorption of atomic and molecular oxygen, methane and oxygen dissociation; 2) ionic conductivity (oxygen vacancy formation energy and migration) and 3) electronic conductivity (density of states (DOS)). DFT + U analysis disclosed a significantly different electronic structure and defect chemistry of $La_{0.5}Sr_{0.5}Co_{0.25}Fe_{0.75}O_{6-\delta}$ (LSCF) due to the addition of cobalt, when it was used as SOFC cathode material [142]. The role of electron-deficient substitution in promoting oxygen diffusion in $La_{1-x}Sr_xFeO_{3-\delta}$ (LSF) was also revealed by DFT simulations on oxygen vacancy formation and migration [143, 144]. $Sr_2Fe_{1.5}Mo_{0.5}O_{6-\delta}$ (SFM) perovskite was widely used as both cathode and anode materials of SOFC to investigate the oxygen ion and proton conductivity, e.g. oxygen vacancies formation energy with DOS analysis,[145] efficient proton transport with doping of K^+ [146] or oxide sublattice [147, 148], etc. The study of oxygen transport in $LaCoO_3$ as the SOFC cathode material base on DFT indicated that low spin Co^{3+} promotes higher oxygen vacancy concentrations than other spin states [149]. The modest amount of transferred electron charge follows vacancy formation in Ni/CeO_2 anode of SOFC, which can be explained based on DFT results and by the fact that the rather shallow vacancy-induced occupied band in ceria has a lower energy than the top of the Ni valence band [150]. As a follow-up study, the effect of Zirconia concentration was investigated, which showed that high ZrO_2 can increase oxygen vacancy formation energy and lower activity of the oxide surface with reduction of the oxygen spillover barrier [151]. DFT was also employed to study carbon removal from the $Ni/BaCe_{1-x}Y_xO_{3-\delta}$ anode TPB of SOFC by adsorbed water molecules [152]. The simulation results showed that oxidation of interfacial carbon was more favorable on $Ni/BaCe_{1-x}Y_xO_{3-\delta}$ anode as compared to Ni/YSZ, which occurred via a reaction with hydroxyls. Based on this, the authors of that study argued that

favorable carbon oxidation is governed by the ability of the oxide to adsorb and partially split water molecules [152]. DFT was employed to provide a comparison of the electronic properties of Ni/YSZ and Ni/CeO$_2$ interfaces and present an interpretation of their different chemical performances when used as anodes for SOFC [153]. DFT were also used to study the electric field effects on C-H bond cleavage in methane over Ni/YSZ surfaces, the results show that the presence of a low concentration of carbon species, or the addition of a positive electric field will improve the hydrocarbon activation process [154].

Perovskites are most widely used in the oxygen electrode of solid oxide cells to act as catalysts for oxygen reduction reaction (SOFC) and oxygen evolution reaction (anode of SOEC). Most of the DFT studies described above for the perovskites acting as SOFC oxygen electrodes can also be applied to SOEC to explain some properties of perovskites, such as the adsorption energy of oxygen, ionic conductivity and oxygen exchange rate. Only a handful of DFT studies have been reported for SOEC. Nikolla et. al [155] studied H$_2$O dissociation in SOEC on Ni and Ni-based alloy electrocatalysts and found a volcano-type relationship between the calculated electrochemical rates and the binding energies of O by DFT. Ni/Fe alloy was found to show the highest rate of H$_2$O dissociation. Che et. al [156] investigated the field effects on hydrogen oxidation and water decomposition over the TPB region of the Ni/YSZ electrode and found that positive electric field can decrease the water decomposition rate. DFT was also used to interpret experimental work of CO$_2$ adsorption on (La,Sr)TiO$_3$ cathode surface. [157] and on La$_{0.4}$Sr$_{0.6}$Co$_{0.2}$Fe$_{0.7}$Mo$_{0.1}$O$_{3-\delta}$ [158]. However, no DFT works on CO$_2$ adsorption, reduction energy barrier, oxygen vacancy effect on Ni/SDC and La$_{0.6}$Sr$_{0.4}$FeO$_{3-\delta}$ based materials in SOEC have been reported.

Figure 2-8 shows the general scheme of DFT analysis, where surface models are required to be established first according to the material properties reported in the literature. Structural

optimization is then considered to identify the ground states (most stable configurations) of the system. Next, adsorbate molecules are placed at different sites of the surface to perform structural optimization and be able to determine the most stable adsorption sites.
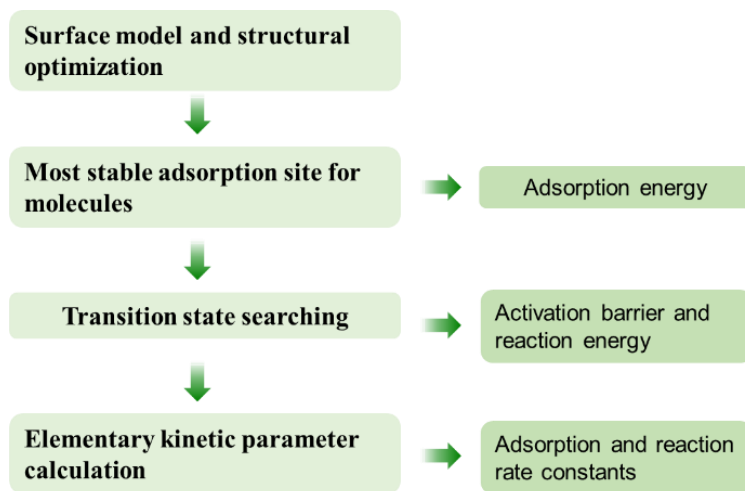
Figure 2-8. Scheme of the DFT analysis

The adsorption energy can be calculated according to these energetic results and used to establish reaction paths. These paths are found through transition state (TS) search using the climbing image nudge-elastic band (CI-NEB) method [159]. The fundamental idea in Nudged Elastic Band method is to perform an optimization over a number of intermediate images that maintain equal spacing to their neighboring images along the reaction path. Saddle points (the image with the highest energy) are identified among these optimized structures between known products and reactants to establish the reaction scheme with the minimum energy barrier. DFT can also be used to calculate the electronic structure, i.e. density of states [160].

2.3.2. Microkinetic Modelling

Microkinetic modeling is a powerful tool in computational catalysis field, consisting in the construction of explicit kinetic reaction networks merging kinetic data provided by DFT calculation

or obtained experimentally [161-163]. Microkinetic models can be used to predict the rate limiting step, dominant reaction pathway, dominant adsorbate intermediates and estimate the dependence of the rate-determining step on operating conditions [162]. They are simple to apply, demand little computational effort and constitute an excellent complement to the free energy profiles which are routinely computed with DFT methods [162]. A common assumption in microkinetic modelling is the so-called mean-field approximation. In mean-field model, all the surface species and active sites are assumed to be uniformly distributed at the nanometer scale [163].

In microkinetic modelling, the forward and reverse rate constants for all elementary steps are implemented into a set of rate equations to obtain the "surface coverages" of all adsorbed species and empty sites at specific reaction conditions. The coverages are further used to calculate the rates of all the elementary steps. For example, if θ_A and θ_v denote the surface coverages of the adsorbed species and the vacant sites in first-order reaction, respectively, then the adsorption rate of the above elementary reactions can be expressed as follows,

$$r = k_{\text{for}}\, \theta_v P_A - k_{\text{rev}}\, \theta_A. \qquad (2\text{-}4)$$

where P_A is the partial pressure of the gas phase species A. k_{for} and k_{rev} represent the rate constants of the forward and reverse reactions respectively, which can be determined by DFT calculations or experiments.

Then, a set of ordinary differential equations (ODEs) can be built to describe the time-dependent or steady-state concentration of each species in the reaction mechanism, i.e.

$$\frac{dC_i}{dt} = \sum_m (r_{prod,m} - r_{cons,m}) \qquad (2\text{-}5)$$

where C_i is the concentration of species i; $r_{prod,m}$ is the producing rate of species i in reaction m; $r_{cons,m}$ is the consuming rate of species i in reaction m. Solving the ODEs provides the time

evolution of the surface coverage of species and reaction rates. A general approach of DFT based microkinetic modelling is shown in Figure 2-9. As shown in this figure, the energetic results obtained from DFT calculations (activation barrier, adsorption energy, vibrational frequencies, etc.) can be incorporated into the microkinetic models as inputs. A microkinetic model for heterogeneous catalysis involves both gas and surface species. The rate constants of surface reactions and non-activated surface adsorption/desorption are calculated by the transition state theory and collision theory [163], respectively. Microkinetic modeling allows to bridge reaction kinetics to concentration gradients.

Developing a microkinetic model based on kinetic data obtained from DFT calculations is also critical to predict rates of elementary steps under realistic temperatures and pressures, and surface coverages influenced by temperature and voltage [53, 164, 165]. This enables the coupling of reaction kinetic data and electrochemical measurements [166], e.g. polarization curves[52].
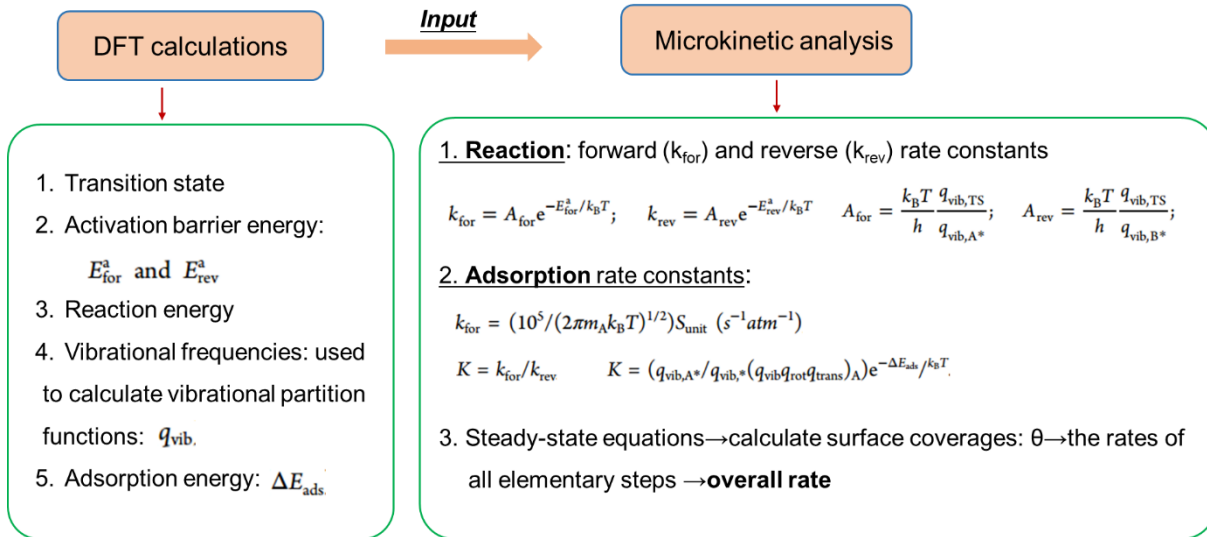
Figure 2-9. Scheme of the DFT based microkinetic modelling

Nørskov et al. [51] reported a DFT combined microkinetic model to study low temperature CO_2 electroreduction to CO pathway on Ag(111) surface and indicated that the electric field aims to

stabilize key intermediates *CO$_2$ and *COOH. Heyden et al. [164] conducted DFT calculations combined with microkinetic modeling considering the effects of anode bias potential which were used to investigate the electrochemical oxidation of H$_2$ fuel on the (001) surface of Sr$_2$Fe$_{1.5}$Mo$_{0.5}$O$_6$ (SFMO) perovskite. The model predicts that water desorption is rate-controlling and that stabilizing the oxygen vacancy structure increases the overall rate for H$_2$ oxidation. The same group also performed a combined DFT and microkinetic modeling study of hydrogen oxidation at the Ni/YSZ anode of solid oxide fuel cells [166]. The results show that bulk oxygen diffusion in YSZ is rate-limiting at low temperatures, and H transfer from Ni to YSZ to form water becomes rate-limiting at high temperatures. Zhu et al. [54] built a DFT based microkinetic model to explore the reaction mechanism for dry methane reforming on Ni catalyst. This study identified the dominant reaction pathway and examined the dependence of the rate-determining step on operating conditions. Despite these efforts, there is no reported DFT based microkinetic modelling work for high temperature CO$_2$ electrolysis in SOEC. In order to improve the performance of SOEC, it is crucial to gain theoretical insights of CO$_2$ reduction reaction mechanism, especially through microkinetic modelling by considering the effects of high temperature and electrode overpotentials.

2.3.3. Multiphysics Finite Element Method Simulations

Searching for optimal conditions for electrochemical cell operation requires knowledge of the CO$_2$ reduction mechanism and the influence of all factors controlling cell performance. Measuring the conditions inside SOEC is quite challenging and very expensive to perform regularly due to high operating temperature (700-800°C). Modeling can be a comprehensive cost-effective tool to analyze the performance of such devices. In addition, compared with experimental analysis, computational modelling and simulation are more effective tools to investigate the underlying mechanisms of these complex processes; in particular to study the surface adsorbate distributions,

31

e.g. when their coverages are too low to be detected using experimental tests.

The finite element method (FEM) is a numerical discretization method for solving partial differential equations (PDEs) by subdividing a large system into smaller parts, which are called finite elements [167]. Multiphysics means the coexistence of multiple physical fields in a process or a system, which has become a research frontier in academic communities and industrial practice due to confrontation with problems of the disciplinary boundaries between physics, chemistry, material science and biology [168]. COMSOL Multiphysics is a cross-platform finite element based simulation software, which gives conventional physics-based interfaces and coupled systems of PDEs to address a wide range of physical phenomena [169-171].

Regulations of chemical and electrochemical reactions act a critical role in chemical engineering and are typical multiphysics problems, not only depend on catalysts and local environments over them (e.g. concentration of reactants and products, temperature, etc.), but also depend on the coupled mass, charge, and heat transport [172]. Variations in local environments are crucial in heterogeneous reactions and have significant effects on performance, selectivity, and degradation, and make the assessment of kinetics difficult [173].

COMSOL multiphysics finite element numerical modeling has gained popularity in research as it can provide design and operating criteria for regulations of chemical and electrochemical reactions by accounting for the critical physical phenomena, including electrochemistry, reaction kinetics, multiphase flow, and heat transfer [43, 174-176]. Multiphysics simulation in electrochemistry is based on Faraday's law, Ohm's law, Butler-Volmer equation, and gas transport equations [177]. Faraday's law relates the applied current to the flow of oxygen ions [177]. Ohm's law corresponds to the losses associated with the resistance to the flow of both ions and electrons. Butler–Volmer equation can be used to calculate the current density [59, 178-182] for the models without

considering the elementary reactions.

Multiphysics modelling can be used to predict the properties of a SOEC system, such as polarization curves, gas species distributions, adsorbate species distributions, current density distributions or the effects of various operation conditions and geometric parameters.

Butler–Volmer equation has been used in the modelling of CO_2 reduction in SOEC to calculate the current density [59, 178-182] without considering the elementary reactions. For the reported studies with detailed elementary reactions, the current density is related to the charge transfer steps.

There is still a gap in the literature regarding the most likely reaction mechanism of charge transfer step. A previous study with elementary heterogeneous reactions assumed $CO_2(Ni) + (YSZ) + 2e^-$ $\leftrightarrow CO(Ni) + O^{2-}(YSZ)$ as the charge transfer step [58]; however, that study did not consider the oxygen ion spillover step. For CO_2 electrolysis in SOEC, the oxygen ion produced by CO_2 reduction could also be on Ni, i.e. $O^{2-}(Ni)$ instead of $O^{2-}(YSZ)$ [52, 183, 184]. One-step oxygen ion spillover from Ni surface to YSZ surface, i.e. $O^{2-}(Ni) + (YSZ) \leftrightarrow O^{2-}(YSZ) + Ni(s)$, is used to describe the charge transfer step [183-185]. Two-step charge-transfer mechanism was also used to describe the reaction and transfer processes of CO-CO_2 electrochemical conversion. For example, Yurkiv et al. [186] investigated three different spillover mechanisms for electrochemical CO oxidation at Ni/YSZ anodes. That study reported that the best agreement with the experimental data was obtained when two consecutive single-electron charge-transfer steps from $O^{2-}(YSZ)$ via $O^-(YSZ)$ to $O(Ni)$ were considered. Shi et al. [187] developed an elementary reaction model for reversible CO-CO_2 electrochemical conversion to couple two charge-transfer reactions, i.e. $C(Ni)+O^{2-}(YSZ)\leftrightarrow CO(Ni)+(YSZ)+2e^-$ and $CO(Ni)+O^{2-}(YSZ)\leftrightarrow CO_2(Ni)+(YSZ)+2e^-$.

Detailed elementary reaction kinetics should be incorporated in the computational models to

provide insights in revealing the reaction mechanisms. Many mathematical models have been developed with detailed heterogeneous chemistry, coupled with ionic/electronic conduction and gas-phase transport for CO_2 electrolysis in SOEC. Table 2-2 presents a summary of recent simulation works using FEM in solid oxide cells. From this table, one can observe that most of the current models in SOEC are one-dimensional (1D) models [56, 179, 184, 188]. However, models involving higher spatial dimensions can provide more information of the performance of the cell than 1D models, e.g. spatial distributions of current density, reaction intermediates and gas species. For the two-dimensional (2D) modelling work, almost all the works have used a global reaction mechanism [59, 182, 189-191]. Global reaction models cannot provide detailed information, such as reaction intermediates, charge transfer step and rate controlling step. Until now, there is only one 2D SOEC model with detailed heterogeneous catalysis and electrochemical reactions reported in the open literature [183]. However, many reaction kinetic data used in this paper are fitted to experimental data and there is no discussion about possible charge transfer steps. Therefore, to fill this gap, the objective of this thesis is to analyze the most possible charge transfer and provide new insights by using as few fitted data as possible. i.e. by adopting all the pre-exponential factors and activation barriers of every elementary step from DFT.

Table 2-2 Summary of recent multiphysics work in solid oxide cells.

	Kinetic/geometry	Research contributions	Ref.
Reversible CO/CO_2 electrochemical conversion on patterned nickel electrodes	1D, Electrolyte supported button cell (elementary reaction-based)	studied two-charge-transfer-step mechanism and validated in both SOEC and SOFC; elucidated the role of surface diffusion of CO and CO_2.	[188]

Electrochemical reduction of CO_2	1D, Cathode supported button cell (elementary reaction-based)	validated with own experimental data; found that the carbon deposition phenomenon at the cathode/electrolyte interface is more serious.	[58]
Syngas production by H_2O/CO_2 co-electrolysis	1D, Cathode supported planar SOEC (elementary reaction-based)	considered 42-step elementary heterogeneous reaction mechanism; two sets of experimental data are reproduced by the simulations.	[56]
Ni/YSZ Electrodes in CO_2 and Co-electrolysis	1D and 2D, Cathode supported planar SOEC (global reaction-based)	considered the effect of the rib from the interconnect.	[181]
CO_2/H_2O co-electrolysis cell	1D, Cathode supported button cell (elementary reaction-based)	considered the effects of cathode thickness; found that the main zone of electrochemical reactions is far enough from the main zone of heterogeneous reactions when the cathode is thick enough (e.g. 700 μm).	[184]
Modeling of CH_4-assisted SOEC for H_2O/CO_2 co-electrolysis	2D, Tubular, cathode support (global reaction-based)	found that CH_4 assisting is effective in lowering the equilibrium potential of SOEC thus greatly reduces the electrical power consumption for H_2O/CO_2 co-electrolysis.	[59]
Co-electrolysis of steam and carbon dioxide	2D, Cathode supported tubular SOEC (global reaction-based)	considered the fluid flow, heat/mass transfer and electrochemical/chemical reactions in the SOEC; found that reversed water-gas shift reaction significantly promotes CO_2 conversion ratio.	[189]
Methane production by H_2O/CO_2 Co-electrolysis	2D, Cathode supported tubular SOEC (global reaction-based)	found that addition of H2 and the increase of electrolysis current could promote CH4 production rate.	[190]

Electrochemical Reduction of CO_2 to CO	2D, Cathode supported planar SOEC microfluidic flow cell (global reaction-based)	analyzed the effects of applied cell potential, CO_2 concentration of the feed and feed flow rates, channel length and porosity of the gas diffusion electrodes.	[182]
Modeling for syngas generation	2D, Cathode supported button cell SOEC(elementary reaction-based)	considered detailed surface chemistry and the effects of applied voltage and temperature on carbon deposition.	[183]
Thermal modeling for syngas production by H_2O/CO_2 co-electrolysis	2D, Cathode supported planar SOEC(global reaction-based)	studied the heat/mass transfer and considered the effects of methanation and internal reforming on the co-electrolysis process.	[191]
Understanding degradation mechanism	3D, Cathode supported planar SOEC (Both fuel cell and electrolysis mode, global reaction-based)	considered the electrode thickness and more geometric parameters	[192]
Localized carbon deposition study	3D, Cathode supported planar SOEC (global reaction-based)	found that gas diffusion and temperature are important driving forces for C deposition; C deposition can be avoided by thinner and more porous electrodes.	[193]

2.4. Summary

Based on the literature review presented in this Chapter, conventional cathodes in SOEC are metal–ceramics (cermet) such as Ni/YSZ and Ni/SDC, in which Ni demonstrates high catalytic activity and provides the electronic transport path, whereas YSZ (electrolyte material) provides the ionic diffusion path. Compared to YSZ, SDC exhibits higher ionic conductivity at intermediate temperatures (600-750℃). Thus, Ni/SDC was selected in this thesis. However, surface oxidation

and coke deposition on Ni particles leads to loss of electronic conductivity and cell degradation during high temperature CO_2 electrolysis. CO_2 electroreduction mechanisms are still not clear which plays an significant role in improving the performance of SOEC. (e.g. rate controlling step, oxygen ion conduction, the effects of oxygen vacancy location, charge transfer step and carbon deposition distribution). Therefore, additional research on conventional metal–ceramic cathode are needed to address these problems. As described previously, there are alternative SOEC materials that address coking issues, essentially perovskites. Perovskite-type oxides have been proven to be the most promising replacement of the conventional Ni/SDC in SOEC. $La_{0.6}Sr_{0.4}FeO_{3-\delta}$ based perovskite oxides were selected as the main research topic in the present work because they have shown enhanced coking resistance and good compatibility with electrolyte materials (YSZ or SDC), although accompanied by insufficient catalytic activity and surface Sr segregation problems which causes cell degradation. The catalytic activity is still low because there are not enough theoretical insights for the design of this materials. Specifically, the functional mechanisms of B-site doping elements (e.g. Ni or Mn) in improving the catalytic activity are not clear.

Multiscale modelling is a powerful tool to provide the theretical insights of the phenomena occurring at different scales; in particular, DFT for electronic scale, micro-kinetic modelling for micro-scale and multiphysics FEM for macro-scale. Therefore, developing a multiscale modelling approach combining different modelling methods is very important for the development of CO_2 electrolysis in SOEC, which has not been reported in the literature. In order to fill the gaps in the literature mentioned above, a DFT based microkinetic modelling study for Ni/SDC is presented in Chapter 3. As a follow up study, a DFT based multiphysics model for Ni/SDC is presented in Chapter 4. For another research topic, i.e. $La(Sr)FeO_{3-\delta}$ based materials, a DFT based microkinetic modelling study is presented in Chapter 5.

Chapter 3. CO$_2$ Electrolysis at Ni/SDC Cathode by Combined DFT and Microkinetic Modelling

Better understanding of CO$_2$ electroreduction mechanism at the TPB is of great importance for the development of SOEC. In this chapter, CO$_2$ electroreduction mechanism on Ni/SDC surface is studied by combined DFT and micro-kinetic analysis. The rate controlling step is determined on the surface models with different oxygen vacancy locations. The effect of voltage is considered.

3.1. Introduction

It has been reported that oxygen vacancy sites can act as host for CO$_2$ chemical adsorption at high temperatures [94]. Also, the chemically adsorbed CO$_2$ can also be activated on oxygen vacancy sites, which is favorable for the electrochemical reduction [94, 194-196]. However, the effect of oxygen vacancies and detailed interface oxygen migration mechanism for CO$_2$ electroreduction on Ni/SDC in SOEC are still unclear. In addition, the rate controlling step of high temperature CO$_2$ electroreduction in SOEC considering the effect of electrode overpotentials has not been studied yet.

In order to improve the performance of SOEC, it is necessary to explore the reaction mechanism of CO$_2$ electrochemical reduction including oxygen migration. In this study, catalytic reaction mechanisms of CO$_2$ electrolysis at the Ni/SDC TPB were investigated using a combination of DFT+U calculation and mean-field microkinetic modeling method [164, 166]. Specifically, the energetics of elementary reactions in CO$_2$ reduction including oxygen ion migration on Ni(111)/SDC surface were first studied using DFT+U calculations. Then, the energetic results were incorporated into a microkinetic modeling. All possible charge transfer steps, including one- or

two-electron charge transfer, are considered and discussed.

3.2. Models and Methods

3.2.1. Surface Models

The Ni (111)/ceria model proposed by Ziegler's group [153] was adopted in the present study. This is a representative model for the interface of Ni cluster and ceria surface. Hermansson et al.[197] suggested that a nine-layer surface model would be sufficient for the CeO_2(111) surface calculations. For the surface model, it was reported that CeO_2(111) is energetically the most stable [197, 198] among the low-index CeO_2(111), (110), and (100) surfaces. Therefore, low energy ceria (111) surface was modeled using a (2×2) supercell slab with 9 atomic layers thick (24 CeO_2 formula units with 72 atoms). The Ni cluster includes three layers of Ni atoms with nine, six, and three Ni atoms on the bottom, medium, and top layers, respectively. The Ni cluster is periodic in one direction (Figure 3-1) and exhibits a (111) surface towards the gas phase (Figure 3-1b). A theoretical lattice constant of ceria (5.49 Å) has been used in the present study [199]. The vacuum gap is set to be 15 Å. $Ce_{1-x}Sm_xO_{2-x}$(x=0.1~0.2) is the optimum ratio due to its highest ionic conductivity [200, 201]. Herein, we replaced four Ce atoms with Sm atoms ($Ce_{20}Sm_4O_{46}$) to build a slab model consisting of 17 mol % Sm in SDC which is within the optimum ratio of Sm substitution reported above. Substituting every two Ce atoms with Sm will produce one oxygen vacancy. Accordingly, two oxygen vacancies were created to meet the stoichiometry requirement. By performing calculations with different locations of two Sm atoms, as shown in Table S3-1 in Supporting Information, the most stable SDC slab model was identified, in which one substituting Sm atoms should be located in the outermost surface and another one in the sub-surface layer.

To study the effects of interface oxygen vacancy on CO_2 electrolysis on Ni/SDC, two surface

39

models of Ni/SDC (with different oxygen vacancies locations) were built. Model 1 is Ni-SDC with non-interface surface oxygen vacancies of SDC created by removing the oxygen atoms O1 and O3 in Figure 1a. Model 2 is Ni-SDC with interface oxygen vacancy modelled by removing O2 which is bound with Ni and Ce at the interface and O3 (Figure 3-1a).

(a)   (b)
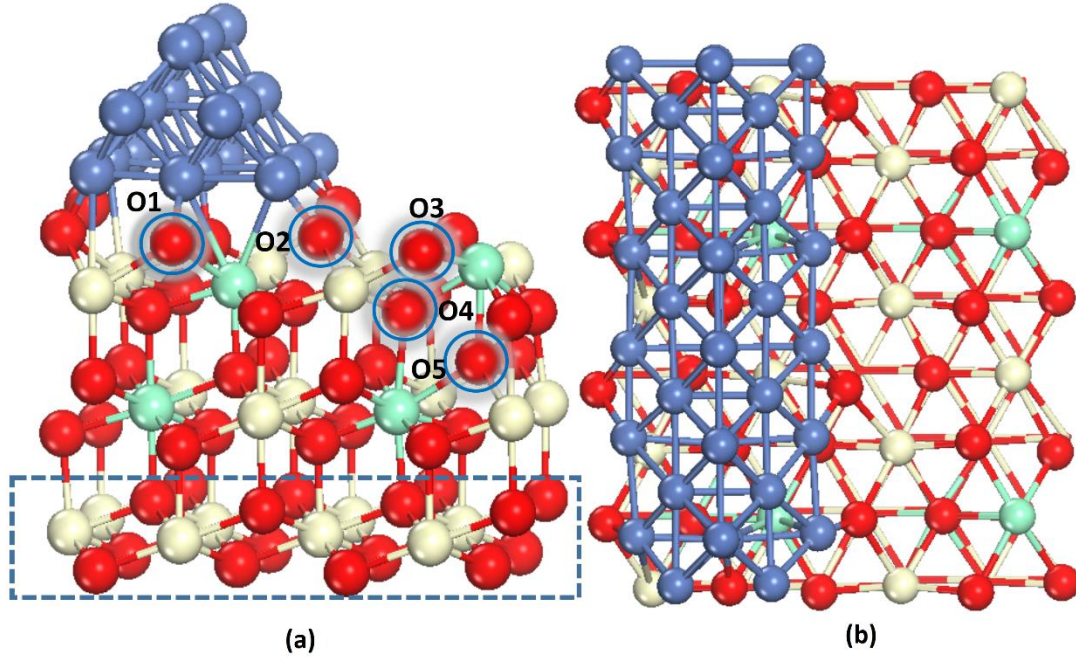
Figure 3-1. (a) Side view and (b) periodic top view of optimized structure of Ni(111) /SDC model. Atoms with the dark-blue, white, cyan and red colors represent the Ni, Ce, Sm, and O atoms, respectively. **O1** and **O3** are surface oxygen atoms of SDC. **O2** represents the Ni/SDC interface oxygen. **O4** is subsurface oxygen, while **O5** represents bulk oxygen of SDC. The bottom three atomic layers, represented by the blue dotted box, are fixed during the calculations.

3.2.2. Computational Details

All calculations were carried out using DFT+U framework with periodic boundary conditions using Vienna Ab initio Simulation Package (VASP 5.4.4) [202, 203]. To solve the ion-electron interactions in a periodic system, the projector-augmented wave (PAW) method was applied [204]. The generalized gradient approximation (GGA) [205] with Perdew−Burke−Ernzerhof (PBE) [206] functionals was used to take into consideration the exchange-correlation interactions in the

Kohn−Sham equations [202]. Spin-polarized calculations have been carried out at the Γ-point using the Gaussian smearing method (σ=0.1 eV) with an energy cut off for the plane waves of 400 eV. Based on a slab with horizontal dimensions of 13.25×7.65 Å, the Monkforst-Pack k-point mesh of $2 \times 2 \times 1$ k-points was employed [207-209]. By increasing the cut off energy to 450 eV and the number of k-points to $4 \times 4 \times 1$, we observed a negligibly small change in adsorption energies (<0.01 eV), which indicates that adsorption energy values are well converged with respect to these parameters. A Hellmann-Feynman [210] force of 0.01 eV/Å was chosen as the convergence criterion for optimization of the atomic structure.

The Hubbard parameter, U=5 eV, was adopted in this work. This U value yields a qualitatively correct distribution of f-electrons, localized on the Ce atoms. For U = 5 eV, the 4f electrons are reported to be completely localized on two Ce ions near the oxygen vacancy [211]. The 4f electrons of Sm were treated as part of the core (core state model); therefore, the empirical U parameter for the 4f electrons of Sm was not required [68]. All atoms in the slab and the cluster were relaxed except the bottom 3 atomic layers of the SDC slab. The structures of transition state (TS) of elementary steps were obtained using the climbing image nudge-elastic band (CI-NEB) method [159].

The adsorption energy E_{ads} of surface species is defined as follows:

$$E_{ads} = E_{absorbates/slab} - E_{slab} - E_{adsorbates} \qquad (3\text{-}1)$$

where $E_{absorbates/slab}$, $E_{adsorbates}$ and E_{slab} represent the total energy of surface slabs with adsorbates, the energy of free adsorbates and the energy of bare surface slabs of Ni/SDC, respectively. The activation barrier E_a and reaction energy ΔE are defined as follows [208]:

$$E_a = E(TS) - E(IS) \qquad (3\text{-}2)$$

$$\Delta E = E(FS) - E(IS) \qquad (3\text{-}3)$$

where $E(IS)$, $E(TS)$, and $E(FS)$ represent the total energies of the initial state (IS), transition state (TS) and final states (FS), respectively. Negative values of ΔE represent exothermic reactions.

3.2.3. Microkinetic Model

Transition state theory was used to calculate the forward and backward rate constants (unit: s^{-1}) for a surface reaction $A^* \rightarrow B^*$,

$$k_{for} = A_{for}e^{-E_{for}^a/RT} \qquad (3\text{-}4)$$

$$k_{rev} = A_{rev}e^{-E_{rev}^a/RT} \qquad (3\text{-}5)$$

where * indicates an active surface site, E_{for}^a and E_{rev}^a denote the zero-point energy (ZPE)-corrected forward and reverse activation barriers, respectively [164]. The ZPE was obtained as $\sum_i (1/2)h\nu_i$ from calculated vibrational frequencies, ν_i. h is the Planck constant. R is the gas constant and T is the temperature in Kelvin. The frequencies of all involved species were calculated and are presented in Table S3-2 in the Supporting Information.

All the transition states were confirmed with one imaginary frequency. The frequency factors (A) were calculated from the vibrational partition functions $q_{vib,TS}$, q_{vib,A^*}, q_{vib,B^*} for the transition state (TS), A* and B*, respectively, using the following expressions [164] :

$$A_{for} = \frac{k_B T}{h} \frac{q_{vib,TS}}{q_{vib,A^*}} \qquad (3\text{-}6)$$

$$A_{rev} = \frac{k_B T}{h} \frac{q_{vib,TS}}{q_{vib,B^*}} \qquad (3\text{-}7)$$

$$q_{vib} = \prod_i \frac{1}{1-e^{-h\nu_i/k_B T}} \qquad (3\text{-}8)$$

where k_B is the Boltzmann's constant.

For surface adsorption process, A + * → A*, the forward k_{for} and reverse k_{rev} rate constants, and the equilibrium constant K are correlated through $K = k_{for}/k_{rev}$. The equilibrium constant was calculated using the following expression [166],

$$K = \frac{q_{vib,A^*}}{q_{vib,A^*}q_{rot,A^*}q_{trans,A^*}} e^{\frac{-\Delta E_{ads}}{RT}} \qquad (3\text{-}9)$$

where ΔE_{ads} is the zero-point energy corrected adsorption energy. q_{rot,A^*} and q_{trans,A^*} are the rotational and translational partition functions respectively. The present model assumes that all the CO_2 molecules are absorbed into the surface; thus the sticking coefficient was set to the unity. Note that this assumption has also been considered in previous models[32]. Based on the above, the forward adsorption rate constant of an adsorption reaction was calculated as follows ((unit: $s^{-1}bar^{-1}$)),

$$k_{for} = \frac{10^5}{\sqrt{2\pi m_A k_B T}} S_{unit} \qquad (3\text{-}10)$$

where m_A is the molecular weight of species A. S_{unit} is the surface area per site, which is 3.13×10^{-19} m^2 for the Ni cluster in our model.

The forward and reverse rate constants for all elementary steps were implemented into a set of steady-state rate equations to obtain the "surface coverages" of all adsorbed species and empty sites at specific reaction conditions. The coverages are further used to calculate the rates of all the elementary steps. For example, if θ_A and θ_v denote the surface coverages of the adsorbed species and the vacant sites, respectively, then the adsorption rate of the above elementary reactions can be expressed as follows,

$$r = k_{for}\, \theta_v P_A - k_{rev}\, \theta_A. \qquad (3\text{-}11)$$

where P_A is the partial pressure of the gas phase species A.

Once the forward and backward rate constants of each elementary steps are identified, the rate controlling step in CO_2 reduction under different SOEC operating cathode over-potentials can be determined. Campbell's theory [212] was used in this work to determine the rate controlling steps [164, 166]. In Campbell's theory, the "degree of rate control" for step i, $X_{RC,i}$ is calculated as follows:

$$X_{RC,i} = \frac{k_i}{r} \left(\frac{\delta r}{\delta k_i}\right)_{K_i, k_{j \neq i}} \tag{3-12}$$

where the equilibrium constant for step i (K_i) and all other rate constants ($k_{j \neq i}$) are held constant. The larger the numerical value of $X_{RC,i}$, the larger the influence of its rate constant on the overall reaction rate r.

For an elementary step involving a charge transfer process, the forward and backward charge transfer reaction rates are formulated as follows:

$$k_{for} = k_f^0 \exp\left(\frac{\beta n_i e \eta}{RT}\right) = A_{for} \exp\left(\frac{-(E_{for}^a - \beta n_i e \eta)}{RT}\right) \tag{3-13}$$

$$k_{rev} = k_r^0 \exp\left(\frac{-(1-\beta) n_i e \eta}{RT}\right) = A_{rev} \exp\left(\frac{-(E_{rev}^a + (1-\beta) n_i e \eta)}{RT}\right) \tag{3-14}$$

where n_i represents the number of transferred electrons in the charge transfer step, e is the charge of an electron (equivalent to 1.6×10^{-19} C), β is the symmetry factor ($\beta = 0.5$) and η is the cathode overpotential [58].

3.3. DFT Results Analysis

In this section, oxygen vacancy formation, energetics of CO_2 and CO decomposition, CO_2 reduction mechanism are presented in detail.

3.3.1. Oxygen Vacancy Formation

Previous DFT studies have shown that the nearest neighbor (1NN) position of dopant is the most

energetically favorable site for oxygen vacancy formation [70, 213, 214]. The nearest neighbor (1NN) position of dopant Sm in the models considered in this work includes surface, subsurface and bulk oxygen. The formation of these types of vacancies were studied on ceria surface. The vacancy formation energy has been evaluated as follows [153, 215]:

$$E(vac.) = E(Ni/SDC + vac.) + E(O) - E(Ni/SDC) \qquad (3\text{-}15)$$

where E(Ni/SDC) and E(Ni/SDC + vac.) are the total energies of the cells before and after the vacancy formation, respectively; E(O) is the half energy of an oxygen molecule in the triplet state.

DFT calculations revealed that, in the absence of a Ni cluster, the formation of subsurface oxygen vacancies is most energetically favored with an E(vac) of -1.12 eV (exothermic) in SDC surface model. This indicates that, with Sm doping, oxygen vacancy formation on CeO_2 (111) surface is spontaneous. The corresponding model and the oxygen vacancy formation energy are presented in Figure S3-1 in the Supporting Information (SI). In the presence of Ni cluster, surface oxygen vacancies are prone to form with a formation energy of 2.27 eV, which is lower than that of other oxygen vacancies configurations (Figure S3-2 in the SI). Thus, Ni/SDC with two surface vacancies (i.e. removing **O1** and **O3** as shown in Figure 3-1) has been built for Model 1, i.e. Ni(111)/SDC with two surface oxygen vacancies. Model 2 can be considered as a special case of Model 1, when one of the surface oxygen vacancy is located at the interface of Ni and SDC. Note that the formation of a non-interface surface oxygen vacancy is more favorable than the formation of an interface oxygen vacancy (formation energies are 2.28 and 3.67 eV, respectively) in the presence of Ni. This is consistent with that reported for Ni/CeO_2 in a previous study [150]. In summary, surface oxygen vacancy is most energetically favored, which is also the reason why only surface vacancies were considered in both models.

3.3.2. $CO_2 \rightarrow CO + O$

CO_2 adsorption and reduction were studied on Ni-SDC with non-interface oxygen vacancies (Model 1) and with interface oxygen vacancy (Model 2). All configurations for the CO_2 reduction reaction are presented in Figure 3-2 and the energetics of the elementary steps are listed in Table 3-1. The adsorption energies are shown in Table S3-3 in SI. In Model 1, CO_2 can be physically adsorbed (-0.33 eV) at the surface of SDC. For CO_2 adsorbed on top of the Ni cluster, the corresponding CO_2 chemical adsorption energy is -0.52 eV, which is close to that reported for Ni (211) surface in the literature [216-218]. This value is reasonable because even though Ni (111) surface is exposed to a gas phase, the top site of the pyramid Ni cluster can be considered as a step surface. CO_2 reduction reaction on top of the Ni cluster of Model 1 has a forward and backward activation energy barrier of 0.91 eV and 1.51 eV, respectively (Table 3-1). The adsorption energy of CO_2 at the interface of Ni/SDC (Model 1) is -0.15 eV. The corresponding forward and backward activation energy for this reaction were found to be 0.63 eV and 1.02 eV, respectively. The low CO_2 reduction energy barrier at the Ni/SDC interface site suggests that the interface site in Model 1 is more favorable for CO_2 reduction than Ni cluster top site.

As shown in Table S3-3, the adsorption energy for Model 2 indicates that CO_2 can be strongly bonded with the interface oxygen vacancy of Ni and SDC. The corresponding adsorption energy is -1.01 eV, indicating that CO_2 molecules may be easily incorporated into interface oxygen vacancy sites. Such vacancy sites act as host sites to accommodate the nonpolar CO_2. The energy barriers of the CO_2 reduction step on the Ni/SDC interface (0.21 eV) and on the Ni cluster top (0.39 eV) are much lower than that of Model 1 (Table 3-1). This implies that CO_2 reduction is notably promoted by the interface oxygen vacancy at the Ni/SDC.
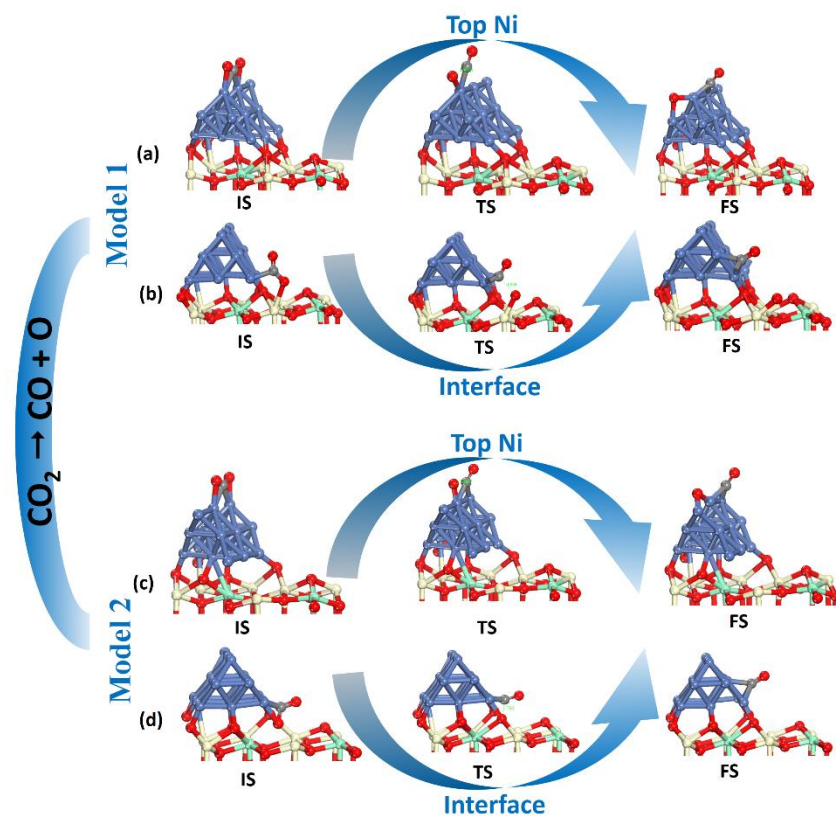
Figure 3-2. Configurations of the initial states (IS), the transition states (TS) and the final states (FS) for the CO_2 reduction reaction on Ni-SDC with non-interface oxygen vacancy (Model 1) and with interface oxygen vacancy (Model 2). CO_2 reduction (a) on top of Ni cluster for Model 1; (b) at the interface of Ni cluster and SDC for Model 1; c) on top of Ni cluster for Model 2; d) at the interface of Ni cluster and SDC for Model 2.

Table 3-1. Activation energy (E_a /eV, the first value is for the forward reaction and the second for the backward reaction) and bonding distance (d/Å) (distance between atoms involved in the broken or new formation bonds in the transition states).

Reactions	Model 1		Model 2	
	E_a /eV	d /Å	E_a /eV	d /Å
$CO_2 \rightleftharpoons CO + O$ (interface)	0.63 / 1.02	1.98 (C-O)	0.21 / 1.17	1.77(C-O)
$CO_2 \rightleftharpoons CO + O$ (top Ni)	0.91 / 1.51	1.82(C-O)	0.39 / 1.19	1.81(C-O)
$CO \rightleftharpoons C + O$ (interface Ni)	3.08 / 1.42	2.00(C-O)	2.67 / 0.72	1.80(C-O)

CO $\rightleftharpoons$ C+O (top Ni)	3.84 / 2.87	2.05(C-O)	2.91 / 1.78	2.01(C-O)
O migration on Ni cluster	0.78 / 0.38	1.76(O-Ni)	0.78 / 0.38	1.76(O-Ni)
O spillover from Ni to SDC	1.41 / 1.38	1.95(O-Ce)	----	----
O migration from SDC surface to subsurface	0.19 / 0.76	2.03(O-Ce) 2.20(O-Sm)	0.50 / 1.22	2.18(O-Ce) 2.20(O-Sm)
Bulk O migration in SDC	0.61 / 0.92	2.13(O-Sm)	0.69 / 0.83	2.06(O-Sm)

3.3.3. CO $\rightarrow$ C +O

CO decomposition reaction has also been considered for the two models. The DFT energetics results show that, regardless of the models, the CO decomposition (carbon formation) energy barriers are much higher than that of CO_2 reduction. Therefore, CO dissociation is not included in the proposed reaction mechanism of CO_2 electroreduction and microkinetic analysis. The effects of different oxygen vacancy locations on the CO decomposition reaction are discussed in detail in the SI. The configurations are shown in the Supporting Information (Figure S3-3: a-d).

3.3.4. CO₂ Reduction Mechanism on Ni(111)/SDC Surface

The proposed reaction mechanisms for CO_2 electroreduction in the cases of Model 1 and Model 2 are shown in Figure 3-3. Due to its low energy barrier, the CO_2 reduction step at the interface of Ni-SDC was considered in the reaction mechanism on both Ni/SDC surface models with different locations of oxygen vacancies. The overall electrochemical reduction of CO_2 at the Ni-SDC cathode can be expressed as follows:

$$CO_{2(g)} + 2e' + V_O^{\cdot\cdot}(SDC) \rightarrow CO_{(g)} + O_O^{\times}(SDC)$$

where $V_O^{\cdot\cdot}$ denotes a doubly charged oxygen vacancy of SDC that has been formed before CO_2

reduction and $O_O^\times$ with two electrons is the surface oxygen ion of SDC.
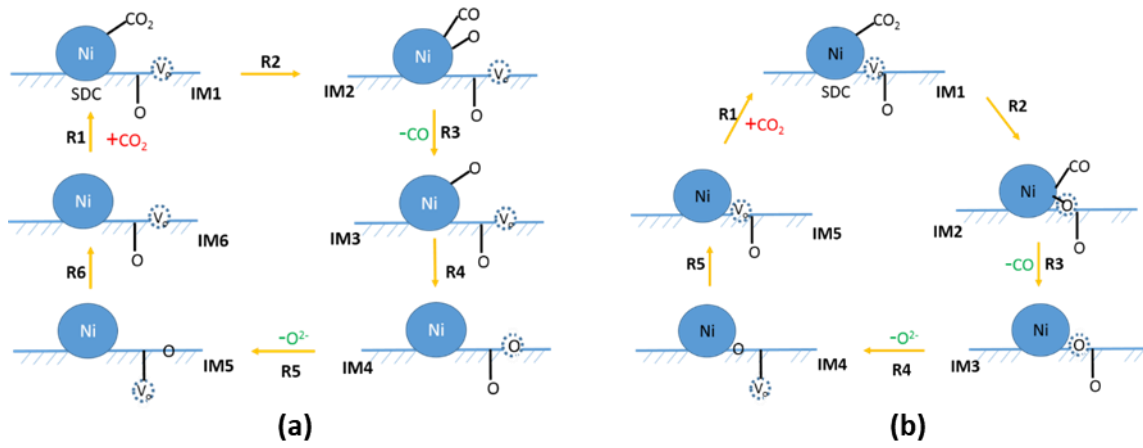
Figure 3-3. Proposed mechanism for CO_2 reduction on Ni-SDC without interface oxygen vacancy: (a): Model 1; (b): Model 2, the dashed circle represents the oxygen vacancy. IM represents intermediate species.

The proposed reaction mechanism consists of the following steps:

$$CO_{2(g)} + * (Ni) \rightarrow CO_2^* \qquad\qquad \text{R1 (Model 1 and Model 2)}$$

$$CO_2^* + * (Ni) \rightarrow CO^* + O^*(Ni) \qquad \text{R2 (Model 1 and Model 2)}$$

$$CO^* \rightarrow CO_{(g)} + * (Ni) \qquad\qquad \text{R3 (Model 1 and Model 2)}$$

$$O^*(Ni) + V_s \rightarrow O_s + * (Ni) \qquad \text{R4 (Model 1 only)}$$
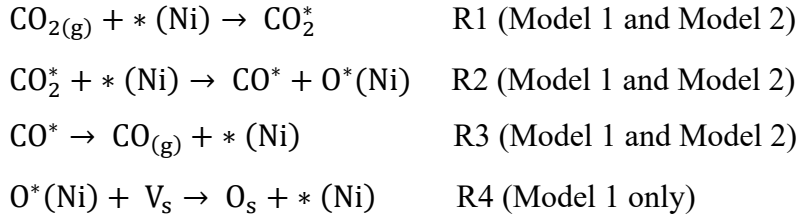
Herein, R1-3 represent the CO_2 adsorption, CO_2 reduction and CO desorption steps, respectively. R4 represents oxygen spillover from Ni to SDC surface. Vs denotes a non-interface surface oxygen vacancy and Os is a surface oxygen on SDC surface. CO_2 reduction mechanism in Model 2 is similar to that of Model 1, except that it does not include the oxygen spillover step from Ni to SDC surface (R4). This is because the CO_2 reduction reaction is prone to occur at the interface vacancy position, and the oxygen produced by CO_2 fills the interface vacancy of Model 2 (i.e. the surface vacancy of SDC).

To complete the reaction cycle, an oxygen removal step (R5) was introduced in the mechanism by assuming that this oxygen will be conducted through the electrolyte and become oxygen gas at the

49

anode. In fact, R5 includes two steps: oxygen migration from cathode SDC bulk to the SDC electrolyte (R5a) and gas oxygen formation (R5b), i.e.
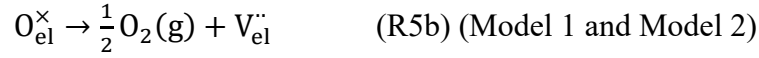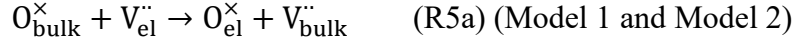
$$O_{bulk}^{\times} + V_{el}^{\cdot\cdot} \rightarrow O_{el}^{\times} + V_{bulk}^{\cdot\cdot} \qquad \text{(R5a) (Model 1 and Model 2)}$$

$$O_{el}^{\times} \rightarrow \frac{1}{2}O_2(g) + V_{el}^{\cdot\cdot} \qquad \text{(R5b) (Model 1 and Model 2)}$$

where, $V_{el}^{\cdot\cdot}$ and $V_{bulk}^{\cdot\cdot}$ represent the oxygen vacancy of electrolyte and SDC bulk, respectively, whereas $O_{el}^{\times}$ and $O_{bulk}^{\times}$ are the corresponding oxygen ion in electrolyte and SDC bulk. According to previous studies, oxygen evolution reaction at the anode side (R5b) is very fast at high temperatures (700-900°C) [164, 166]; therefore, it was assumed that the reaction rate of R5 is the same as that of R5a. As shown in Figure 3, the last step is oxygen migration from SDC surface to SDC bulk (R6):

$$O_s + V_{bulk} \rightarrow O_{bulk} + V_s \qquad \text{(R6) (Model 1 and Model 2)}$$

The energetics results of CO_2 reduction and oxygen migration are summarized in Table 3-1. The energy profile for the CO_2 reduction and oxygen migration processes in Model 1 and Model 2 are depicted in Figure 3-4. IM2 is Model 1(or 2) with adsorbed CO* and O* (Ni). Note that, with the exception of IM1 and IM2, the free energy of all the intermediate species reported in Figure 3-4 include the free energy of the CO gas molecule. The process from IM4-1 to IM4-2 is bulk oxygen removing process for Model 1. The energy difference between IM4-1 and IM4-2 is the bulk oxygen vacancy formation energy of pure SDC (-0.83 eV as shown in Figure S1). The process from IM3-1 to IM3-2 is bulk oxygen removing process for Model 2. The energy difference between IM3-1 and IM3-2 is also the bulk oxygen vacancy formation energy of pure SDC (-0.83 eV).
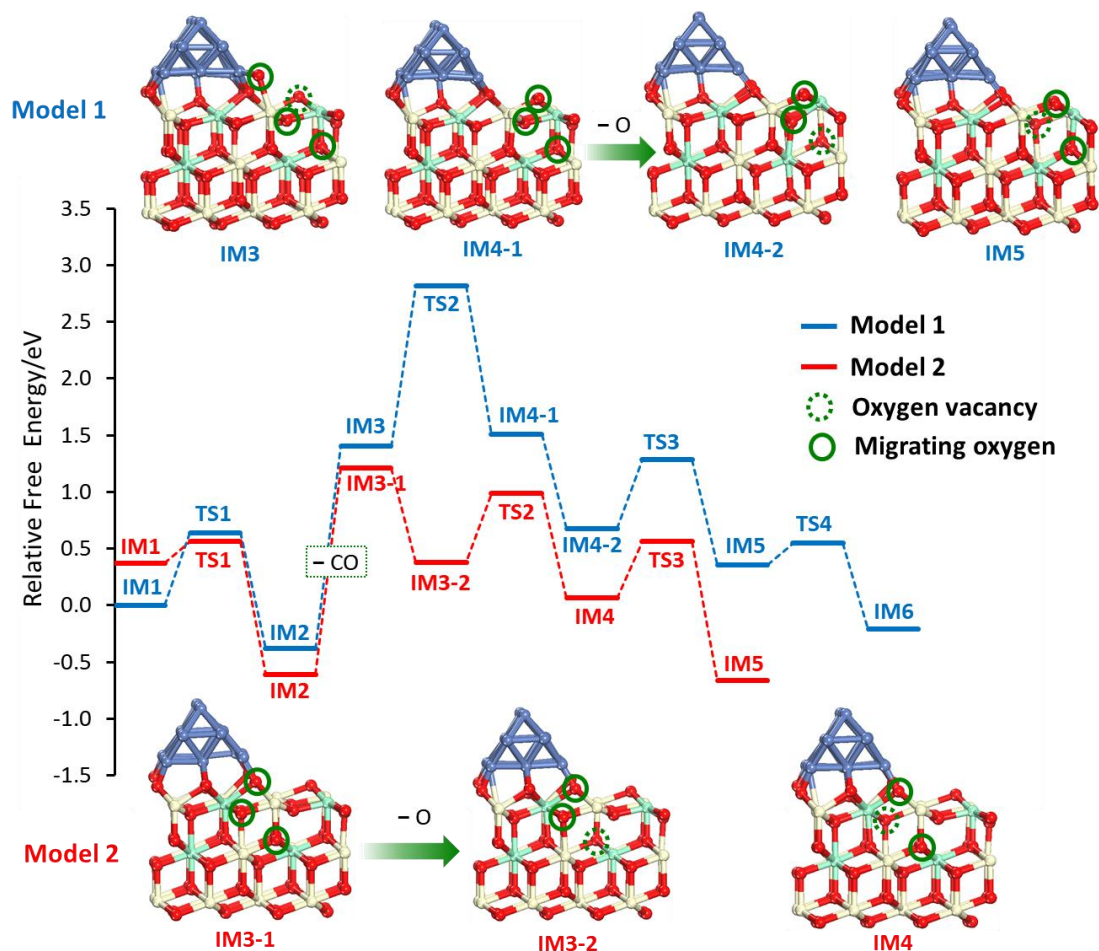
Figure 3-4. Energy profile for CO_2 reduction and oxygen migration processes on Ni-SDC with non-interface (Model 1, blue) and interface oxygen vacancy (Model 2, red). All energies are with reference to the energies of the initial state of Model 1 with adsorbed CO_2 (IM1 in blue). The insets provide a side view of the optimized structures of the intermediates. The transition states are listed in Table S3-4 and S3-5 in the Supporting Information.

The energetics of R1 to R3 for Model 1 and Model 2 are shown in Table 3-1 and Table S3-3. For Model 1, the spillover of oxygen from Ni to SDC surface (R4) proceeds with an activation barrier of 1.41 eV, and it is an endothermic process ($\Delta E = 0.03$ eV). The energy barrier of reaction R5 (oxygen migration: from subsurface to bulk) in SDC is found to be 0.61 eV and exothermic by -0.31 eV. R6 is considered as the oxygen migration process from the surface to the subsurface. The energy barrier is 0.19 eV and is exothermic by -0.57 eV. With regards to Model 2, bulk oxygen

migration (R4) has similar energy barrier (0.69 eV) to that observed for Model 1. Interface oxygen migration from the SDC surface to the subsurface (R5) has a slightly higher energy barrier (0.50 eV) than that for Model 1. This is because the interface oxygen atom is bonded with both Ce and Ni, making it difficult to migrate from the interface to the subsurface.

Based on the discussion above, two slightly different routes for CO_2 reduction and oxygen migration were proposed in Model 1 and Model 2. The energetic results were used to develop a microkinetic modeling, which is presented next.

3.4. Insights from Microkinetic Modeling

3.4.1. Microkinetic Analysis without Cathode Overpotentials

Microkinetic analysis for CO_2 reduction on Ni (111)/SDC was performed to deduce the rate controlling step based on DFT+U calculations. Rate constants for each elementary step are determined by the forward and backward energy barriers of the elementary steps, entropies and frequencies of involved species. Surface coverages of all adsorbed species and vacant sites, as well as the overall reaction rates were evaluated at steady state. In addition, to the authors' knowledge, the charge transfer steps for CO_2 electrochemical reduction have not been presented in the literature. In the present study, the possibilities involving one- or two- electron charge transfers were considered.

Table 3-2 and Table 3-3 summarize the forward reaction rates, X_{RC}, and equilibrium constants of all the elementary steps proposed for Model 1 and Model 2, respectively, without considering the effect of electrode overpotential. The SOEC operating conditions were set as follows: T= 1000 K, P_{CO_2}=0.7 atm, P_{CO}= 0.3 atm and P_{O_2}=0.21 atm (in air). These operating conditions were chosen in order to compare our simulation results with data reported in the literature [31, 58].

Table 3-2. The forward reaction rates, X_{RC}, and equilibrium constants of the elementary steps of Model 1 calculated at 1000K, P_{CO_2}=0.7 atm, P_{CO}= 0.3 atm and P_{O_2}=0.21 atm (in air) without considering the effect of electrode overpotential.

Reaction step	k_{for} (s^{-1})	K	X_{RC}	Forward rate (s^{-1})
R1	3.92×10^8	4.81×10^3	0.01	2.54×10^4
R2	1.15×10^9	1.19×10	0.02	3.24×10^4
R3	2.04×10^4	4.15×10^{-5}	0.06	1.42×10^4
R4	1.18×10^6	1.67×10^0	0.91	5.56×10^2
R5	8.11×10^9	4.19×10^1	0.00	8.87×10^7
R6	8.56×10^{11}	4.92×10^2	0.00	1.90×10^7

Table 3-3. The forward rates, X_{RC}, and equilibrium constants of the elementary steps of Model 2 calculated at 1000K, P_{CO_2}=0.7 atm, P_{CO}= 0.3 atm and P_{O_2}=0.21 atm (in air) without considering the effect of electrode overpotential.

Reaction step	k_{for} (s^{-1})	K	X_{RC}	Forward rate (s^{-1})
R1	3.92×10^8	1.62×10^7	0.35	1.17×10^4
R2	9.83×10^{11}	2.09×10^5	0.00	1.18×10^4
R3	1.81×10^4	3.67×10^{-5}	0.65	1.81×10^4
R5	8.11×10^9	4.19×10^1	0.00	8.87×10^7
R6	1.29×10^{10}	2.53×10^3	0.00	6.77×10^4

In Campbell's theory [212], the larger the numeric value of $X_{RC,i}$ is for a given step, the larger the influence of its rate constant on the overall reaction rate r. Therefore, Campbell's degree of rate control analysis indicates that the oxygen spillover step (R4) is the rate-controlling process for

Model 1, whereas the CO desorption step (R3) is the rate-controlling step for Model 2. Note that the CO desorption entropy change calculated with the other method [219] do not change current conclusion. The calculation details are discussed in the Supporting Information. CO adsorption energy calculated by hybrid functional HSE06 [220-223] has very little difference (< 0.1 eV) compared to that using GGA+U functional, and also do not change the current conclusion.

The overall rate ($r_{overall} = r_i = r_{i,forward} - r_{i,backward}$ (i=1-6)) is 5.56×10^2 s^{-1} for Model 1 and 1.17×10^4 s^{-1} for Model 2. In the absence of cathode overpotential, the microkinetic analysis predicts that the overall rate of Model 2 is two-order of magnitudes higher than that of Model 1. This trend is expected since CO_2 reduction presents a lower energy barrier in Model 2, and there is no oxygen spillover step.

3.4.2. Effects of Electrode Overpotentials

Potentials of 0-0.3 V vs. open circuit voltage (OCV) are considered in this study. At high potentials, it is reported that mass transfer is always the limiting step for CO_2 electrolysis [224, 225].

When the electrode overpotential is taken into account, the rate constants for surface reactions involving charge transfer were modified.

In the proposed CO_2 reduction mechanism, there are four elementary steps for Model 1 (R1-R4) and three steps for Model 2 (R1-R3), involving Ni cluster sites. Since Ni is governing the electronic conductivity of SOEC, these elementary steps can be affected by the cathode bias potential. They can be further classified as follows: i) surface adsorption (or desorption) (R1, R3 for both models); ii) surface reactions (R2 and R4 for Model 1; R2 for Model 2).

For surface adsorption and desorption, the potential drop across the cathode/electrolyte interface, caused by electrochemical double layer, can induce an electric field and affect the binding energies

of surface species [226]. Therefore, DFT calculations with a uniform electric field (from 0 to 0.5 V/Å), were performed to investigate the effects of electric field on the adsorption energies of CO_2 and CO. A typical magnitude of the electric field in the electrochemical double layer is about 0.5 V/Å in SOFC [226]. In the present study, the electric field was introduced by inducing an artificial dipole layer in the middle of the vacuum layer [226, 227]. This approach was proposed by Neugebauer and Scheffler [228]. The potential energy profile of the Ni/SDC system [227] is shown in Figure S3-4 in the SI. That figure shows that this uniform electric field has significantly more effects on the interface of Ni/SDC than on the SDC bulk. Also, a previous report has indicated that the electric field only has minor effects (less than 0.02 eV) on the binding energies of oxygen on Ni (111) surface [226]. Hence, only the effects of electric field on the adsorption of CO_2 and CO are considered. The field-induced changes in the binding energy of CO_2 and CO adsorbed at the interface of Ni and SDC were calculated as follows:

$$\Delta E_{ads} = E_{ads}(\text{with electric field}) - E_{ads}(\text{without electric field}) \qquad (3\text{-}16)$$

Figure 3-5 indicates that, under an electric field smaller than 0.5 V/Å, the effects of the electric field on the adsorption energies of CO_2 and CO are small (< 0.03 eV). This result is expected, because these species are not ionic and should not be severely affected by an electric field. Therefore, effects of electric field on CO_2 adsorption and CO desorption can be neglected.
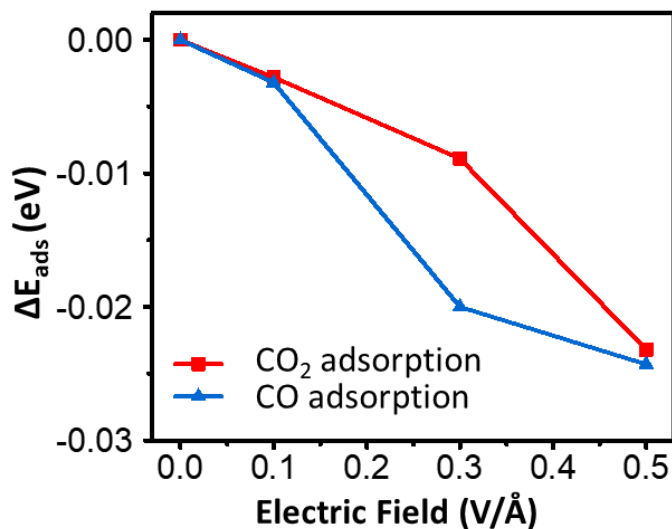
Figure 3-5. Field-induced change in the binding energies of CO_2 and CO adsorbed at the interface of Ni and SDC.

Hence, only effect of electric field was considered for charge transfer reactions. In addition, both one- or two-electron charge transfer processes were considered. The overall reaction of CO_2 electrolysis in SOEC involves two electrons' transfer in total. Herein, three situations were considered for Model 1: i) two-electron charge transfer for R2 (this will be referred to as T2); ii) two-electron charge transfer for R4 (this will be referred to as T4); iii) one-electron charge transfer for R2 and R4 (this will be referred to as O24). For Model 2, there is only one situation: two-electron charge transfer for R2. The corrected forward and backward rate constants were implemented in the microkinetic model to recalculate the surface coverages and rates at the applied voltage. The calculated rate constants and equilibrium constants for the four possibilities of charge transfer steps at a representative electrode overpotential of 0.3V (relatively low potential) and at a temperature of 1000 K are presented in Table S3-6 of the SI.

Table 3-4. The overall rates and the rate control factors X_{RC} for the four situations at a cathode bias potential of 0.3 V calculated at 1000K.

Model	Charge transfer step	X_{RC} (Rate-controlling step)	Overall rate (s^{-1})
	R2	0.64 (R3)	1.22×10^4
Model 1	R4	0.41 (R3)	5.39×10^3
	R2+R4	0.60 (R3)	9.81×10^3
Model 2	R2	0.65 (R3)	1.17×10^4

Table 3-4 summarizes the overall rates calculated for the four possibilities of charge transfer steps, and the corresponding rate control factors determined using Campbell's analysis at a cathode bias potential of $\eta = 0.3$ V. The results indicate that CO desorption (R3) is always the rate-controlling step at the bias potential of $\eta = 0.3$ V for both models. This result is reasonable because studies have found that CO_2 reduction is hindered on the CO poisoned transition metals which suggests that catalysts are strongly bonded with CO [229].

Comparison of Table 3-2 and Table 3-4 shows that the maximum overall rate obtained at $\eta = 0.3$ V $(1.22 \times 10^4 \text{ s}^{-1})$ is almost two orders of magnitude higher than the rate at $\eta = 0$ V for Model 1. This reflects the promoting effect of applied potential on CO_2 reduction. However, by considering the effect of potential, the overall rates and rate controlling step of Model 2 remain unchanged. This is because X_{RC} for the charge transfer step R2 is approximately 0 which means that this step has almost no effect to the overall rates. Therefore, the rate constants of R2 modified by the potential will not affect the overall rates and rate controlling step when R2 is the charge transfer step. Moreover, the micro-kinetics analysis exhibits that with the increase of electrode overpotential from 0 to 0.3 V, the rate controlling step of Model 2 is unaltered which is the CO desorption step (R3).

Figure 3-6 shows that the rate-controlling steps changes from oxygen spillover (R4) to CO desorption (R3) when the electrode overpotentials are increased in the three charge transfer pathways for Model 1.
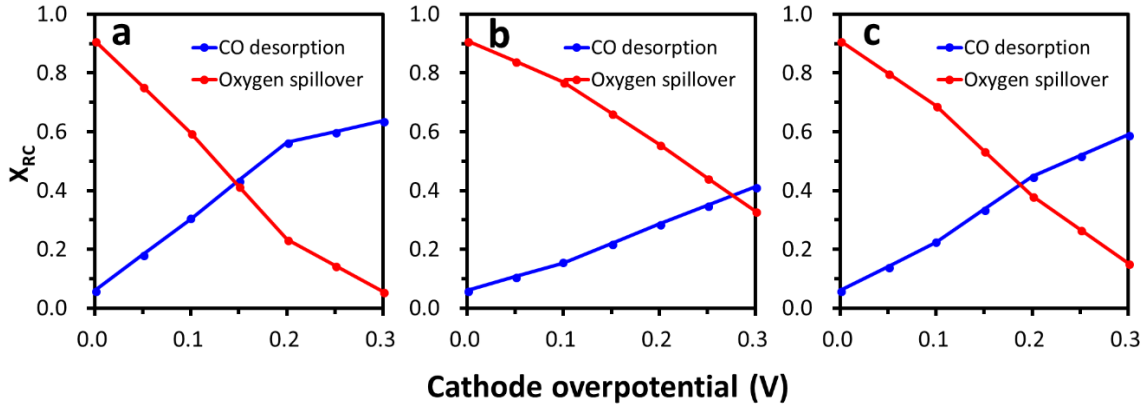
Figure 3-6. Campbell's degree of rate control (X_{RC}) analysis of CO_2 reduction for Model 1 as a function of electrode overpotentials (T = 1000 K). (a): Two-electron charge transfer for R2 (T2); (b): Two-electron charge transfer for R4 (T4); (c): One-electron charge transfer for R2 and R4 (O24).

3.4.3. Polarization Curves

The kinetic relationship between cell voltage and current density is represented by the simulated polarization curves. To simplify the calculations, this study assumed that: i) mass transfer is not the limiting step under low overpotentials; ii) ohmic losses are neglected due to the high ionic conductivity of SDC; and iii) anode potential is fixed at its equilibrium potential. Thus, the cell voltage vs. OCV is equal to the cathode bias potential in this study. The current density is calculated using the Butler-Volmer Equation, $i = zer\Gamma$ [225], where i denotes the current density (A·cm^{-2}), z is the number of electrons involved in the overall reaction, r represents the overall reaction rate (s^{-1}) calculated from microkinetic model, and Γ is the number of active sites per surface area (cm^{-2}). The simulated polarization curves of three charge-transfer possibilities for Model 1 are depicted in Figure 7. The dash black-line in that figure represents the experimental polarization curve [53] for a

solid oxide electrolysis button cell with Ni/YSZ as cathode at the operating condition of 700°C (973K) and CO_2/CO molar ratio of 2/1, which are similar operating conditions for which the present model is valid.
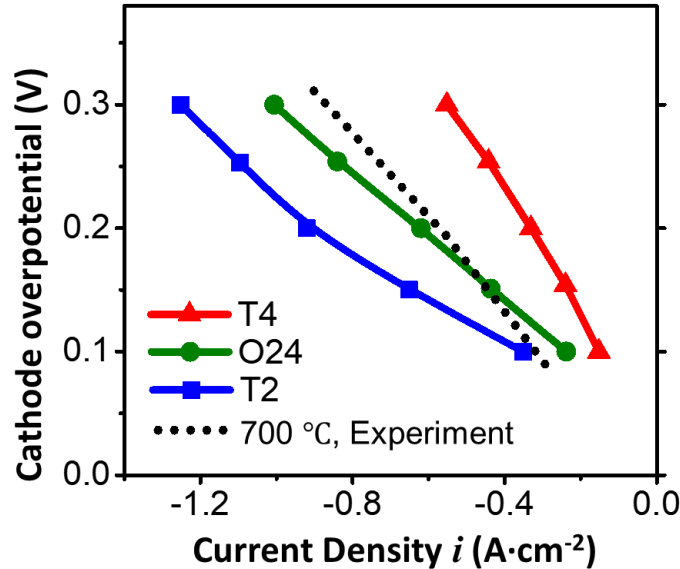
Figure 3-7. Simulated polarization curves of 3 situations of CO_2 reduction for Model 1 calculated at 1000K. (Blue line: Two-electron charge transfer for R2 (T2); red line: Two-electron charge transfer for R4 (T4); green line: One-electron charge transfer for R2 and R4 (O24).) The dash line is experimental polarization curve [53] for a solid oxide electrolysis button cell with Ni/YSZ as cathode (700◦C with CO_2/CO molar ratio of 2/1).

As shown in Figure 3-7, the polarization curves are consistent with experimental observations at low cathode overpotentials (0-0.3V), i.e. the current density increases with increasing cell voltages [31, 58]. However, at higher overpotentials, the simulated results deviate from the experiments. This is because, at large overpotentials, mass transfer becomes the limiting step for the electrolysis of CO_2 [224, 225], which is not considered in the present microkinetic model. Note that the analysis shows that the two-electrons charge transfer on R2 (T2) yields higher current density than the other pathways (T4 and O24). As we mentioned, compared to YSZ, SDC exhibit higher ionic conductivity at intermediate temperatures (600-750°C) [28-30]. Therefore, it can be speculated that

Ni/SDC has relatively better performance than Ni/YSZ at 700°C. The polarization curve for the SOEC with Ni/SDC cathode would shift slightly left compared with that of Ni/YSZ in Figure 3-7. These results may indicate that two-electron charge transfer for R4 (T4) is most unlikely to occur in the actual setting due to its most deviation with experiment data; however, the sensitivity of other key parameters on the system (e.g. thickness of the electrolyte) is needed to further support the electron charge transfer mechanisms in this system.

As for the polarization curves for Model 2, the current density remains constant with increasing cell voltage (Figure S3-5 in the SI), which is not reasonable. This is because CO desorption (R3) is the rate-controlling step in Model 2 regardless of the potential. As discussed before, the modification of rate constants for the charge transfer step R2 under applied potentials has no effects to the overall rate. Constant overall rate leads to the unchanged current density. Herein, Model 2 may account for a small fraction in an actual situation because its polarization curves may deviate significantly from experimental results for Ni/SDC cathode of SOEC. This is predictable since the interface oxygen vacancy of Model 2 is more difficult to form compared with other surface oxygen vacancies. Note that at low cathode overpotential (0-0.3V), the current density of Model 2 (~1.2 $A \cdot cm^{-2}$) is higher than that of Model 1. This also reveals that Ni-SDC with interface oxygen vacancies facilitates CO_2 reduction process. Insufficient adsorption of CO_2 is also the limitation that leads to the local starvation of CO_2, thus restricting the current efficiency and cell performance [229-231]. Therefore, introducing more interface oxygen vacancies is critical to SOEC performance.

3.5. Summary

To achieve the objective 1 (a) and (b) of this thesis, i.e. elucidating CO_2 electroreduction

mechanism for Ni/SDC, a DFT based microkinetic modeling study under SOEC operating conditions was performed and used to gain insight on the overall CO_2 reduction process on Ni/SDC cathode and to determine the rate-controlling steps. The DFT study performed in this part of the research found out that the interface oxygen vacancy can enhance CO_2 adsorption and further promote CO_2 reduction by lowering its energy barrier. Considering the effect of electric potential and possibility of one- or two-electron charge transfer processes at various elementary steps, a microkinetic analysis has shown that the rate-controlling step changed from the oxygen spillover step to the CO desorption step with an increase in cathode overpotential on Ni(111)/SDC surface with non-interface oxygen vacancy (Model 1). However, once interface oxygen vacancy is considered (i.e. Model 2), the results indicate that CO desorption is the dominating rate-controlling step regardless of the cathode overpotential. This model also has some limitations, e.g. lacking consideration of ionic conduction, gas diffusion, and the thickness of electrode and electrolyte effects, which motivated the development of more detailed multiphysics model, which is the main subject presented in the next Chapter.

Chapter 4. CO₂ Electrolysis at Ni/SDC Cathode by Coupled Ab-initio and Multiphysics Simulations

The microkinetic modelling presented in the previous Chapter cannot consider ionic conduction, gas diffusion, and the thickness of electrode and electrolyte effects. To study the CO_2 electrolysis process at a larger scale by considering ionic/electronic conduction and transport processes, a DFT-based multiphysics model for CO_2 reduction at the cathode of Ni/ SDC in SOEC was developed for a cathode supported button cell. Compared to the current multi-physics SOEC models: the present study considers the following features: 1) the pre-exponential factors and activation energies for each elementary step were determined from DFT. 2) three reaction mechanisms were proposed for the first time to describe the charge transfer steps. Sensitivity analysis, the effects of CO/CO_2 ratio and temperature, and the spatial distributions of adsorbate species, in particular carbon deposition, are presented in this Chapter.

4.1. Introduction

Identifying optimal conditions for electrochemical cell operation requires knowledge of the CO_2 reduction mechanism. Compared with experimental analysis, computational modelling and simulation are more effective tools to investigate the underlying mechanisms of CO_2 reduction in SOEC, especially to study surface adsorbate distributions, in particular when their coverages are too low to be detected, or hardly accessible using experimental tests.

Multiscale models with elementary reaction kinetics through coupled ab-initio calculations and physics-based simulation are crucial to provide more detailed and accurate mechanistic insights into CO_2 reduction in SOEC. However, there are still no reported studies about that. Although the current computational models with fitted kinetic data work well in many circumstances, developing

a robust DFT-based multi-scale model is also essential to avoid time-consuming and expensive procedures [38, 43].

Elementary reaction kinetics should be incorporated in the computational models to provide insights in revealing the reaction mechanisms. In fact, many mathematical models have been developed with detailed heterogeneous chemistry, coupled with ionic/electronic conduction and gas-phase transport for CO_2 electrolysis in SOEC. However, most of the current models in SOEC are 1D models [56, 179, 184, 188]. 1D geometry does not represent a real cell, even the simplest button cell. In addition, they are usually unable to represent accurately boundary conditions at the inlet/outlet of the cell. On the other hand, 2D models are accurate representations of button cell because of the axisymmetry of such cell. Until now, there is only one 2D SOEC model with detailed heterogeneous catalysis and electrochemical reactions reported in the open literature [183]. Most of the previous reported studies used the kinetic data from [232], for which many kinetic data were obtained from unity bond index-quadratic exponential potential (UBI-QEP) method; however, many were subsequently modified to make the model thermodynamic consistent. In addition, UBI-QEP employs a few thermodynamic observables (gas-phase bond energies and atomic chemisorption energies) which DFT does not require [233].

In addition, there is still a gap in the literature regarding the most likely reaction mechanism of charge transfer step. One-step oxygen ion spillover from Ni surface to YSZ surface, i.e. $O^{2-}(Ni) +$ (YSZ) $\leftrightarrow O^{2-}(YSZ) + Ni(s)$, is used to describe the charge transfer step [183-185]. Two-step charge-transfer mechanism was also used to describe the reaction and transfer processes of CO-CO_2 electrochemical conversion. For example, Yurkiv et al. [186] investigated three different spillover mechanisms for electrochemical CO oxidation at Ni/YSZ anodes. That study reported that the best agreement with the experimental data was obtained when two consecutive single-

electron charge-transfer steps from $O^{2-}(YSZ)$ via $O^-(YSZ)$ to $O(Ni)$ were considered. Shi et al. [187] developed an elementary reaction model for reversible $CO-CO_2$ electrochemical conversion to couple two charge-transfer reactions, i.e. $C(Ni)+O^{2-}(YSZ) \leftrightarrow CO(Ni)+(YSZ)+2e^-$ and $CO(Ni)+O^{2-}(YSZ) \leftrightarrow CO_2(Ni)+(YSZ)+2e^-$.

However, CO_2 reduction on Ni surface and the following oxygen spillover step from Ni to YSZ are all key surface reactions at the TPB. The possible charge transfer step could be: i) the two-electron charge-transfer step for interface electrochemical reaction $(CO_2(Ni)+(Ni)+2e^- \leftrightarrow CO(Ni)+O^{2-}(Ni))$; ii) the two-electron charge-transfer step for $O^{2-}(Ni) + (YSZ) \leftrightarrow O^{2-}(YSZ) + Ni(s)$, or iii) the two consecutive single-electron charge-transfer steps involving these two reactions. $CO_2(Ni) + (Ni)+e^- \leftrightarrow CO(Ni)+O^-(Ni)$ and $O^-(Ni) + (YSZ) +e^- \leftrightarrow O^{2-}(YSZ) + Ni(s)$. Having access to this insight allows the identification of the mechanism that leads to a dependence of species coverage on the applied voltage and offers more accurate predictions for the experimental phenomena.

In the present study, a DFT-based 2D multi-scale model for SOEC button cell was built to validate the proposed reaction mechanisms obtained from DFT calculations. Compared to the previously reported models, the present model not only adopted the pre-exponential factors and activation energies of each elementary step calculated from DFT, but also considered three possible charge transfer steps. The multi-physics model includes coupled elementary catalytic and electrochemical reactions, ionic/electronic conduction, and transport processes within the cell. Comparison between experimental and simulated polarization curves were carried out to determine the most possible reaction mechanism. Also, a sensitivity analysis was performed to analyze the impact of every elementary step on the current density, and thereby determine the rate controlling step. The effect of CO/CO_2 ratio and the 2D spatial distributions of gas and adsorbate species were analyzed to provide a better understanding of CO_2 electrolysis process in SOEC.

4.2. Model Development and Governing Equations

4.2.1. Geometry and Assumptions

The 3D geometry, as shown in Figure 4-1(a), represents the SOEC button cell (green region) and the corresponding gas channels for both anode (orange region) and cathode (blue region). Figure 4-1(b) shows the computational domain of the 2D continuum transport model used in the present study. A cathode supported SOEC cell was adopted in this study. It consists of a Ni/SDC negative electrode support layer (500 μm), a YSZ electrolyte layer (20 μm), and a lanthanum strontium manganate (LSM) anode (15 μm). The diameter of the anode is 1.3 cm, and the diameter of the remaining layers is 2.6 cm. The thickness of the wall in between the inner and outer fuel channel is 1mm. These dimensions were built referring to a previously reported cathode supported SOEC study [58] so as to make the results of this study comparable with the aforementioned experimental study. The anode electrode is exposed to the ambient air. The fuel channel is feed with CO/CO_2 gas mixtures. Figure 4-1(c) illustrates the microkinetic model showing the TPB and the main elementary reactions for CO_2 reduction over Ni/SDC, which are coupled with the continuum model. Figure 4-1(d) depicts the Ni(111)/SDC surface model used for the kinetics calculations of the elementary steps using DFT.

The assumptions made in the present model are as follows: (1) the model is isothermal; (2) the gas mixtures are assumed to be ideal gases; (3) heterogeneous thermochemical and electrochemical reactions are assumed to take place on both the Ni and SDC surfaces; the active reaction sites are assumed to be uniformly distributed; (4) the oxygen ion transfer reaction from SDC to YSZ is neglected due to their similar properties as ceramic materials [28, 29]. Because the focus of the present work is on the cathode, only a global reaction is considered at the anode.
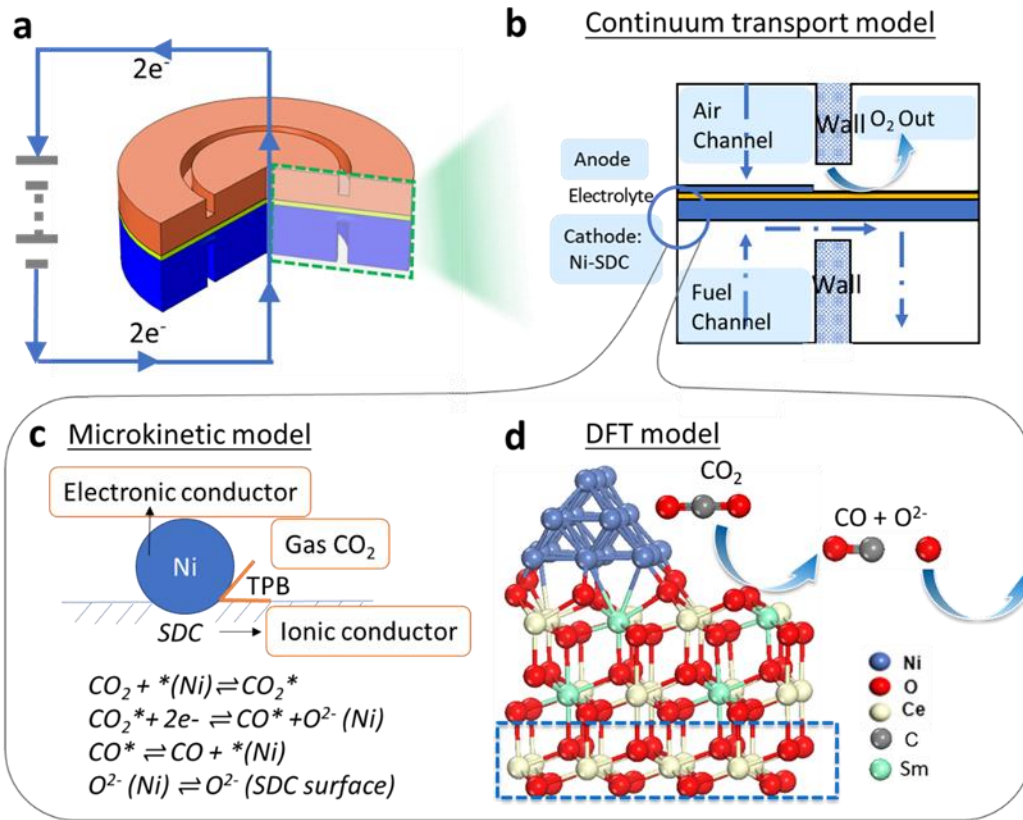
Figure 4-1. (a) Schematic of SOEC button cell and gas channel; (b) 2D continuum transport model used in the present study. (c) Microkinetic model showing the triple phase boundary (TPB) and main elementary reactions for CO_2 reduction over Ni/SDC, which is coupled with the continuum model. (d) The Ni(111)/SDC surface model used for the DFT kinetics calculations of the elementary steps.

4.2.2. Heterogeneous Chemistry

In the cathode, the CO_2 reduction mechanism on Ni(111)/SDC surface and reaction kinetic data calculated from DFT for every elementary step from one of our previous studies [52] were used in this study. Arrhenius parameters for the rate constants k are formulated as follows:

$$k = A T^n exp\left(-\frac{E_a}{RT}\right) \tag{4-1}$$

where A, n and E_a are the pre-exponential factor, temperature exponent and activation energy, respectively. The pre-exponential factor of the surface reactions and desorption were calculated from the vibrational frequencies using DFT [52]. E_a was also obtained from DFT analysis. The

66

complete reaction mechanism for SOEC CO_2 reduction, composed of 10 reactions at the cathode, is shown in Table 4-1. Reaction r11 is the oxygen evolution reaction at the anode. The current density in the anode is expressed by the global Butler-Volmer equation (equation 12 in Table 4-2). The reaction $O(s) + O(s) \leftrightarrow O_2 + Ni(s) + Ni(s)$ is neglected due to the extremely low partial oxygen pressure (10^{-20} atm) in the cathode during CO_2 electrolysis [37, 49, 57].

Table 4-1. Heterogeneous reaction mechanism for CO_2 electrolysis in SOEC.

No.	Reactions	A (cm, mol, s)[a]	n[a]	E_a (J/mol)[a]
	Adsorption and Desorption on Ni surface			
r1	$CO_2 + Ni(s) \rightarrow CO_2(s)$	1.000×10^{-04} [b]	-	0
r2	$CO_2(s) \rightarrow CO_2 + Ni(s)$	$3.433 \times 10^{+05}$	0.0	49920
r3	$CO + Ni(s) \rightarrow CO(s)$	4.000×10^{-02} [b]	-	0
r4	$CO(s) \rightarrow CO + Ni(s)$	$6.989 \times 10^{+10}$	0.0	174720
	Surface reactions on Ni surface			
r5	$CO_2(s) + Ni(s) \rightarrow CO(s) + O(s)$	$3.569 \times 10^{+21}$	0.0	87360
r6	$CO(s) + O(s) \rightarrow CO_2(s) + Ni(s)$	$2.567 \times 10^{+21}$	0.0	144960
r7	$CO(s) + Ni(s) \rightarrow C(s) + O(s)$	$1.530 \times 10^{+22}$	0.0	368640
r8	$C(s) + O(s) \rightarrow CO(s) + Ni(s)$	$6.752 \times 10^{+23}$	0.0	275520
	Transfer of oxygen ions			
r9	$O(s) + V_{SDC}^{\cdot\cdot} \rightarrow O(SDC) + Ni(s)$	$2.837 \times 10^{+22}$	0.0	135360
r10	$O(SDC) + Ni(s) \rightarrow O(s) + V_{SDC}^{\cdot\cdot}$	$1.201 \times 10^{+22}$	0.0	132480
r11	$O_{YSZ}^{2-} \rightarrow \frac{1}{2} O_2 + 2e^- + (YSZ)$	Global Butler-Volmer		

[a] Arrhenius parameters for the rate constants are written in the form: $k = AT^n * \exp(-Ea/RT)$.

[b] Sticking coefficient.

4.2.3. Electrochemistry

When the electrode overpotential is taken into account, the following equations were used to modify the rate constants for surface reactions involving charge transfer. The forward $k_{f,CT}$, and reverse $k_{r,CT}$, charge transfer (CT) reaction rate constants are as follows:

$$k_{f,CT} = k_{f,CT}^0 \exp\left(-\frac{E_{f,CT}^a}{RT}\right) \exp\left(\frac{\beta zF}{RT}\eta_{ca}\right) \tag{4-2}$$

$$k_{r,CT} = k_{r,CT}^0 \exp\left(-\frac{E_{r,CT}^a}{RT}\right) \exp\left(\frac{-(1-\beta)zF}{RT}\eta_{ca}\right) \tag{4-3}$$

where $k_{f,CT}^0$ and $k_{r,CT}^0$ are the pre-exponential factors; $E_{f,CT}^a$ and $E_{r,CT}^a$ are the thermal activation energies; z is the number of electrons transferred in the electrochemical reaction, β is the charge transfer coefficient, η_{ca} is the cathodic overpotential (V), and F is the Faraday constant (96,487 $C\cdot mol^{-1}$).

The overall electrochemical reduction of CO_2 at the Ni-SDC cathode can be expressed as follows:

$$CO_{2(g)} + 2e^- + V_O^{\cdot\cdot}(SDC) \rightarrow CO_{(g)} + O_O^{\times}(SDC) \tag{4-4}$$
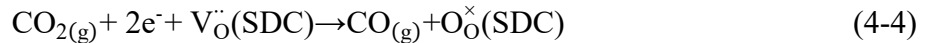
In the present study, the possibilities of charge transfer steps involving one-or two-electron charge transfers were considered. The overall reaction of CO_2 electrolysis in SOEC involves two electrons' transfer in total. Herein, three reaction mechanisms were considered, as shown in Figure 4-2: i) reaction mechanism 1: two-electron charge transfer for CO_2 reduction step: $CO_2(s) + Ni(s) + 2e^- \leftrightarrow CO(s) + O^{2-}(s)$; ii) reaction mechanism 2: one-electron charge transfer for CO_2 reduction step and oxygen spillover step respectively; and iii) reaction mechanism 3: two-electron charge transfer for oxygen spillover step: $O^{2-}(s) + V_{SDC}^{\cdot\cdot} \leftrightarrow O_{SDC}^{2-} + Ni(s)$. These charge transfers are chosen because the CO_2 reduction step and oxygen spillover step are the main elementary surface reactions (except the surface adsorption/desorption and carbon formation).
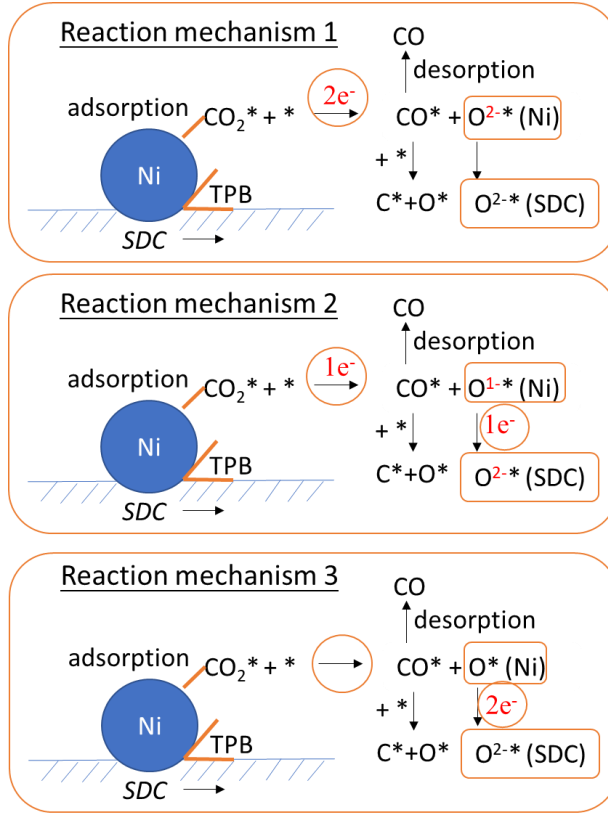
Figure 4-2. Three reaction mechanisms involving different charge transfer steps.

4.2.4. Governing Equations

The present model integrates detailed elementary chemical and electrochemical reactions with ionic/electronic conduction and gas transport processes in SOEC. The main governing equations, including heterogeneous chemistry/electrochemistry, mass conservation, charge conservation and momentum conservation, are summarized in Table 4-2. The nomenclature section of this study provides the definition for each of the variables and parameters listed in Table 4-2 and used throughout the manuscript. More details about the model can be found elsewhere [57, 58, 188].

Note that for surface chemistry, the reaction rate is usually expressed as a function of the surface coverage θ_i, which is defined as follows [234]:

$$\theta_i = \frac{c_i}{\Gamma} \tag{4-5}$$

69

where c_i is the concentration of species i (mol·m^{-2}) and Γ is the area-specific density of Ni (mol·m^{-}

^{2}). The uncovered Ni surface is treated as a dummy surface species.

<div align="center">Table 4-2. Main SOEC cell governing equations [57, 58]</div>

Heterogeneous chemistry and electrochemistry		No.
Reaction rate constant of surface reactions and desorption reactions in Arrhenius form (m, mol, s)	$k_m = A_m T^{\beta_m} exp\left(-\dfrac{E_m}{RT}\right) \prod_{k=1}^{K_s} \theta_i^{\mu_{km}} exp\left(-\dfrac{\varepsilon_{km}\theta_i}{RT}\right)$	(4-6)
Net production rate for species i (mol·m^{-2})	$s_i = \sum_m (v_i'' - v_i')\left(k_{f,m} \prod_{R_{f,m}} c_i^{v_i'} - k_{r,m} \prod_{R_{r,m}} c_i^{v_i''} \right)$	(4-7)
Charge transfer (CT) reaction rates (mol·m^{-2})	$r_m = k_{f,CT} \prod_{R_{f,m}} c_i^{v_i'} - k_{r,CT} \prod_{R_{r,m}} c_i^{v_i''}$	(4-8)
Charge transfer		
Ionic charge conservation at the electrolyte	$\nabla \cdot (-\sigma_{\text{ion, elyte}} \nabla V_{\text{ion, elyte}}) = 0$	(4-9)
Electronic and ionic charge conservation at the anode and the cathode	$\nabla \cdot (-\sigma_{\text{elec}}^{\text{eff}} \nabla V_{\text{elec}}) = Q_{elec} = -\nabla \cdot (-\sigma_{\text{ion}}^{\text{eff}} \nabla V_{\text{ion}}) = -Q_{ion}$	(4-10)
Current source derived from electrochemical reactions in the cathode (A·m^{-3})	$Q_{ca} = 2F \times S_{TPB,ca} \times \sum_m r_m$	(4-11)
Exchange current density in the anode (A·m^{-2})	$i_{0,an} = \dfrac{\gamma RT}{4F} exp\left(-\dfrac{E_{an}}{RT}\right) (P_{O_2}^{an})^{0.25}$	(4-12)

Global Butler-Volmer expression for the current source in the anode (A·m^{-3})	$Q_{ion,an} = -i_{0,an}S_{TPB,an}$ $\times \left(\dfrac{c_{O_2}^{TPB}}{c_{O_2}^{bulk}} exp\left(\dfrac{\alpha zF\eta_{ca}}{RT}\right) \right.$ $\left. - exp\left(-\dfrac{(1-\alpha)zF\eta_{ca}}{RT}\right) \right)$	(4-13)
Overpotential at the cathode (V)	$\eta_{ca} = V_{elec,ca} - V_{ion,ca} - V_{ref,ca}$	(4-14)
Overpotential at the anode (V)	$\eta_{an} = V_{elec,an} - V_{ion,an} - V_{ref,an}$	(4-15)
Applied voltage (V)	$V_{cell} = V_{ref,an} - V_{ref,ca} + \eta$	(4-16)
Open circuit voltage (V)	$OCV = \dfrac{-\Delta G^0}{nF} - \dfrac{RT}{nF} * ln\left(\dfrac{C_{CO}(C_{O_2})^{0.5}}{C_{CO_2}}\right)$	(4-17)

Mass transfer

Gas transport in the porous electrodes as well as fuel/gas supply channel (extended Fick's model (EFM))	$\varepsilon\dfrac{\partial c_{i,g}}{\partial t} + \nabla\left(-D_i^{eff}\nabla c_{i,g}\right) + u\nabla c_{i,g} = s_{i,g}$	(4-18)
Effective diffusivity of gaseous species (m^2 s^{-1})	$D_i^{eff} = \left(\dfrac{1}{D_{i,mole}^{eff}} + \dfrac{1}{D_{i,kn}^{eff}}\right)^{-1}$	(4-19)
Effective molecular diffusion coefficient (m^2 s^{-1})	$D_{i,mole}^{eff} = \dfrac{1 - x_i}{\sum_{j=1,\neq i}^{n}(x_j/D_{i,j}^{eff})}$	(4-20)
Effective binary molecular diffusion coefficient (m^2 s^{-1})	$D_{i,j}^{eff} = \dfrac{\varepsilon}{\tau}D_{i,j} = \dfrac{0.00101\varepsilon T^{1.75}(\frac{1}{M_i} + \frac{1}{M_j})^{1/2}}{\tau P(V_i^{\frac{1}{3}} + V_j^{1/3})^2}$	(4-21)
Effective Knudsen diffusion coefficient (m^2 s^{-1})	$D_{i,kn}^{eff} = \dfrac{\varepsilon}{\tau}D_{i,kn} = \dfrac{4}{3}\dfrac{\varepsilon}{\tau}r_p\sqrt{\dfrac{8RT}{\pi M_i}}$	(4-22)

Momentum conservation

| Brinkman equation and the Darcy's law (in the fuel/gas supply channel and porous electrodes) | $\rho\frac{\partial u}{\partial t}+\rho(u\cdot\nabla)u = \nabla\cdot\left[-PI + \mu(\nabla u + (\nabla u)^T) - \frac{2\mu}{3}(\nabla u)I\right] + F - \frac{K}{\mu}\nabla P$ | (4-23) |

The cathode reference potential $V_{ref,ca}$ was set to zero. Then $V_{ref,an}$ equals to the Open circuit voltage (OCV).

4.2.5. Model Parameters and Boundary Conditions

The operating parameters used in this study are summarized in Table 4-3. The cathode supported SOEC geometry and model parameters were taken from a previous experimental work [58].

Table 4-3. Operating parameters[57, 58, 188]

Parameters	Value	Units
Cathode		
Thickness (H), radius (r)	5.0×10^{-4}, 1.3×10^{-2}	m
Porosity (ε)	0.4	
Tortuosity(τ)	1.2	
Ni electronic conductivity(σ_{Ni})	$(3.27\times10^6-1060.3[1/K]\times T)$	s•m^{-1}
Surface site density of Ni (Γ)	5.1×10^{-5}	mol•m^{-2}
Effective TPB area ($S_{TPB,ca}$)	1.8×10^6	m^2•m^{-3}
Symmetry factor β	0.5	
Fuel channel radius, wall thickness	6.5×10^{-3}, 1.0×10^{-3}	m
Outlet fuel channel radius	1.3×10^{-2}	m
Inlet fuel velocity	0.05	m•s^{-1}
Surface diffusion coefficient of CO on Ni surface (D_{CO})	$2.85\times10^{-5}\cdot\exp(-19307[K]/T)$	m^2•s^{-1}
Surface diffusion coefficient of CO$_2$ on Ni surface (D_{CO_2})	$1.20\times10^{-9}\cdot\exp(-3472[K]/T)$	m^2•s^{-1}
Surface diffusion coefficient of C on Ni surface (D_C)	$3.5\times10^{-9}\cdot\exp(-3472[K]/T)$	m^2•s^{-1}
Surface diffusion coefficient of O on Ni surface (D_O)	$6.3\times10^{-7}\cdot\exp(-7373[K]/T)$	m^2•s^{-1}
Electrolyte		
Thickness (H), radius (r)	2.0×10^{-5}, 1.3×10^{-2}	m
YSZ ionic conductivity (σ_{YSZ})	$3.34\times10^4\cdot\exp(-10300[K]/T)$	s•m^{-1}
Anode		
Thickness (H), radius (r)	1.5×10^{-5}, 6.5×10^{-3}	m

Porosity (ε)			0.35			
Tortuosity(τ)			1.5			
LSM electronic conductivity(σ_{LSM})			4.2×10^7[S·K/m]/T·exp(-1150[K]/T)			s•m^{-1}
Symmetry factor α			0.25			
γ in the exchange current density			1.06×10^{-9}			Ω^{-1}•m^{-2}
Inlet air channel radius			6.5×10^{-3}			m

The boundary conditions of the governing equations for charge transfer and mass transfer are listed in Table 4-4. These boundary conditions are the same as those reported in the references [57, 183]. Details regarding the mathematical descriptions for each of these boundary conditions can be found elsewhere [182].

Table 4-4. Boundary conditions

	Air channel	Channel /Anode	Anode /Electrolyte	Cathode /Electrolyte	Channel /Cathode	Fuel channel
Ionic charge	N/A	Insulation	Continuity	Continuity	Insulation	N/A
Electronic charge	N/A	Specified voltage	Insulation	Insulation	Electric ground	N/A
Mass	O_2/N_2 mass	Continuity	No flux	No flux	Continuity	CO_2/CO mass
Momentum	Flow rate, Pressure	Continuity	Wall (no-slip)	Wall (no-slip)	Continuity	Flow rate, Pressure

4.3. Computational Model

The model described above was implemented in the finite element commercial software COMSOL MULTIPHYSICS®. The button cell performance was calculated at a given cell voltage V_{cell}. The average current density at a given cell voltage was calculated from the total volumetric current densities. A complete polarization curve was generated by setting different cell voltages and running model calculations at each voltage. The physics-controlled mesh was employed in the 2D domain with triangular mesh elements and "Extra fine" element size. The estimated relative error

73

in Newton iterations is set by the specified tolerance of 10^{-3}. The simulations were conducted using multifrontal massively parallel sparse (MUMPS) direct solver. The compressible Brinkman equation and Darcy's law were used for the momentum conservation in the fuel/gas supply channels and porous electrodes [185]. Extended Fick's model (EFM) was used to describe the diffusion of gas species in the porous electrodes as well as fuel/gas supply channels. Charge balances were formulated using generic Ohm's law.

4.4. Results and Discussion

4.4.1. Model Validation

In the present model, three parameters were adjusted to reproduce an acceptable polarization curve obtained experimentally under a CO/CO_2 ratio of 1/2 and at 700°C [58]. More precisely, the fitting was performed by matching the current density at a selected voltage of 1.25 V which lies in the middle of the voltage range considered in [58]. The three fitted parameters are the sticking coefficients for CO_2 and CO adsorption and the pre-exponential factor of k5. The two sticking coefficients were originally taken from [232], i.e. 1×10^{-5} for CO_2 and 5×10^{-1} for CO, which were determined from fitting experimental data. The sticking coefficient is a function of surface coverage, which becomes smaller with a higher surface coverage [235]. Due to the dependence on surface coverage, the values of sticking coefficients can be manually adjusted through trial-and-error simulations. The resulting values were found to be 1×10^{-4} for CO_2 and 4×10^{-2} for CO (Table 4-1). The changes from the initial values (×10 for CO_2 and ×0.08 for CO) are consistent with the resulting calculated low surface coverage of CO_2 and high surface coverage of CO. It was found that the model's convergence is sensitive to the value of the pre-exponential factor of k5, which was also adjusted through simulations. The calculated pre-exponential factor of k5 from DFT is

3.569×10^{22} cm^2/mol/s, which was reduced by an order of magnitude using manual tuning to obtain acceptable results that are comparable with experimental observations. A comparison between the experimentally observed [58] and simulated polarization curves using the three reaction mechanisms at 700 °C with a CO/CO$_2$ molar ratio of 1/2 is shown in Figure 4-3. The cathode supported SOEC operating parameters used in this study were taken from [58]. The kinetic and system parameters were fixed and used to predict the current density at various applied voltages using three reaction mechanisms.
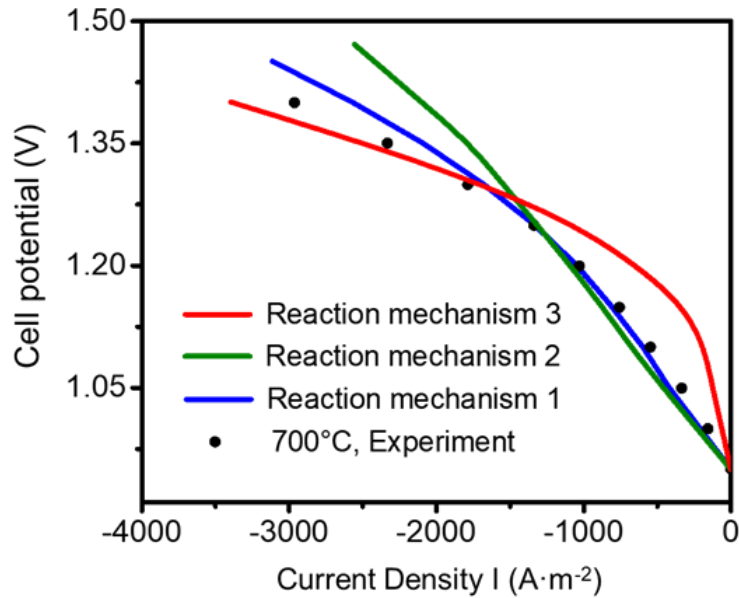
Figure 4-3. Comparison of the experimentally observed [58] and simulated polarization curves using three reaction mechanisms (as shown in Figure 4-2) at 700 °C with a CO/CO$_2$ molar ratio of 1/2.

It can be observed that the simulated polarization curve using reaction mechanism 1, i.e. two-electron charge transfer for $CO_2(s) + Ni(s) + 2e^- \leftrightarrow CO(s) + O^{2-}(s)$, fits best the experimental data. This indicates that reaction mechanism 1 is the most likely mechanism to dominate in the actual catalytic process. The deviations observed of the simulated polarization curves with respect to the experimental data using mechanism 2 and mechanism 3 in the high and low cell potential ranges,

respectively, are likely due to the underestimated overpotential effects on the $CO_2(s) + Ni(s) \leftrightarrow CO(s) + O(s)$ reaction in these two mechanisms. This observation also agrees with the conclusion that the two-electron charge transfer for oxygen spillover step (reaction mechanism 3) is highly unlikely to occur according to Chapter 3, as the polarization curve of this reaction mechanism shows the most deviations with experimental data. However, in Chapter 3, only overpotentials up to 0.3 V vs. open circuit voltage (OCV) were considered, because at high potentials, it is reported that mass transfer is always the limiting step for CO_2 electrolysis [94, 224]. In the present multiscale model, by integrating the kinetic behavior and multiple gas transport processes, it was possible to predict the polarization curve for a wider overpotential window and compare with experimental data to infer the mechanism that agrees the best with experimental observations.

Further model validation was conducted by comparing the polarization curve using reaction mechanism 1 with experimental data at different operating conditions. The kinetic and system parameters were fixed and used to predict the current density at various applied voltages, CO/CO_2 ratios and temperatures. Figure 4-4 shows the comparison between the experimentally observed [58] and simulated polarization curves using reaction mechanism 1 at (a) different temperature (650/700/750°C) with CO/CO_2 molar ratio of 1 and (b) with various CO/CO_2 molar ratios (2, 1 and 0.5) at 700°C. As shown in Figure 4-4, in all cases the model predictions agree well with the experimental observations. From Figure 4-4, one could see that increasing the temperature and the ratio of CO_2 in the inlet gas can both increase the current density and thus enhance the performance of direct CO_2 electrolysis in SOEC.
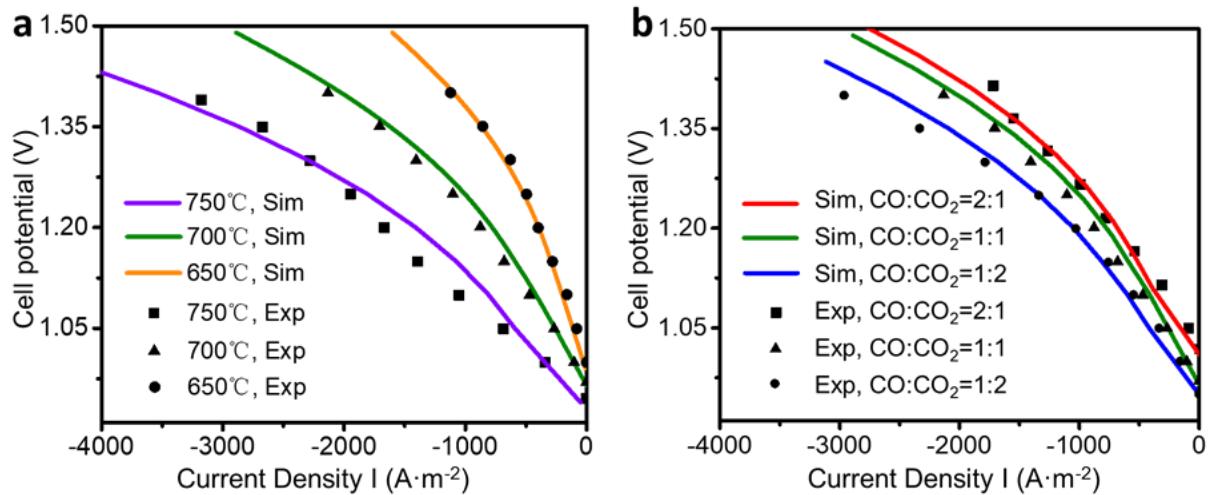
Figure 4-4. Comparison between experimental data [58] and simulated polarization curves using reaction mechanism 1 at (a) different temperature (650/700/750°C) with CO/CO_2 molar ratio of 1 and (b) with different CO/CO_2 molar ratios (2, 1 and 0.5) at 700°C.

4.4.2. Distribution of Current Density

In Figure 4-5, the electronic and ionic current density distributions are examined along the axis-symmetric line (r=0) from cathode to anode at overpotentials of 0.3V, 0.4V and 0.5V, respectively, under a CO/CO_2 ratio of 1/2 and at 700°C. As shown in Figure 4-5, the results show that the current density increases as the overpotential increases (applied cell voltage increases since the OCV is constant due to the temperature and ratio of CO/CO_2 are all the same for these cases).

In Figure 4-5, both the electronic and ionic current densities remain nearly constant throughout the cathode support layer up to around 425 μm from the cathode/fuel channel interface, then they change rapidly within 75 μm of the cathode near the electrolyte. This result indicates that the electrochemical reaction takes place mainly within about 75 μm of the cathode. This observation is consistent with the conclusion that the depth of the electrochemical reaction zone is about 60-100 μm as per previous simulation studies [184, 189, 236] and experimental study of Ni-YSZ anode supported SOFC [237].
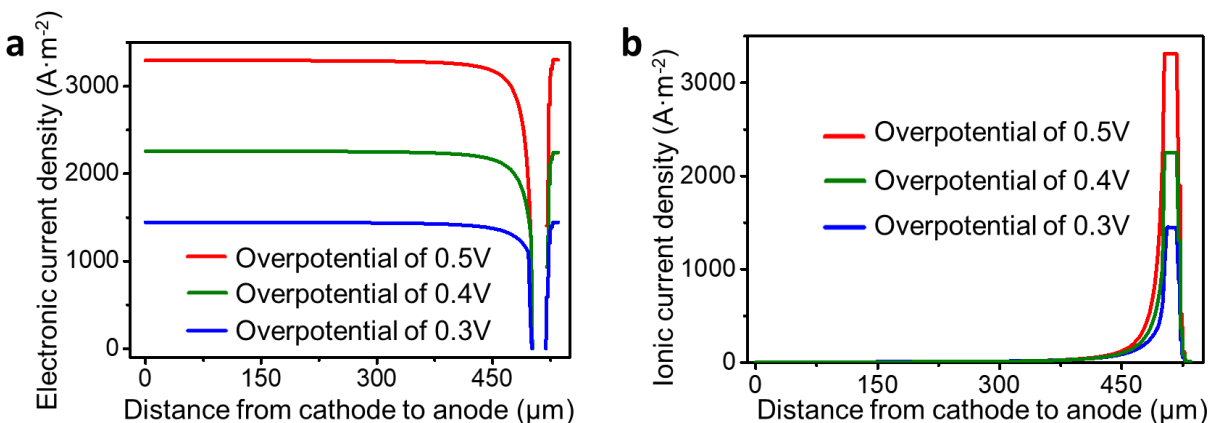
Figure 4-5. Distribution of (a) local electronic and (b) ionic current density along the cell axis-symmetric line (r=0) from cathode to anode at overpotentials of 0.3V, 0.4V and 0.5V, respectively, at a CO/CO_2 ratio of 1/2, and at 700°C for LSM/YSZ/Ni-SDC sandwiched button cell.

4.4.3. Sensitivity Analysis of Elementary Steps

To determine which elementary step has the most impact on the current density, the percentage change of current density under an overpotential of 0.4V and a CO/CO_2 ratio of 1/2 at 700°C was examined when the rate constants (pre-exponential factors) of every elementary reactions were changed by +/-10%. Note that sensitivity analysis at overpotentials of 0.3V and 0.5 V were also carried out and it was found that there was not much difference with that at 0.4V.

As shown in Figure 4-6, r3 and r4 (in Table 4-1), i.e. CO adsorption and desorption step, have more significant effects on the current density than the other elementary steps in this model. Increasing the rate constant of CO desorption and decreasing the rate constant of CO adsorption is expected to increase the current density. This observation is consistent with the DFT based micro-kinetic study results which indicated that CO desorption is the rate controlling step at overpotentials above 0.15 V for the case of reaction mechanism 1 (CO_2 reduction step as the charge transfer step) [52].
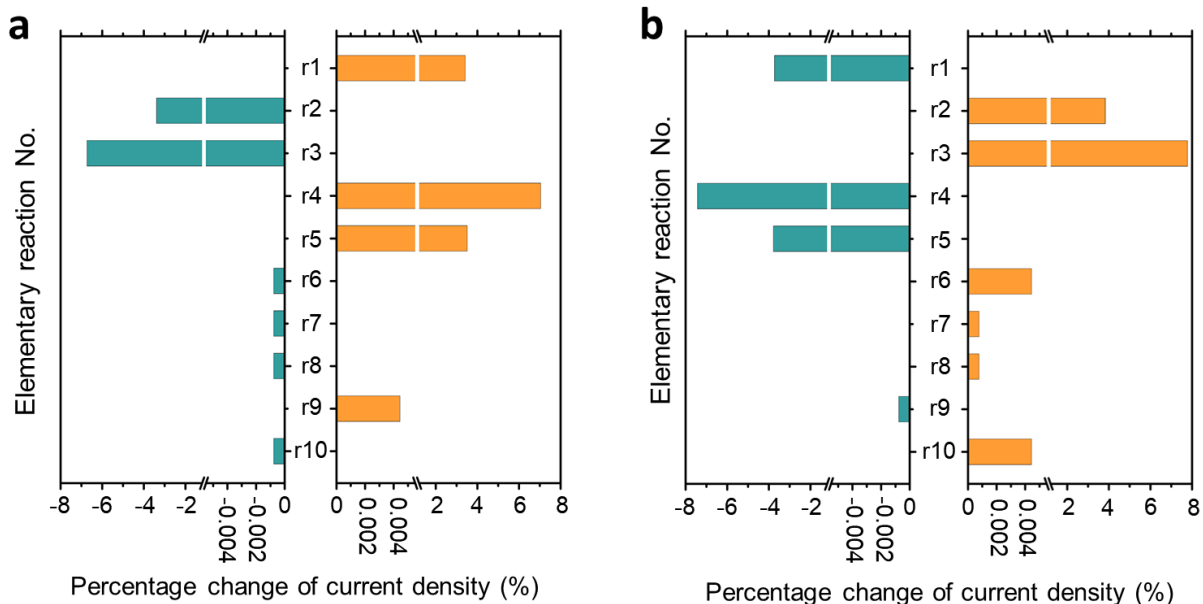
Figure 4-6. Percentage change of current density at an overpotential of 0.4V, a CO/CO_2 ratio of 1/2 and at 700°C when the rate constants of every elementary reactions (a) increase by 10% and (b) decrease by 10%.

The CO_2 adsorption (r1) and desorption step (r2), as well as CO_2 electroreduction step (r5) also have a relatively high effect on the current density as depicted in Figure 4-6. Those observations are consistent with those reported in a previous simulation study, i.e. CO surface diffusion and CO_2 adsorption may be co-limiting for CO_2 direct electrolysis in SOEC [188]. The other elementary steps from r6 to r10 have little influence on the current density.

4.4.4. Distribution of Gas and Adsorbed Surface Species

The multiscale model presented in this study adopted a detailed elementary reaction mechanism, which allows to investigate the surface intermediate species distribution. Figure 4-7 shows the spatial distribution of molar fractions of gas species and surface coverage of adsorbate species at an overpotential of 0.5V under the operating condition of a CO/CO_2 ratio of 1/2 and temperature of 700°C. In SOEC, the consumed CO_2 is converted into CO and O^{2-} by electrochemical reduction in the cathode. Oxygen ions are then migrated through the electrolyte and become O_2 in the anode.

Accordingly, as shown in Figure 4-7(a), the molar fraction of CO_2 decreases slowly in the fuel supply channel; however, a more rapid decrease is observed when CO_2 reaches the cathode towards the cathode/electrolyte interface. The molar fraction of O_2 increases more rapidly in the anode area as it approaches the anode/electrolyte interface.

Carbon deposition in the nickel-based cells can accumulate on the catalysts surface and can lead to the deactivation of the catalysts, which must be considered during CO_2 electrolysis [193, 238]. Figure 4-7 (b), (c) and (d) show the 2D spatial distribution of $CO_2(s)$, $CO(s)$ and $C(s)$ surface coverages in the cathode, respectively. The central area of the cathode in contact with the electrolyte and located below the anode is referred to as the electrochemical reaction zone, whereas the other area of cathode is referred to as the chemical reaction zone. Surface coverage of $CO_2(s)$ is relatively lower, while surface coverage of $CO(s)$ and $C(s)$ are relatively higher in the electrochemical reaction zone compared with those in chemical zone due to faster electroreduction of CO_2.

Due to the highest concentration of gas CO_2 around the interface of electrochemical/chemical zone, as shown in Figure 4-7(a). The corresponding CO_2 surface coverage is also the highest at interface of electrochemical/chemical zone compared with the rest of the cathode area as shown in Figure 4-7(b). Another observation from Figure 4-7 is that the surface coverage of $CO(s)$ shows an opposite trend compared with that of $CO_2(s)$ and $C(s)$ from the interface of electrochemical/-chemical zone to the edge of chemical zone.

From this figure, one can observe that the surface sites are almost fully covered by adsorbed CO molecules (i.e. more than 99%). Moreover, $CO(s)$ has higher surface coverage and distributes uniformly in the electrochemical zone, where $CO(s)$ dissociation leads to higher coverage of $C(s)$. The surface coverage of $C(s)$ was observed around 2.35×10^{-4} at the cathode at an overpotential of 0.5V under the operating condition of a CO/CO_2 ratio of 1/2 and temperature of 700°C, which is

comparable with the reported carbon surface coverage of 1.5×10^{-4} at the anode of SOFC with pure CO inlet at 700°C [185].

In this study, the surface coverage of CO(s) is about 0.991 on Ni surface at a CO/CO$_2$ ratio of 1/2 and 700°C. This might be ascribed to the high adsorption energy (174.72 kJ/mol) of CO on Ni calculated by DFT which indicates adsorbate CO is difficult to desorb from the surface. The calculated CO adsorption energy is consistent with that obtained in previous DFT studies (173–200 kJ/mol) for CO adsorption on Ni surface [54, 216, 239]. Other fitting experimental data predicted that CO adsorption energy are within 135.7–167.36 kJ/mol [240-242]. It is also reported that CO(s) dominate on Ni surface with a coverage of 0.66 in a DFT-assisted microkinetic analysis of methane dry reforming on Ni catalyst under the conditions of 973.15 K, 10 bar with the BET area of Ni catalyst of 7.2 m^2/g with the initial volume fractions of CH$_4$ and CO$_2$ being 0.5 and 0.5, respectively [54]. Currently, most of the multiphysics models of SOEC and SOFC used the reported reaction kinetics proposed by Deutschmann et al. [232], in which the adsorption energy of CO is 111.27 kJ/mol. By using this value, the species distribution was studied within the SOEC cathode [58]. The results indicate that (Ni) and CO(Ni) are the major species on the catalysts surface. It is also reported that most sites on the Ni surface are vacant sites, i.e. (Ni) has a surface coverage of > 94% corresponding to a CO(Ni) surface coverage of 4.4% [188]. In order to verify the effect of CO adsorption energy on its surface coverage, we also performed the simulations by changing the CO adsorption energy from 174.72 kJ/mol to 157.25 kJ/mol (decrease by 10%) under the operation conditions of a CO/CO$_2$ ratio of 1/2 and 700°C. The resulting θ_{CO} decreases from 0.991 to 0.989. This indicates that decreasing CO adsorption energy by 10% alone does not have much impact on the surface coverage of CO in the present study.
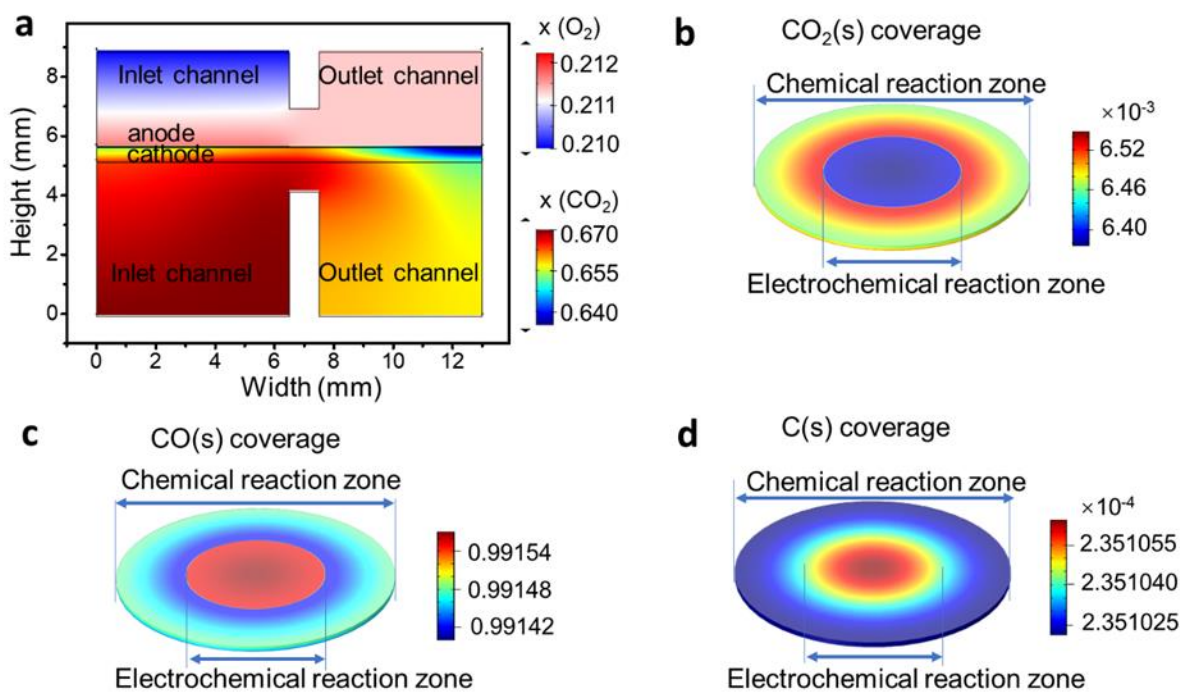
Figure 4-7. Spatial distribution of molar fractions of gas species and surface coverage of adsorbate species at an overpotential of 0.5V, a CO/CO_2 ratio of 1/2 and 700℃. (a) 2D spatial distribution of molar fractions of CO_2 gas (in the cathode and gas channels) and O_2 gas (in the anode and gas channels, respectively). 2D spatial distribution in the cathode near the electrolyte of (b) surface coverages of $CO_2(s)$, (c) surface coverage of $CO(s)$, (d) surface coverage of $C(s)$.

Moreover, another discrepancy between DFT and the empirical reaction kinetics that affects the CO surface coverage is the energy barrier of CO dissociation into C. The energy barrier of this reaction calculated by DFT is 368.64 kJ/mol, which is considerably higher than that in the empirical reaction kinetics (116.12 kJ/mol). This might be because the DFT calculations were only conducted on Ni(111)/SDC surface. According to the literature [216], compared with Ni(211) surfaces, Ni(111) has a much lower activity for C−O bond breaking, and thus, flat surfaces are less susceptible to deactivation by coke. This DFT study literature reported a CO dissociation energy barrier of 290.42 kJ/mol on Ni(111) surface. However, multiple lattice plane exists in an actual Ni catalysis. Therefore, the DFT calculations in this study overestimated the energy barrier of CO dissociation

step. In order to verify the influence of this overestimation, we also performed simulations by using the empirical CO dissociation energy barrier (116.12 kJ/mol) at a CO/CO_2 ratio of 1/2 and 700°C. The results show that θ_{CO} decreases from 0.991 to 0.857. This implies that changing CO dissociation barrier has a noticeable impact on surface coverage of CO.

These results imply that the disparity between DFT and empirical reaction kinetics can make a significant difference in the predicted absolute value of CO surface coverage. Nonetheless, the present multiscale model still provides reasonable predictions of relative surface species distributions. High θ_{CO} further supports the observation that CO desorption is the rate controlling step revealed by the sensitivity analysis depicted in Figure 4-6.

Figure 4-8 shows the surface coverage distribution of adsorbed surface species ((a)CO(s), (b) O^{2-}(s), (c) CO_2(s)) on Ni along the cell axisymmetric line (r=0) within the cathode at overpotentials from 0.1V to 0.5V, at a CO/CO_2 ratio of 1/2 and at 700°C. The results show that the surface coverage of CO(s) (θ_{CO}) increases as the overpotential increases. This is due to the fact that CO(s) is a product of the charge transfer step (CO_2(s) + Ni(s) + 2e$^-$ ↔ CO(s) + O^{2-}(s)) in this study. The increase in overpotential allows for more charge transfer reactions to occur, thus leading to more CO being produced. In addition, the θ_{CO} increases when approaching the cathode/electrolyte interface, because more CO(s) is produced by the electrochemical reaction in this region, which has faster kinetics compared to that of the CO(s) production from the chemical reaction in other regions. This is indicated in the definition of rate constants of the electrochemical reactions (Eqs. 4-1 and 4-2), with the addition of a term involving the overpotential decreases the energy barrier. Likewise, more electrochemical reaction occurring at the cathode/electrolyte interface leads to an increase of O^{2-}(s) and decrease of CO_2(s), as shown in Figure 4-8(b) and (c). Note that, different from surface coverages of CO(s) and O^{2-}(s), the surface coverage of CO_2(s) shows little variation

in chemical reaction zone with the increase of the overpotential but it decreases rapidly in the cathode towards the cathode/electrolyte interface. This is probably because the adsorption of $CO_2(s)$ in the chemical reaction zone can almost compensate its slow consumption, while in the electrochemical reaction zone, with the increase of the overpotential, the local starvation of CO_2 due to the sluggish adsorption of $CO_2(s)$ is insufficient to make up for its rapid consumption. Moreover, the variation of surface coverages of $CO(s)$ and $O^{2-}(s)$ under different overpotentials in the chemical reaction zone might be due to the surface diffusion of these species on Ni from the high concentration zone close to cathode/electrolyte interface. However, the surface diffusion coefficient of CO_2 on Ni surface is smaller compared to that of the other two species; hence, there is not an obvious variation among the surface coverage under different overpotentials.

Figure 4-8(d) shows the surface coverage of $CO(s)$ at overpotentials from 0.1V to 0.5V under different CO/CO_2 inlet ratios. The molar ratio of CO in the inlet gas mixture has a much larger impact on its surface coverage than the overpotential itself. Less inlet CO gas results in lower surface coverage.
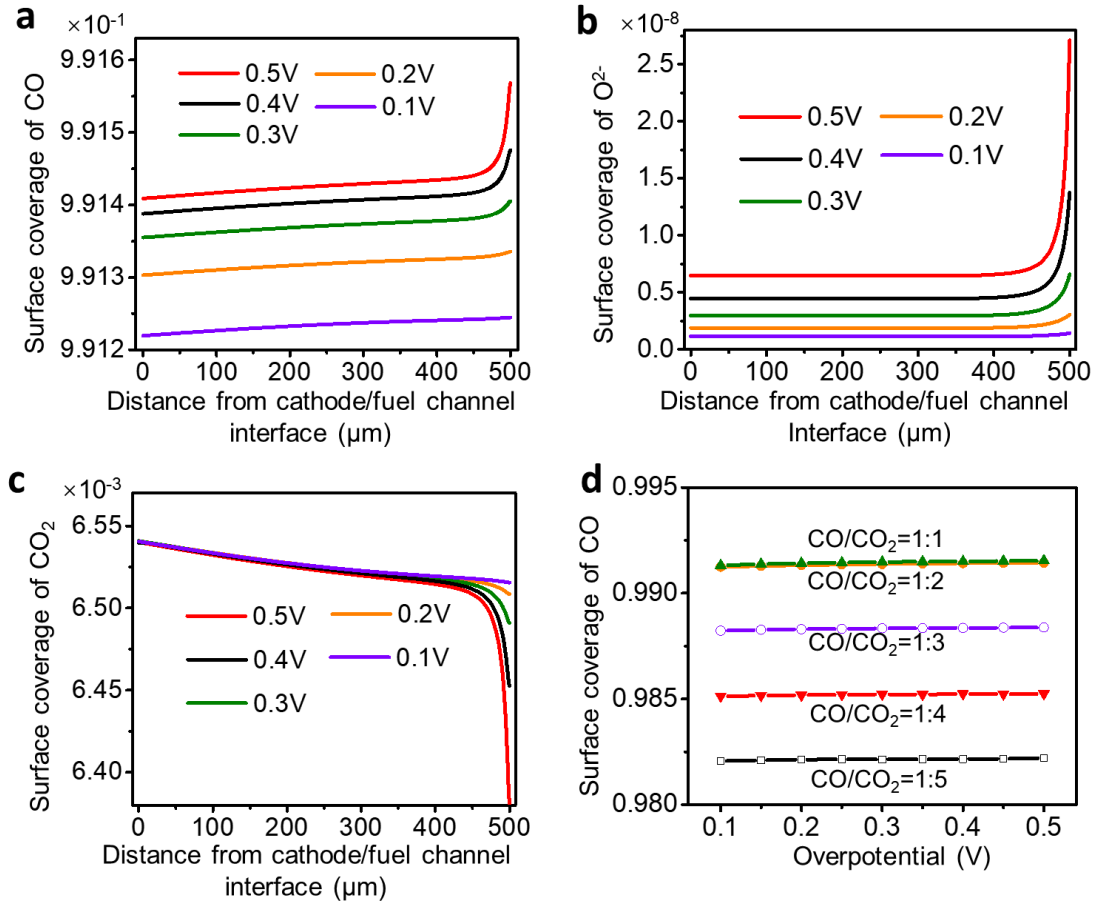
Figure 4-8. The effect of overpotential and CO/CO_2 ratios on the surface coverage distribution of (a) CO(s), (b) O^{2-}(s), (c) CO_2(s) on Ni along the cell axisymmetric line (r=0) within the cathode at overpotentials from 0.1V to 0.5V at a CO/CO_2 ratio of 1/2, and at 700°C. (d) shows the surface coverage of CO(s) at the overpotential from 0.1V to 0.5V under different CO/CO_2 inlet ratios.

4.4.5. CO/CO₂ Ratio and Temperature Effects

As discussed in section 4.4.1, the CO/CO_2 molar ratio in the inlet gas mixtures has a distinct impact on the electrochemical performance for CO_2 electrolysis in SOEC. Herein, numerical simulations using different CO/CO_2 molar ratios were performed to study the influence of this input variable on the simulated polarization curves and the surface coverage of C(s). The results are shown in Figure 4-9.
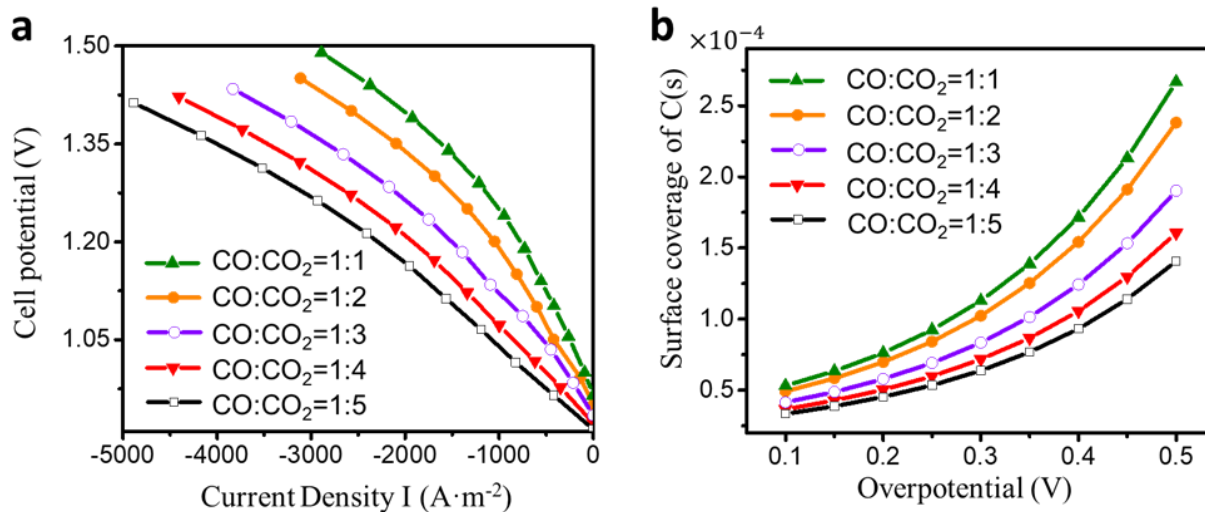
Figure 4-9. (a) Simulated polarization curves (b) Surface coverage of C(s) in the center of cathode surface using reaction mechanism 1 at 700 °C under different overpotentials and various CO/CO_2 molar ratios.

It can be observed that with the increasing proportion of CO_2 in the inlet gas mixtures, the electrochemical performance is improved, which is consistent with experimental results [188, 243]. Currently, SOECs are usually operated with H_2 and/or CO as the safe gas. The state-of-the-art fuel electrode consists of Ni metal as the electronic conductor and YSZ as the oxygen ion conductor [244]. Without the safe gas, Ni particles undergo surface oxidation and agglomeration in a high CO_2-steam atmosphere, thus losing their electrical and catalytic activity, leading to poor redox stability, and eventually degrading the cell performance [60, 243, 245]. For long-term performance, the gas composition of the reactive gas needs to be optimized because of the trade-off between performance and durability.

Moreover, the results show that high cell voltage conditions may cause an increase of the surface coverage of C(s) and the deposition of carbon on the surface of Ni catalyst. This has also been previously reported [183, 188]. At high cell voltages, carbon deposition on the active sites or within the porous electrode would reduce cell performance. In addition, with the increase of CO concentration in the inlet gas, the carbon deposition is also increased. This is reasonable since Ni

catalyst is well known to catalyse dissociation of carbon containing gases or disproportionation of CO (Boudouard reaction) leading to the formation of coke [243]. It was reported that the formation of coke only occurs at very high CO concentrations [246].

As shown in Table 4-5, another parameter that can affect carbon deposition is temperature. When there are large amounts of CO, carbon deposits through the boudouard reaction (CO + CO $\rightarrow$ CO_2 + C) and this worsens as the temperature decreases. At the same ratio of CO/CO_2 (1:1), when temperature decreases from 700°C to 600°C, the carbon surface coverage increases significantly from 2.7×10^{-4} to 8.5×10^{-4}. At 700°C, the carbon deposition keeps decreasing as the ratio of CO/CO_2 decreasing from 9:1 to 1:9. A ratio of CO/CO_2 less than 1:1 may be suitable because the current densities are quite close when increasing CO/CO_2 ratio from 1:1 to 2:1 as shown in Figure 4-4, however, the carbon deposition increased. Therefore, a temperature above 700 °C and an $CO:CO_2$ inlet ratio less than 1:1 are expected to maintain low carbon deposition and high SOEC performance. A higher temperature in SOEC operation can provide better performance, however, it requires higher energy input and higher costs [247, 248].

Table 4-5. The effects of temperature and ratio of CO/CO_2 on the surface coverage of C(s). The values are all calculated at an overpotential of 0.5V.

Temperature (°C)	Ratio of CO/CO_2	Surface coverage of C(s)
600	1:1	8.5×10^{-4}
650	9:1	1.2×10^{-3}
650	5:1	9.0×10^{-4}
650	1:1	6.5×10^{-4}
650	1:2	3.2×10^{-4}
700	1:9	9.1×10^{-5}
700	1:5	1.3×10^{-4}
700	1:4	1.5×10^{-4}

700	1:3	1.8×10^{-4}
700	1:2	2.4×10^{-4}
700	1:1	2.7×10^{-4}
700	2:1	3.0×10^{-4}
700	3:1	3.8×10^{-4}
700	4:1	4.3×10^{-4}
700	5:1	4.7×10^{-4}
700	9:1	6.2×10^{-4}

4.4.6. Polarization Resistance

The polarization resistances in the cathode under different CO/CO_2 ratios at 700°C and overpotential of 0.5V were also calculated as shown in Figure 4-10. The cathodic polarization resistances were calculated using the cathodic overpotential η_{ca} divided by the local current density in the cathode. It can be seen that with the increasing of CO_2 ratio of CO/CO_2 inlet mixture, the polarization resistance in the cathode also increases. In addition, the cathodic polarization resistance increases more rapidly when $CO:CO_2$ ratio changes from 1:5 to 1:9. These observations are consistent with that of experimental electrochemical impedance spectra (EIS) data by using Ni–SDC as the cathode in microtubular cells [60] and Ni–Gadolinium-doped ceria (GDC) as cathode [249]. This trend is due to increased activation polarization caused by reaction kinetics and concentration polarization caused by the gas diffusion.
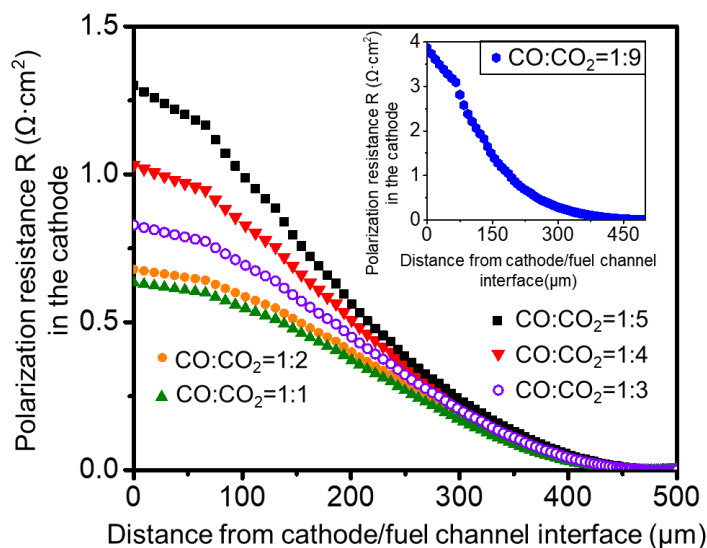
Figure 4-10. Simulated polarization resistance ($\Omega \cdot cm^2$) along the distance from cathode/fuel channel interface (μm) under various CO/CO_2 molar ratios from 1:1 to 1:5 at 700 °C and overpotential of 0.5V. The inset figure is the simulated polarization resistance under CO/CO_2 molar ratios of 1:9.

These data also imply that too high CO_2 concentration in the inlet mixture will cause large polarization resistance. Therefore, a $CO:CO_2$ inlet ratio lager than 1:3 would be recommended to maintain a low resistance because when changing $CO:CO_2$ ratio to 1:4 or 1:5, the resistance will increase rapidly.

Note that the absolute value of simulated polarization resistance in the present study cannot be directly used to compare with experimental EIS data since this model cannot consider the evolution of catalysts, e.g. Ni oxidation, which is also another reason causing the fast-growing polarization resistance in high CO_2 concentration [60].

4.5. Summary

To overcome the limitations of the DFT based microkinetic model and achieve the objective 1 (c) this thesis, i.e. elucidating CO_2 electroreduction mechanism for Ni/SDC, a 2D cathode-supported multiphysics model was built with Ni/SDC as the cathode materials. The kinetic data of surface

reactions and desorption were calculated by DFT while the pre-exponential factors of the CO_2 and CO adsorption along with the pre-exponential factor of CO_2 reduction were fitted to the experimental data. The multi-scale model was validated with reported experimental data. The model developed in this work has provided the following insights:

(1) The most possible reaction mechanism is the one with $CO_2(s)+(s)\ 2e^- \leftrightarrow CO(s)+O(s)^{2-}$ reaction as the charge transfer step.

(2) The electrochemical reduction of CO_2 takes place mainly within about 75 μm distance from the cathode/electrolyte interface.

(3) CO(s) is the dominate species on Ni catalyst surface and CO desorption is the rate-controlling step.

(4) A temperature above 700 °C and an $CO:CO_2$ inlet ratio between 1:1~1:3 are recommended to maintain a low content of carbon deposition, low polarization resistance and high current density.

Chapter 5. CO$_2$ Electrolysis at La(Sr)FeO$_3$-based Cathode

Despite the advantage of conventional Ni-ceramic materials, i.e. high catalytic activity, this cathode material encounters several limitations, such as Ni oxidation, sulfur poisoning, and carbon deposition [250]. Compared with Ni/YSZ or Ni/SDC, perovskite oxides have enhanced coking resistance but lower catalytic activity[31, 97]. Hence, it is highly desirable to develop such catalysts with high catalytic activity capable of efficient conversion of CO$_2$ into CO. In this chapter, CO$_2$ electroreduction mechanism at La(Sr)FeO$_3$-based cathode in SOEC were studied by coupling DFT calculations with a micro-kinetic analysis. In particular, the effects of Ni doping, Mn doping and co-doping of Ni and Mn on CO$_2$ reduction reaction, electronic properties, oxygen vacancy formation and oxygen ion migration are investigated theoretically using DFT analysis. The performance of pure LSF and doped LSF under realistic SOEC operating conditions are evaluated through microkinetic modelling.

5.1. Introduction

La(Sr)FeO$_3$ perovskite oxides (LSF) have been widely investigated as cathode materials for CO$_2$ electrolysis in SOEC because of their mixed ionic and electronic properties and good thermal compatibility with electrolyte YSZ [251]. Oxygen vacancy sites can act as hosts for CO$_2$ chemical adsorption at high temperatures, and in this way CO$_2$ can be activated favoring the electrochemical reduction [17, 30, 52, 94, 195, 252]. Moreover, cation substitution in transition-metal oxides is also an important approach to improve electrocatalysts through the optimization of their composition [37, 253]. LaFeO$_3$ doped with lower valence cations of Sr and Ni in La(A-site metal) and Fe sites

(B-site metal), respectively, can promote the oxygen vacancies formation in order to maintain the system electrically neutral [35, 110, 113]. $La_{0.6}Sr_{0.4}Fe_{0.8}Mn_{0.2}O_{3-\delta}$ has also exhibited remarkable performance towards CO_2 electrolysis using $LaGaO_3$-based electrolyte [36].

While $La(Sr)FeO_3$ based materials have been widely used, the CO_2 reduction mechanisms, particularly the role of the synergetic effects of oxygen non-stoichiometry and Ni/Mn doping, have not been theoretically studied. Developing a microkinetic model based on kinetic data obtained from DFT calculations is critical to predict rates of elementary steps and surface coverage influenced by temperature and voltage [53, 164, 165]. This would construct a bridge between reaction kinetic data and electrochemical measurements [166], e.g. polarization curves [52].

In order to improve the performance of SOEC, it is crucial to gain theoretical insights of CO_2 reduction reaction mechanism, especially through microkinetic modelling by considering the effects of high temperature and electrode overpotentials. This study aims at filling the gap of the absence of reported reaction kinetic mechanism of CO_2 reduction on perovskite. Compared with pure metal systems, the difficulty for modelling perovskite materials in this study is that it involves more possible configurations, including combinations of several oxygen vacancies positions and adsorption positions of species involved in the reaction [164]. Based on the screening of all these possible combinations, a comprehensive DFT+U study of CO_2 electrolysis on $La(Sr)FeO_3$ based materials was performed to investigate the synergistic effects of surface oxygen vacancies, doping elements (Ni, Mn and Ni-Mn co-doping) and surface cation doping ratio. In addition, a microkinetic modelling was first developed based on DFT+U results under realistic SOEC operation conditions, which can determine the rate-controlling step and polarization curves to compare with reported experimental results.

5.2. Models and Methods

5.2.1. Surface Models

The model of $LaFeO_3$ was built with a cubic structure in space group $Pm\bar{3}m$ and lattice parameter 3.926 Å, which is similar to that previously reported by experimental data [254]. A (001) surface was cleaved with FeO_2-terminated. Studies have shown that the (001) structure is the most stable surface in perovskites oxides [255, 256] and the catalytic activity of these materials involves interaction between the gas molecules with the B-site redox active transition metals [143]. This surface model of (2×2) supercell slab was constructed with 8 atomic layers thick, which captures the well-known cooperative tilting of the FeO_6 octahedra [143, 257]. The G-type antiferromagnetic state of LSF was considered in this study to be consistent with neutron diffraction experiments [254].

In the present model, 50% of La was substituted with Sr ($La_{0.5}Sr_{0.5}FeO_3$) to address the role of Sr doping, which is in close agreement with optimum experiment ratio: $La_{0.6}Sr_{0.4}FeO_3$ [31, 35, 113]. We considered all unique arrangements of La and Sr within the $LaFeO_3$ lattice (Table S5-1 in Supporting Information); the most stable structure with Sr substitution is shown in Figure 5-1.

5.2.2. Computational Details

Structure relaxations, single-point energies, and electronic structures were calculated using DFT+U with periodic boundary conditions as implemented in the Vienna ab initio Simulation Package (VASP 5.4.4) [202]. The projector-augmented wave (PAW) method was used to treat the core electrons. The generalized gradient approximation (GGA) with Perdew−Burke−Ernzerhof (PBE) [206] functionals was used to describe exchange-correlation interactions [205]. Spin-polarized calculations with plane-wave cut off 400 eV was adopted using convergence criteria of 10^{-5} eV and

the Gaussian smearing method (σ=0.1 eV). Hellmann-Feynman force of 0.02 eV/Å was chosen as the convergence criterion for optimization of the atomic structure. A vacuum layer of 15 Å was adopted to prevent the interaction between neighboring slabs. The surface slabs were optimized using a 2 × 2 × 1 Monkhorst−Pack k-mesh for sampling of the Brillouin zone. By increasing the cut off energy to 450 eV and the k-points to 4×4×1, we observed a negligibly change in adsorption energies (<0.01 eV), which indicates that adsorption energy values have asymptotically converged using those parameters. To describe the correlated electrons for the 3d-orbitals of Fe, Ni and Mn, the Hubbard parameter U_{eff} values of 4 eV was used for each element in all calculations [164, 255]. The structures of transition state (TS) for the elementary steps were obtained using the climbing image nudge-elastic band (CI-NEB) method [159]. All the transition states in this study were confirmed with one imaginary frequency. Van der Waals interactions were also considered using the DFT-D2 method of Grimme [258].

The adsorption energy E_{ads} of surface species and the activation barrier E_a and reaction energy ΔE are defined the same as those in Chapter 3 and in the reference [208]:

A detailed description of the microkinetic modeling approach can be found elsewhere [52]. The frequencies of all involved species were calculated and are presented in the supporting information (Table S5-2). For an elementary step involving a charge transfer process, the forward and backward charge transfer reaction rates are formulated the same as those in Chapter 3:

The current density is calculated using the Butler-Volmer Equation [164],

$$i = zer\Gamma \tag{5-1}$$

where i denotes the current density (A·cm^{-2}), r represents the overall reaction rate (s^{-1}) calculated from microkinetic model, z is the number of electrons involved in the overall reaction and Γ is the

number of active sites per surface area (cm^{-2}), which is 1.62×10^{14} cm^{-2} for the (001) FeO_2-terminated surface in our model.
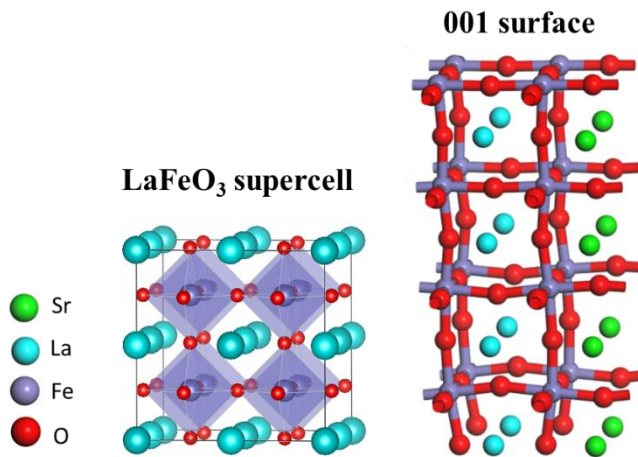
Figure 5-1. $LaFeO_3$ supercell showing FeO_6 octahedra and the optimized most stable $La_{0.5}Sr_{0.5}FeO_3$ (001) surface structure.

5.3. Results and Discussion

5.3.1. Ab Initio Thermodynamic Analysis

Oxygen nonstoichiometry and defective structures of perovskite are expected at low oxygen partial pressure and elevated temperatures ($P_{O_2} < 0.13atm$, T > 473K) [259]. With the aim to determine the most stable LSF structure under SOEC operating conditions, we carried out a thermodynamic analysis of Gibbs free energies based on ab initio calculations on $La_{0.5}Sr_{0.5}FeO_{3-\delta}$ (001) surface model. An approximate phase diagram was constructed for the possibility of 1-5 oxygen vacancies. Hence, a total of 45 structural optimization configurations were performed for the surface models with 1-5 oxygen vacancies at all possible locations. Results from this analysis would be used to find the structure with the lowest free energy at 0 K for each case (1-5 oxygen vacancies). This information is provided in Table S5-3 in the Supporting Information. The most stable structures identified for the possibilities of 1-5 oxygen vacancies at 0 K were then incorporated into the

constrained ab initio atomistic thermodynamics calculations [164], which enabled further identification of relevant structures and compositions under realistic temperatures and pressures. The corresponding phase diagrams were constructed by calculating the change in the free energy (ΔG) for the oxygen vacancy formation process as a function of the oxygen chemical potential, i.e. temperature and oxygen partial pressure.

$$La_8Sr_8Fe_{16}O_{48} \rightarrow La_8Sr_8Fe_{16}O_{48-\alpha} + \frac{\alpha}{2}O_2 \qquad (5\text{-}2)$$
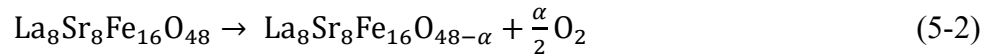
Note that α denotes the number of oxygen vacancies (α =0-5 in this study). The Gibbs free energy change for the formation of α oxygen vacancies can be calculated as follows:

$$\Delta G = E_{\text{defective}} + \alpha[E_O + \Delta\mu_O(T,P)] - E_{\text{perfect}} \qquad (5\text{-}3)$$

where $E_{\text{defective}}$ and E_{perfect} were obtained from DFT+U calculations and represent the free energies of surface models with and without oxygen vacancies, respectively. E_O is the energy of the atomic oxygen, i.e.

$$E_O = \frac{1}{2}(E_{O_2} + \Delta h_{O_2}) \qquad (5\text{-}4)$$

where E_{O_2} denotes the free energy of an oxygen molecule of gas phase in the triplet state by ab initio calculations. Δh_{O_2} is the 1.36 eV correction [260] used to correct the GGA binding energy. $\Delta\mu_O$ describes the temperature- and pressure- dependent chemical potential of O:

$$\Delta\mu_O(T,P) = \frac{1}{2}[\Delta\mu_{O_2}(T,P^0) + k_BT \ln\left(\frac{P}{P^0}\right)] \qquad (5\text{-}5)$$

where $\Delta\mu_{O_2}(T,P^0)$ can be derived from the gas phase thermochemistry data of O_2, i.e. enthalpy and entropy contributions, which are described as polynomial functions of temperature at 1 bar [261]. P^0 is standard pressure(1 atm). Figure 2(a) illustrates the calculated phase diagrams for the $La_{0.5}Sr_{0.5}FeO_{3-\delta}$ (001) surface models with 0-5 oxygen vacancies. Each colored area indicates the

number of oxygen vacancies yielding the lowest Gibbs free energy change for a given temperature and oxygen partial pressure.
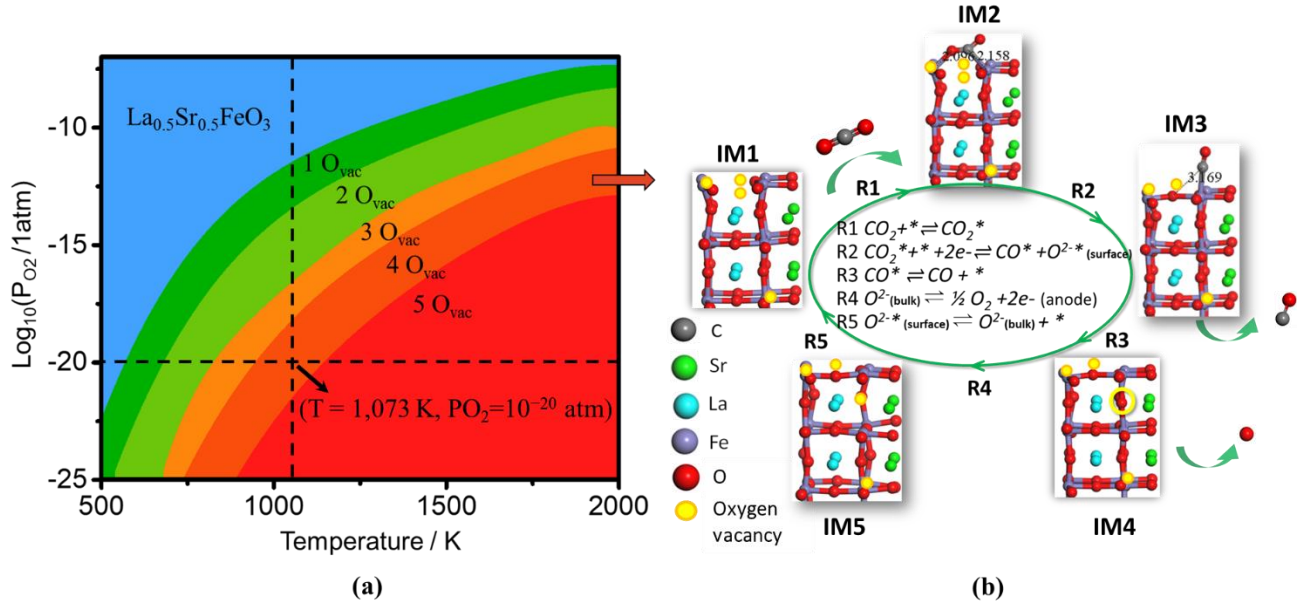
Figure 5-2. (a) Calculated phase diagrams of $La_{0.5}Sr_{0.5}FeO_{3-\delta}$ (001) surfaces. Each colored area indicates the number of oxygen vacancies yielding the lowest Gibbs free energy change for a given temperature and oxygen partial pressure. Dashed lines indicate experimental cathodic SOEC conditions (T = 1,073 K and $PO_2 = 10^{-20}$ atm [37]). (b) The optimized most stable structure with 4 oxygen vacancies is shown as the intermediate 1 (IM1) together with the reaction mechanism of CO_2 electroreduction proposed in this study.

At typical SOEC operating conditions, i.e. T = 1,073 K and $P_{O_2} = 10^{-20}$ atm [37], the surface model that involves 4 oxygen vacancies is the most favorable (oxygen vacancy concentration: 4/48 = 8.3%). According to experimental results [259, 262], the concentration of oxygen vacancy in LSF is approximately 8% at 1,073K and O_2 partial pressure of 10^{-20} atm. These observations indicate that the ab initio thermodynamic analysis is in good agreement with reported experimental results. Note that we tested all meaningful oxygen vacancy positions with the aim to identify all the possible lowest-energy structures for the cases with 1-5 oxygen vacancies. The optimized most stable structure with 4 oxygen vacancies is shown as the intermediate 1 (IM1) in Figure 2(b)

together with the reaction mechanism of CO_2 electroreduction proposed in this study based on literature [52, 164]. IM1 is also the starting point for the detailed investigation of reaction pathways for this process.

5.3.2. CO_2 Reduction Mechanism on $La_{0.5}Sr_{0.5}FeO_{3-\delta}$ (001) Surface

The proposed reaction mechanisms for CO_2 electroreduction on $La_{0.5}Sr_{0.5}FeO_{3-\delta}$ (001) surface is shown in Figure 5-2(b). The overall electrochemical reduction of CO_2 at the LSF cathode can be expressed as follows:

$$CO_{2(g)} + 2e^- + V_O^{..}(LSF) \rightarrow CO_{(g)} + O_O^{2-}(LSF) \tag{5-6}$$
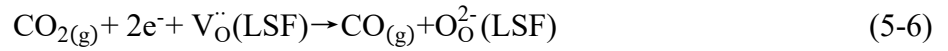
where $V_O^{..}$ denotes a doubled charged oxygen vacancy of LSF that has been formed before CO_2 reduction and O_O^{2-} with two electrons is the surface oxygen ion of LSF.

As shown in Figure 5-2(b), R1-3 represent the CO_2 adsorption, CO_2 reduction and CO desorption steps, respectively. To complete the reaction cycle, the oxygen evolution step (R4) was added to the mechanism under the assumption that oxygen ions are conducted through the electrolyte due to the applied voltage and become oxygen gas at the anode. We have reported the energy barrier for the oxygen migration step in samarium-doped ceria (SDC) electrolyte in our previous study [52]. Therefore, SDC is also adopted to be the electrolyte in this study. At present, SDC or Gadolinium-doped ceria (GDC) are also added into the cathode materials and mixed with LSF uniformly to enhance the ionic conductivity for CO_2 electrolysis in SOEC [31]. In fact, the reaction R4 includes two steps: oxygen migration from cathode SDC bulk to the SDC electrolyte (R4a) and gas oxygen formation (R4b), i.e.
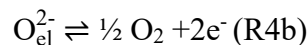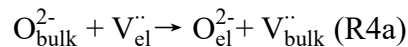
$$O_{bulk}^{2-} + V_{el}^{..} \rightarrow O_{el}^{2-} + V_{bulk}^{..} \tag{R4a}$$

$$O_{el}^{2-} \rightleftharpoons \tfrac{1}{2} O_2 + 2e^- \tag{R4b}$$

where $V_{el}^{\cdot\cdot}$ and $V_{bulk}^{\cdot\cdot}$ represent the oxygen vacancy of electrolyte and SDC bulk, respectively; similarly, O_{el}^{2-} and O_{bulk}^{2-} are the corresponding oxygen ion in electrolyte and SDC bulk, respectively. Note that we neglected the oxygen migration from LSF bulk to the SDC within the cathode, which is a reasonable assumption due to the uniform distribution of these two materials in the cathode [31]. According to previous studies, oxygen evolution reaction at the anode side (R4b) is faster at high temperatures (700-900°C) [164, 166]; therefore, it was assumed that the reaction rate of R4 is the same as that of R4a. The forward energy barrier of R4a (bulk oxygen migration in SDC) is 0.61 eV while the backward energy barrier is 0.92 eV. As shown in Figure 2, the last step is oxygen migration from LSF surface to LSF bulk (R5), i.e.

$$O_{surface}^{2-} + V_{bulk}^{\cdot\cdot} \rightleftharpoons O_{bulk}^{2-} + V_{surface}^{\cdot\cdot} \text{ (R5)}$$
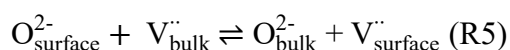
5.3.3. CO₂ Adsorption Energy and Reduction Reaction Energy

5.3.3.1. Pure La₀.₅Sr₀.₅FeO₃₋δ (001) Surface

We have investigated the CO_2 adsorption configurations on a clean LSF (001) surface (IM1 in Figure 5-2(b)) by including up to 11 possible adsorption sites and CO_2 molecule orientations including parallel and inclined configurations with respect to the surface. The configurations of CO_2 and CO adsorption before and after structural optimization considered in this study are presented in the Supporting Information (Figure S5-1 and Figure S5-2). The results show that only 3 chemical adsorption configurations are found to be stable. These stable configurations are shown in Figure 5-3. Configuration 1 and 2 depicted the formation of tridentate; that is, CO_2 bonds with surface oxygen (C-$O_{surface}$ bond) and Fe (O–Fe bond) simultaneously. The $O_{surface}$–C distance and the O–C–O bending with approximately 120° angles indicate a carbonate formation[263]. High temperature CO_2 electrolysis experiments based on operando near-ambient pressure XPS have also

demonstrated the existence of carbonate species on $La_{0.6}Sr_{0.4}FeO_{3-\delta}$ [264]. The basicity of surface O^{2-} ions of perovskite makes it more likely to attract and bind with C of CO_2 (Lewis acid center) thus forming carbonates. Experimentally, the presence of surface defects modifies O basicity: O vacancies accepting electrons from other atoms should enhance the individual O basicity [265, 266], which allows stronger CO_2 adsorption towards carbonate formation. These adsorption modes result in strong interactions between CO_2 and the surface (E_{ads} = -2.28 eV and -1.05 eV for configurations 1 and 2, respectively) so that the CO_2 dissociation reaction energy (endothermic) and energy barrier are much higher (> 3 eV) than that of configuration 3 (1.3 eV): CO_2 adsorption on top of Fe-O vacancy-Fe site, as depicted in Figure 5-3. The adsorption energy of -0.15 eV calculated in this study indicates a moderate chemisorption. More importantly, the reduced CO_2 dissociation reaction energy (1.30 eV) and energy barrier (1.82 eV) ascribed to the weaker adsorption of energy make this chemisorption configuration to qualify as the most favorable for CO_2 reduction reaction (i.e. configuration 3).
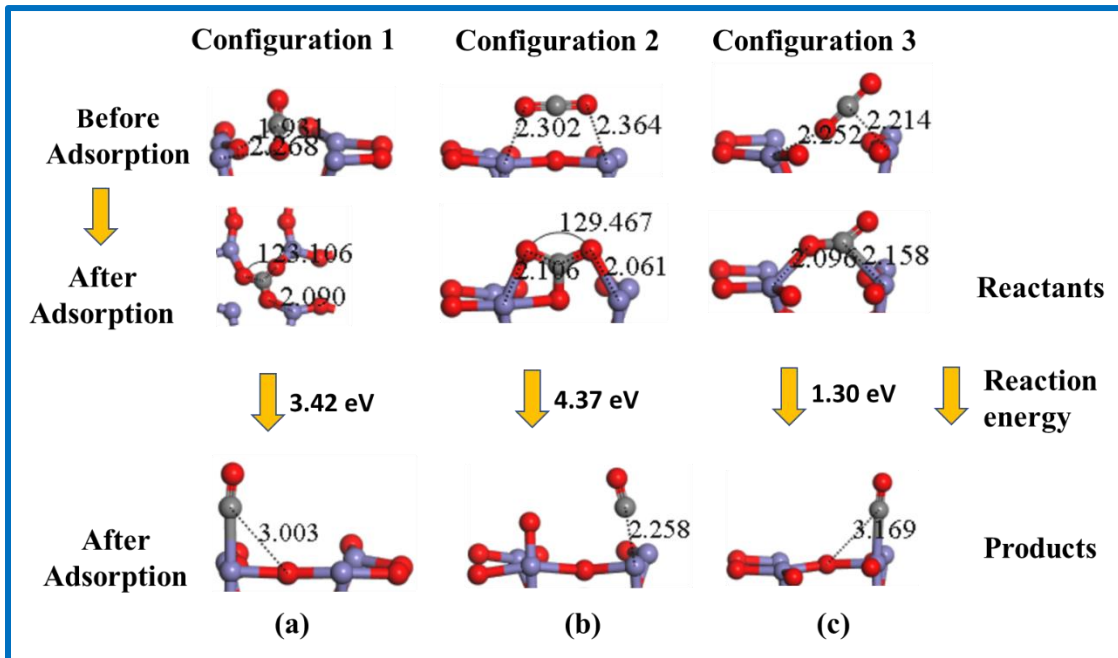
Figure 5-3. (a), (b) and (c) are the three CO_2 chemisorption configurations before and after adsorption and

their corresponding optimized structures of dissociation products CO+O.

5.3.3.2. Ni and Mn Doping

A DFT+U study describing the doping effects of LSF on CO_2 adsorption energy and reduction reaction energy were completed on the most stable LSF (001) surface model with 4 oxygen vacancies ($La_{0.5}Sr_{0.5}FeO_{2.75}$). The main models after structural optimization investigated in this study are depicted in Figure 5-4. This Figure shows the 12 models that were built involving Ni/Mn doping and Ni-Mn-co doping. Surface oxygen vacancy effects can be obtained by comparing the models with 2 or 3 surface oxygen vacancies. We can also gain insight on the surface cation doping ratio effect by comparing the models with the substitution of 25% or 50% of surface Fe atoms. These models were also used for further screening and the selected models with the lowest CO_2 reduction reaction energy would be incorporated in the following DFT analysis and micro-kinetic modelling.
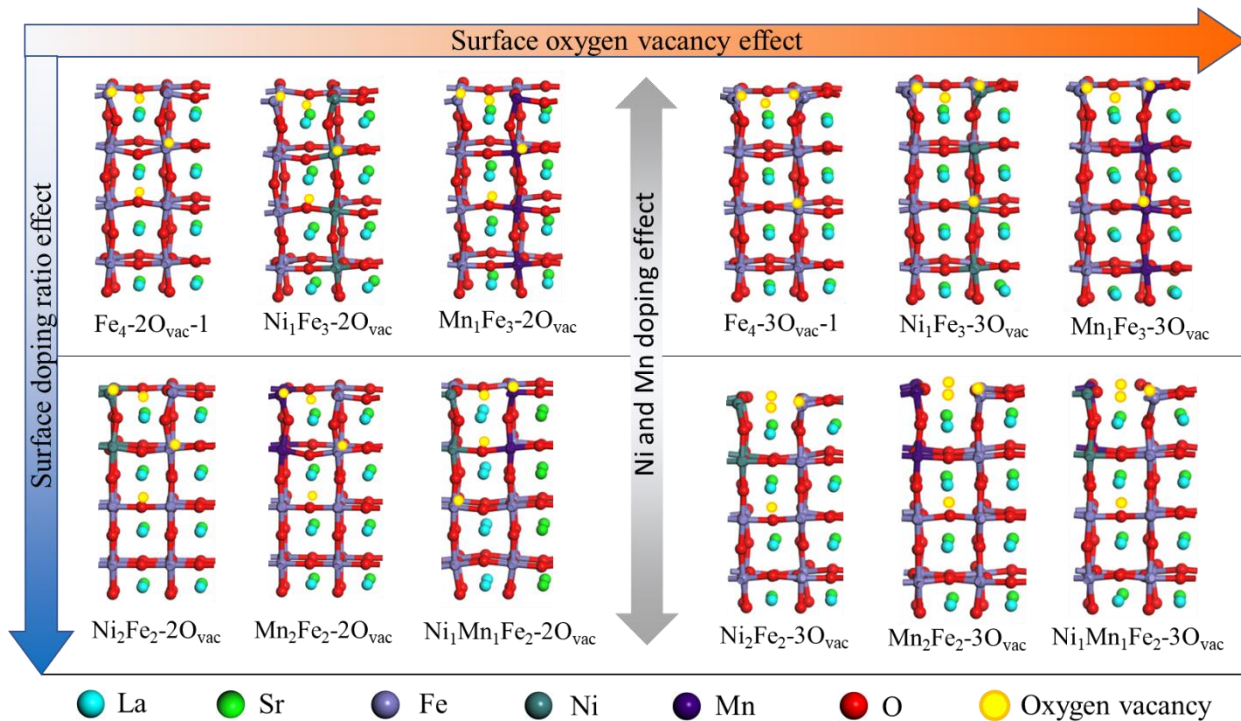
Figure 5-4. Models investigated in this study. The notations indicate the surface compositions: e.g. Ni_1Fe_3-

2Ovac represents the model with 1 Ni cation, 3 Fe cation and 2 oxygen vacancies on the surface.

In order to be comparable with the most stable pure LSF model, all the models with doping include 4 oxygen vacancies. Moreover, the locations of all oxygen vacancies for the models with doping are the same as those of the pure LSF model. The total doping ratio is 25% (4 out of 16 Fe cations, $La_{0.5}Sr_{0.5}Fe_{0.75}Ni_{0.25}O_{2.75}$) for each model, which is close to the reported optimal Fe/Ni and Fe/Mn ratios [31, 113]. After performing calculations with different locations of 4 doping cations (Ni/Mn), it was found that the two most stable LSF slab models with doping were those that corresponded to the models with 1 and 2 doping cations on surface, namely, 25% and 50% surface cations doping ratio respectively; this is presented in Table S5-4 in the Supporting Information. For Ni/Mn co-doping model in this study, Ni and Mn surface doping ratios are all 25% with one Ni cation and one Mn cation exposed on the surface in order to investigate synergistic effects of Ni and Mn on CO_2 reduction reaction.

To simplify the analysis, only two representative CO_2 adsorption configurations, including configuration 1 (most stable) and configuration 3 (most favorable for dissociation), were considered on all models, as shown in Figure 5-4. Moreover, the co-adsorption of the corresponding reduction products of CO and O were also studied. The dissociation reaction energy of each CO_2 chemical adsorption configuration was calculated for every model tested. The lowest reaction energy and its corresponding CO_2 adsorption energy on each model are summarized in Figure 5-5(a). The corresponding data used to construct this figure can be found in Table S5-5 in Supporting Information. The configurations for the adsorption of initial state (IS) and final state (FS) in the CO_2 reduction reaction of SOEC are presented in Figure 5-5(b). Note that for pure LSF models, we also considered the models with no oxygen vacancy (Ovac) and 1 Ovac for comparison purposes (see Table S5-5).

Fe_4-2Ovac-1 is the model with two surface oxygen vacancies located at two adjacent Fe-O-Fe sides while Fe_4-2Ovac-2 has two surface Ovac in the opposite sides. The former allows the existence of the most favorable CO_2 adsorption configuration for its dissociation; therefore, the reaction energy is lower than that of the latter. For pure LSF, the reaction energy reduces with the increase of surface oxygen vacancies except when CO_2 is adsorbed by binding with surface oxygen (the carbonate formation). Fe_4-3Ovac-1 and Fe_4-3Ovac-2 correspond to the models with CO_2 adsorption configuration 3 and 1 in Figure 5-3, respectively.

Two adjacent surface oxygen vacancies were also tested for all the models with doping. For the models with 2 surface oxygen vacancies and 25% surface cation doping, the reaction energies are as follows: $Ni_1Mn_1Fe_2$-2Ovac< Mn_1Fe_3-2Ovac< Fe_4-3Ovac-1<Ni_1Fe_3-2Ovac< Fe_4-2Ovac-1. Note that all these models are compared based on the same CO_2 adsorption configuration.

Therefore, Ni-Mn co-doping can notably boost CO_2 reduction reaction thermodynamically. With 50% surface cation doping, when we locate CO_2 in the same adsorption site with CO_2 adsorption configuration 3, it can only be repelled thus forming physical adsorption. This is possibly because doping more Ni or Mn elements on the surface increases the distance between the two surface metal cations connected with the oxygen vacancy as displayed in Table S5-6 in Supporting Information. Hence, CO_2 cannot chemically bond with those two metal cations with C and O atoms simultaneously. In summary, 25% surface cation doping is better than 50% in terms of CO_2 reduction reaction energy.
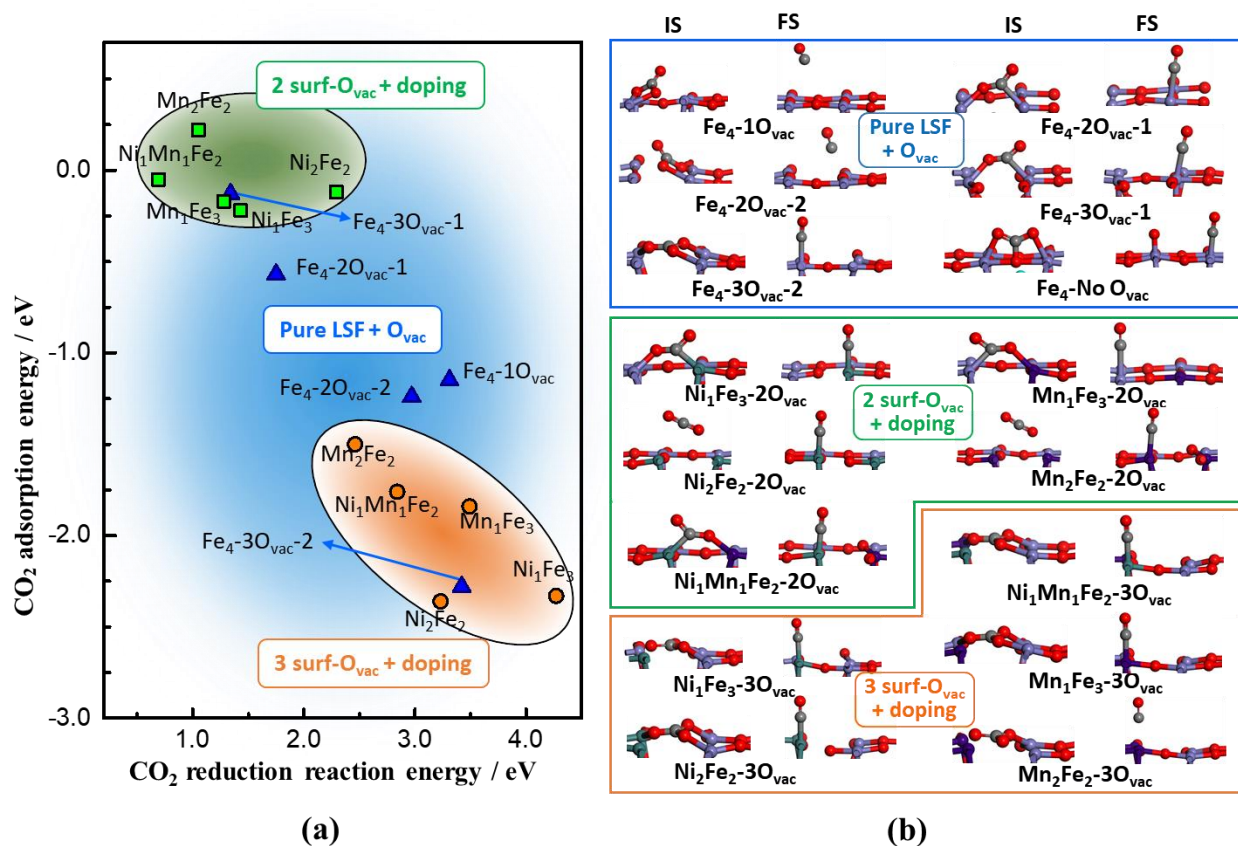
Figure 5-5. (a) CO_2 adsorption energy and reduction reaction energy summary for all the models investigated in this study. (b) The adsorption configurations of CO_2 (initial state (IS)) and its corresponding reduction products CO+O (Final state (FS)) on all the models. The notations indicate the surface compositions: e.g. Ni_1Fe_3-$2O_{vac}$ represents the model with 1 Ni cation, 3 Fe cation and 2 oxygen vacancies on the surface.

In contrast, for the models with 3 surface oxygen vacancies, all the models with doping can only form extremely strong CO_2 adsorption, which is the same observed for configuration 1 (i.e. carbonate formation), as shown in Figure 5-3. Contributing to the formation of the most favorable CO_2 adsorption configuration for dissociation, the CO_2 reduction reaction energy for the doping models with 2 surface oxygen vacancies are always lower than that of models with 3 oxygen vacancies. Therefore, models with 2 surface Ovac are better than 3 for the models with doping in terms of favoring CO_2 reduction reaction. Nevertheless, the same conclusion can be drawn for the 3 surface Ovac with the case of 2 surface Ovac, i.e. Mn doping model exhibits lower reaction

energy towards CO_2 electrolysis than that of Ni doping model.

5.3.4. CO_2 Reduction Kinetics and Oxygen Vacancy Formation & Migration

Four models of pure LSF, Ni doping, Mn doping and Ni-Mn co-doping featuring the lowest CO_2 reduction reaction energies were employed to do further investigation relevant to the proposed CO_2 reduction mechanism, i.e. Fe_4-3Ovac-1, Ni_1Fe_3-2Ovac, Mn_1Fe_3-2Ovac and $Ni_1Mn_1Fe_2$-2Ovac.

As shown in Table 5-1, taking the kinetic barriers of CO_2 electrolysis into consideration, we find that they follow the same trend as with the thermodynamic free energy change except for Ni-Mn co-doping which exhibits remarkably low reaction energy while the energy barrier is slightly higher than that of Mn doping. As shown in Table S5-7 and Table S5-8 in the supporting information, we can conclude that Mn prefers to bind with O of CO_2 while Ni is more likely to bind with C of CO_2 during CO_2 adsorption process. Among the selected four models, Ni-Mn co-doping allows for its stronger interactions with the products CO (binding with Ni through C atom) and O (binding with Mn) simultaneously, which lowers the free energy of the products (final state) of the CO_2 electrolysis process. Meanwhile, the energy of CO_2 adsorption configuration is higher (initial state) ascribed to the weaker adsorption; this is more likely due to the counterbalance of CO_2 binding with Ni (through C atom) and Mn cations (through O atom) on surface. This explains the saliently low reaction energy of CO_2 reduction ($\Delta E=E(FS)-E(IS)$) triggered by Ni-Mn co-doping.

Table 5-1. Energetic data calculated by DFT for the selected models of pure LSF, Ni doping, Mn doping and Ni-Mn co-doping.

Reactions	E_a/eV for surface reactions (forward / backward); E_{ads}/eV for surface adsorption			
	Fe_4-3O$_{vac}$-1	Ni_1Fe_3-2O$_{vac}$	Mn_1Fe_3-2O$_{vac}$	$Ni_1Mn_1Fe_2$-2O$_{vac}$

CO_2 adsorption (R1)	-0.15	-0.22	-0.17	-0.05
CO_2 reduction reaction (R2)	1.82 / 0.52	1.87 / 0.44	1.57 / 0.29	1.73 / 1.04
CO adsorption (R3)	-0.65	-0.55	-0.37	-0.76
O^{2-} migration from the surface to the bulk (R5)	0.63 / 0.91	0.71 / 1.01	0.43 / 0.72	0.69 / 1.18
Surface oxygen vacancy formation energy /eV	0.73	0.02	1.18	0.10
Bulk oxygen vacancy formation energy /eV	1.66	0.32	1.47	0.30

Mn doping leads to the lowest energy barrier of CO_2 electrolysis owing to its most preferable binding of O likewise which can be further illustrated by the effective Bader charge analysis in Table 5-2. The electrons (formal charges) obtained by the surface O bonded with metal cations followed the same trend with the surface oxygen formation energy (Evac): Mn doping > Pure LSF > Ni-Mn co-doping > Ni doping. The vacancy formation energy has been evaluated as follows [52]:

$$E(vac.) = E(model + vac.) + E(O) - E(model) \qquad (5\text{-}7)$$

where E(model) and E(model + vac.) are the total energies of the models before and after the vacancy formation, respectively; E(O) is the half energy of an oxygen molecule in the triplet state.

The effective Bader charges calculated in this study are analogous to that of $LaMO_3$ (M = Mn, Fe, Co, Ni) [267]. These trends in oxygen vacancy formation energy agree with other DFT+U studies on the redox energetics of late transition metal oxides [255, 260, 268]. For instance, the oxygen vacancy formation energy of $La_{7/8}Sr_{1/8}MnO_3$ reported by Piskunov et al. [269] is lower than the that of $LaMnO_3$, which could easily be due to oxidation of Mn^{3+} by Sr doping and Sr-oxygen vacancy interaction (around 1eV) [255]. Therefore, considering the Sr doping, the surface oxygen

vacancy formation for $La_{0.5}Sr_{0.5}Fe_{0.75}Mn_{0.25}O_{2.75}$ calculated in this study (1.18 eV) is close to 1.2 eV, which is the same to that reported Evac of $LaMnO_3$ (001) surface (2.2 eV) [255] minus 1 eV.

Table 5-2. Calculated Bader Charges (e) of surface (O, Fe, Ni, Mn) and subsurface atoms (Sr and La) for the selected models of pure LSF, Ni doping, Mn doping and Ni-Mn co-doping.

Atoms	Bader charges (in e)			
	Fe_4-$2O_{vac}$-1	Ni_1Fe_3-$2O_{vac}$	Mn_1Fe_3-$2O_{vac}$	$Ni_1Mn_1Fe_2$-$2O_{vac}$
O	-1.109	-1.062	-1.149	-1.095
Fe	+1.192	+1.181	+1.155	----
Ni	----	+1.123	----	+1.129
Mn	----	----	+1.488	+1.342
Sr	+1.572	+1.578	+1.567	+1.584
La	+2.073	+2.065	+2.080	+2.072

O: surface oxygen bonded with Ni, Mn and Fe; Fe: the cation connecting to 2 surface oxygen vacancy.

As expected, the most electron charge transfer between Mn and O is an indication of higher O affinity of Mn compared to other doping situations. However, this also leads to higher O vacancy formation energies for Mn doping, which implies that there will be fewer oxygen vacancies on the surface. Note that the models with Mn, Ni, and Ni-Mn co-doping considered in this study are all with 2 surface oxygen vacancies on surface. Our calculations on bulk oxygen vacancy formation energies for these models are also in qualitative agreement with previous DFT studies [255]: $LaMnO_3$ and $LaFeO_3$ have high bulk E_{vac}, of which the surface vacancy concentration will be orders of magnitude higher than in the bulk, impacting the surface vs bulk oxygen transport. Whereas $LaNiO_3$ has quite low bulk E_{vac}, although their surface vacancy concentrations are also

expected to be higher than in their bulk.

Based on the above, the generally higher O vacancy formation energy suggests that Mn doping alone could be catalytically less active for CO_2 reduction reaction in SOEC. Ni-Mn co-doping model demonstrates slightly higher energy barrier than that of Mn doping model but significantly reduced oxygen formation energy. On the basis of our current analysis, we expect that the addition of Ni to the Mn doped LSF surface could facilitate surface oxygen vacancy formation, which in turn improves the electrochemical performance towards CO_2 reduction. Shishkin and Ziegler found that for Ni adsorption on ceria, Ni donates some electrons to the surface [150] (here mostly to the Fe atoms). When Ni is added to this $Sr_2Fe_{1.5}Mo_{0.5}O_6$ (001) surface [164], upon removing the additional oxygen atom, most of the extra charge is transferred back to Ni, and the Fe atoms are not significantly further reduced. Thus, Ni promotes oxygen vacancy formation by accepting the extra electrons left by the removed oxygen atom, resulting in its lowest valence state (formal charge) among all the cations. Based on these observations, we can reasonably expect that Ni-Mn doping would be the best choice to achieve low oxygen formation energy, energy barrier and reaction energy of CO_2 reduction from a theoretical (DFT) point of view. To date, experimental studies involving this co-doping material have not been reported in the literature.

5.3.5. Insights from Microkinetic Modeling

In order to better understand the performance of LSF cathode materials under realistic SOEC operation conditions (with and without doping), a micro-kinetic modelling was developed based on the DFT calculations. The energetic data considered in the micro-kinetic modelling is summarized in Table 5-1. Figure 5-6(a) depicts the energy profile of the proposed CO_2 reduction mechanism from R1 to R5 for the four selected models: Fe_4-3Ovac-1, Ni_1Fe_3-2Ovac, Mn_1Fe_3-2Ovac and $Ni_1Mn_1Fe_2$-2Ovac. All energies are reported using the energies of the initial state of the

bare surface model with gas CO_2 (IM1) as a reference. The insets in Figure 5-6(a) provide the optimized structures of the transition states of R1 and R5 for the four models investigated in this study.
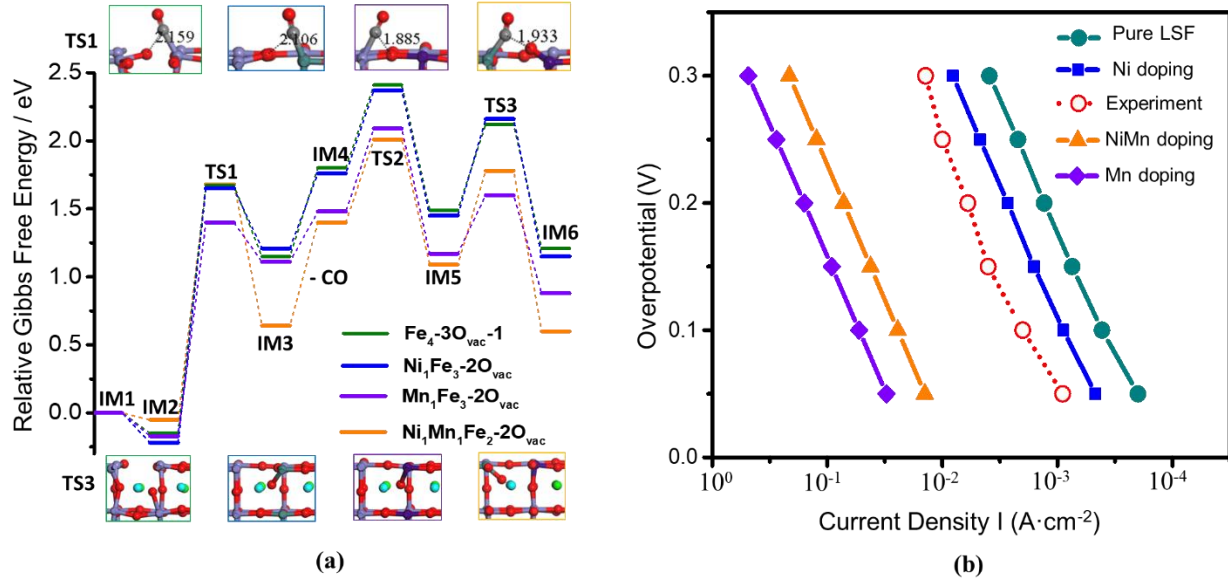

Figure 5-6. (a) Energy profile for CO_2 reduction and oxygen migration processes in the 4 selected models of pure LSF, Ni doping, Mn doping and Ni-Mn co-doping (IM5 to IM6) and SDC electrolyte (IM4 to IM5). IM: intermediate. All energies are with reference to the energies of the initial state of bare surface model with gas CO_2 (IM1). The insets provide the optimized structures of the transition states of R1 and R5 for the 4 models investigated in this study. (b) Simulated polarization curves of 4 situations. The dash line represents an experimental polarization curve [36] for a solid oxide electrolysis button cell with $La_{0.6}Sr_{0.4}FeO_{3-\delta}$ cathode (1,073K with CO_2/CO molar ratio of 50/1).

Rate constants and equilibrium constants of each elementary step at 1,073K, P(CO_2)=0.5 atm, P(CO)= 0.01 atm and P (O_2)=0.21 atm (in air) were determined by the forward and backward energy barriers of the elementary steps, entropies and frequencies of involved species. This information is listed in Table 5-3. The forward rates of every elementary step and overall rates calculated in the microkinetic models for the selected models of pure LSF, Ni doping, Mn doping

and Ni-Mn co-doping are shown in Table S5-9 in the Supporting Information. These operating conditions were chosen in order to compare our simulation results with data reported in the literature[36]. Surface coverages of all adsorbed species and vacant sites were evaluated at steady-state to calculate the overall reaction rates which can be further utilized to compute current density under different applied voltages (electrode overpotentials). Potentials of 0-0.3 V vs. open circuit voltage (OCV) were considered in this study. At higher potentials, it is reported that mass transfer (concentration polarization) is always the rate limiting step for CO_2 electrolysis [224].

Table 5-3. Forward rate constants and equilibrium constants of the elementary steps of the 4 selected models calculated at 1073K, $P(CO_2)$=0.5 atm, $P(CO)$= 0.01 atm and $P(O_2)$=0.21 atm (in air) with and without considering the effect of electrode overpotential.

Reaction step	Fe$_4$-3O$_{vac}$-1		Ni$_1$Fe$_3$-2O$_{vac}$		Mn$_1$Fe$_3$-2O$_{vac}$		Ni$_1$Mn$_1$Fe$_2$-2O$_{vac}$	
	k_{for} (s^{-1})	K	k_{for} (s^{-1})	K	k_{for} (s^{-1})	K	k_{for} (s^{-1})	K
R1	7.47×10^8	1.57×10^4	7.47×10^8	4.88×10^3	7.47×10^8	4.85×10^3	7.47×10^8	1.14×10^3
R2	2.28×10^4	8.20×10^{-6}	1.48×10^4	1.22×10^{-6}	8.36×10^5	1.26×10^{-5}	9.15×10^4	1.08×10^{-3}
R3	1.36×10^9	1.45×10^0	9.83×10^9	1.05×10^1	1.77×10^9	1.88×10^1	8.36×10^9	8.92×10^0
R4	1.33×10^{10}	3.27×10^1	1.33×10^{10}	3.27×10^1	1.33×10^{10}	3.27×10^1	1.33×10^{10}	3.27×10^1
R5	4.84×10^9	1.76×10^1	2.30×10^9	2.77×10^1	4.86×10^{10}	2.81×10^1	2.55×10^9	1.81×10^2
R2(0.3V)	5.85×10^5	5.39×10^{-3}	3.80×10^5	8.01×10^{-4}	2.15×10^7	8.29×10^{-3}	2.35×10^6	7.13×10^{-1}

The forward rate constants and equilibrium constants of R2 is the smallest compared to the rest of the elementary steps; thus, it is deemed as the rate-controlling step. We have also calculated the "degree of rate control" according to Campbell's theory [212] and verified R2 is indeed the rate-limiting step. Upon the addition of the cathode overpotential, the forward rate constants and

equilibrium constants for R2 increased up to 2-3 orders of magnitude but still remain as the rate-controlling step. This result agrees well with previous experimental observations: perovskite still has relatively low catalytic activity towards CO_2 reduction compared with the conventional Ni/YSZ cathode materials [31, 35, 113].

The kinetic relationship between cell voltage and current density is represented by the simulated polarization curves shown in Figure 5-6(b). Some assumptions were made to simplify the calculations [52]: *i*) ohmic losses can be neglected due to the high ionic conductivity of SDC electrolyte [30]; *ii*) anode potential is fixed at its equilibrium potential, which indicates the anode overpotential is ignored; therefore, the cell voltage vs. OCV is equal to the cathode bias potential in this study. Our previous study has shown that CO_2 adsorption (R1) and CO desorption (R3) process were barely affected by the electric field because they are not ionic in SOEC [52]. Hence, only CO_2 reduction (R2) was considered as charge transfer step.

As shown in Figure 5-6(b), our simulated polarization curves for pure LSF models and Ni doping model are in quantitative agreement with previous experimental polarization curves on the order of magnitude [36] for a solid oxide electrolysis button cell with $La_{0.6}Sr_{0.4}FeO_{3-\delta}$ cathode (1,073K with CO_2/CO molar ratio of 50/1). The Mn doping model exhibits the highest performance as expected because of the lowest CO_2 dissociation energy barrier, which is consistent with experimental results: $La_{0.6}Sr_{0.4}Fe_{0.8}Mn_{0.2}O_{3-\delta}$ shows much higher activity (current density) of CO_2 electrolysis compared with Co, Cu and Ni doped LSF [36]. Experimentally, the performance of LSF with Mn doping is slightly higher than that of pure LSF and Ni doped LSF, whereas the current density of those three models are still in the same order of magnitude[36]. The simulated current density for the models with Mn doping and Ni-Mn co-doping have almost 2 orders of magnitude difference compared to that of other models (i.e. pure LSF model and Ni doping model) and

experimental data [36]. This is mostly because our micro-kinetic model is very sensitive to the energy barriers of rate-limiting step [164] as shown in sensitivity analysis (Figure S5-3). The current density would decrease by more than 2 orders of magnitude when increasing the energy barrier of CO_2 reduction by 20%. Despite this observation, our model still captured the same trends of Mn doping, Ni doping and pure LSF with reported experimental results [35, 36, 113]. The performance of Ni-Mn co-doping model is a little lower than that observed for the Mn doping model but still demonstrates quite high current density. Taking into consideration both oxygen vacancy formation energy and the performance of the activation stage under SOEC operating conditions, LSF with Ni-Mn co-doping is the most promising candidate as cathode materials for CO_2 reduction in SOEC. Our study suggests that co-doping represents an effective strategy to bypass the limitations of materials with single doping on the activation stage of high temperature CO_2 reduction reaction.

5.4. Summary

To achieve the second objective of this thesis, i.e. predicting active $La(Sr)FeO_3$ based cathode materials, combined DFT+U calculations and microkinetic analysis were conducted to address the effects of surface oxygen vacancy, Ni/Mn dopants and surface doping ratio of $La(Sr)FeO_3$ based models. Simulations from the microkinetic model provided the following insights:

(1)The most stable LSF configuration , i.e. the configuration including three oxygen vacancies on surface and one in the bulk, under SOEC operating conditions (T = 1,073 K and $PO_2 =10^{-20}$ atm) were determined by performing a phase diagram derived from ab initio thermodynamic calculations.

(2)$La(Sr)Fe_{0.75}Ni_{0.125}Mn_{0.125}O_{2.75}$ with 2 adjacent surface oxygen vacancies exhibits the best

performance due to the higher oxygen affinity of Mn (lower energy barrier and reaction energy) and lower oxygen affinity of Ni (reduced oxygen vacancy formation energy) compared with Fe indicated by the Bader charge analysis.

(3)A microkinetic model based on DFT+U calculations captured the experimentally reported performance trends of LSF with Ni doping and Mn doping. It also provided reliable evidence to the prediction: Ni-Mn co-doping of LSF can be a promising candidate for direct CO_2 electrolysis in SOEC.

Chapter 6. Conclusions and Recommendations

6.1. Conclusions

CO_2 reduction in SOEC provides a promising effective solution to reduce global emissions and to enable large-scale energy storage and conversion. Multiscale modelling was performed to study CO_2 electroreduction mechanism in SOEC, which is crucial for the design of cathode materials and for facilitating the development of CO_2 conversion in SOEC. This thesis studied two different SOEC cathode materials: 1) Ni/SDC-based and 2) $La(Sr)FeO_{3-\delta}$ perovskite-based, filling the gap on theoretical studies on CO_2 reduction reaction mechanism and predicting active cathode materials. Figure 6-1 summarizes the work performed in this thesis.
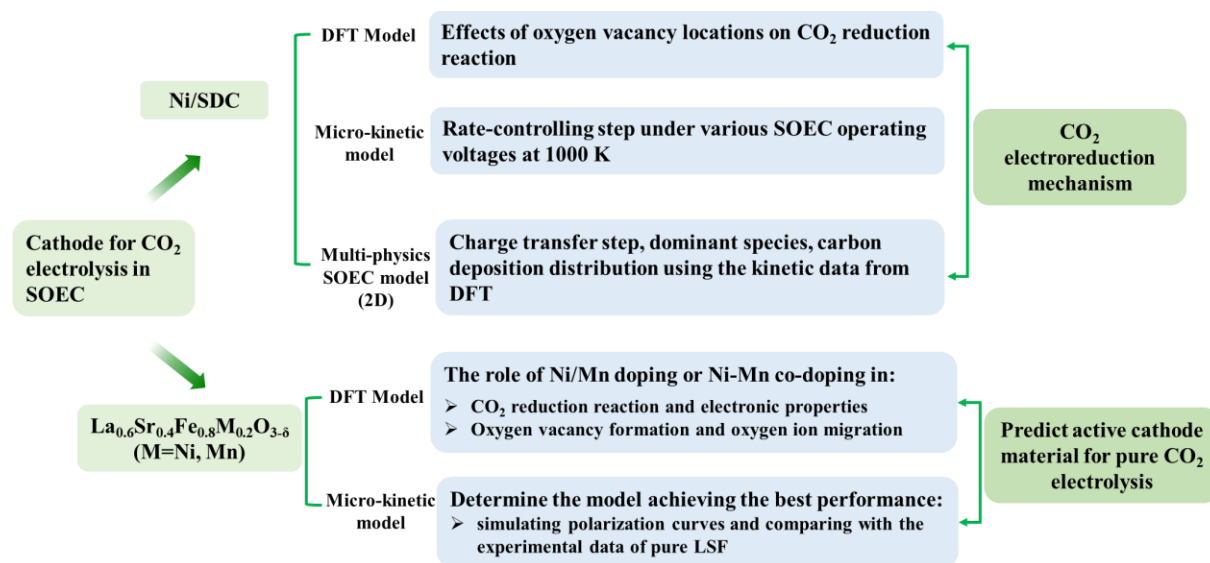

Figure 6-1. Summary of research in this thesis.

(1) For Ni/SDC, two approaches were implemented:

(1-a) A first-principles based microkinetic modeling study under SOEC operating conditions was carried out and used to gain insight on the overall CO_2 reduction process on Ni/SDC

cathode and to determine the rate-controlling steps. This study found that the interface oxygen vacancy can, not only enhance CO_2 adsorption, but also promote CO_2 reduction by lowering its energy barrier. A microkinetic analysis was built that considers the effect of electric potential and was used to explore the possibility of different charge transfer processes, with one- or two-electron charge transfers. The results show that the rate-controlling step will change from the oxygen spillover step to the CO desorption step with an increase in cathode overpotential on Ni(111)/SDC surface with non-interface oxygen vacancy. However, once interface oxygen vacancy is considered, the results indicate that CO desorption is the dominating rate-controlling step regardless of the cathode overpotential. This is because the interface oxygen vacancy makes oxygen spillover easier to occur by binding CO_2 at the interface.

(1-b) Furthermore, a 2D cathode-supported multi-scale model was built to study CO_2 electrolysis considering ionic/electronic conduction, and transport processes, which the initial microkinetic modelling did not take into account. The kinetic data of surface reactions and desorption were calculated by DFT while using fewer fitted parameters than previously reported models. Only the sticking coefficients of CO and CO_2, as well as the pre-exponential factor for the CO_2 reduction reaction were fitted to experimental data. The multi-scale model was validated with reported experimental data. The results show that the most likely charge transfer is $CO_2(s)+(s)\ 2e^- \leftrightarrow CO(s)+O(s)^{2-}$. The electrochemical reduction of CO_2 takes place mainly within about 75 μm from the cathode/electrolyte interface. CO(s) is, by far, the dominating species on the Ni catalyst surface and CO desorption is the rate-controlling step. A relatively high temperature (700 °C) and relatively low CO ratio (CO: CO_2 =1:1~1:3) are recommended to maintain low carbon deposition, low polarization resistance and high current density.

(2) For La(Sr)FeO$_{3-\delta}$ based materials, in order to reveal the catalytic mechanism of B-site dopants and predict new La(Sr)FeO$_{3-\delta}$ based materials with high catalytic activity, combined DFT+U calculations and microkinetic analysis were conducted.

(2-a) Based on DFT calculations, the most stable LSF configuration under SOEC operating conditions (T = 1,073 K and PO$_2$ = 10^{-20} atm), determined through constructing a phase diagram, is the configuration that includes three oxygen vacancies on the surface and one in the bulk. Over 45 configurations with various oxygen vacancy concentrations were considered. The CO$_2$ and CO chemical adsorption with moderate binding strength were identified as the most active adsorption configurations leading to the lowest reaction energy after exploring more than 10 and 8 possible positions for CO$_2$ and CO adsorption, respectively.

(2-b) A microkinetic model based on DFT+U calculations was developed and was able to capture experimentally reported performance trends of LSF with Ni doping and Mn doping. This model also suggests that: Ni-Mn co-doping of LSF can be a promising candidate for direct CO$_2$ electrolysis in SOEC. La(Sr)Fe$_{0.75}$Ni$_{0.125}$Mn$_{0.125}$O$_{2.75}$ with 2 adjacent surface oxygen vacancies exhibits the best performance due to the higher oxygen affinity of Mn (lower energy barrier and reaction energy) and lower oxygen affinity of Ni (reduced oxygen vacancy formation energy) compared with Fe as indicated by the Bader charge analysis.

In summary, a series of multiscale models were developed to study CO$_2$ reduction mechanism in SOEC, which i) revealed mechanistic insights into catalytic mechanism: the charge transfer step, rate-controlling step and carbon deposition; ii) predicted and facilitated the design of new cathode materials with higher catalytic activity in SOEC; and iii) provided guidance for enhancing the performance of SOEC, i.e. introducing more interface oxygen vacancies and dopants, and promoting CO desorption.

6.2. Recommendations

Based on the studies conducted in this research, the following recommendations are proposed for future work:

Further development of DFT work. The kinetic data calculated by DFT were limited to Ni(111)/SDC and La(Sr)FeO$_{3-\delta}$ (001) surfaces because these surfaces are the most stable surfaces. Although these surfaces are critical, to have a comprehensive understanding of these cathode catalysts, more DFT calculations are required on other surfaces that take into account stepped structures (e.g. stepped 211 surface).

Comprehensive multiscale simulation. Multiphysics simulation of the co-electrolysis of CO_2 and H_2O is also recommended since this process is another important application of SOEC to produce syngas ($CO+H_2$) with higher current density than CO_2 electrolysis alone. More DFT work will then be needed to consider additional reaction mechanism and to determine reaction kinetics for CO_2 and H_2O co-electrolysis. Further work is required to make the multiphysics model developed in this research with Ni/SDC cathode more comprehensive and realistic when considering larger cell, or stack, e.g. carbon nucleation mechanism, energy conservation equations. In order to describe the complete SOEC operation process with La(Sr)FeO$_3$ cathode, additional modelling details involving mass transport and geometry effects need to be considered.

Computer aided materials design using Machine learning techniques .DFT calculations in combination with machine learning was reported to accelerate catalysts discovery and guide the experimental exploration of multi-metallic systems [270]. DFT data can be used to train a machine learning model, which can also be employed to study the optimized multi-dopants in the perovskite oxides yielding the lowest reaction energy/ activation barrier of CO_2 reduction in SOEC.

Incorporation of experimental work. More experimental work is required to further support the predictions made by the models presented in this research. For instance, experimental work is needed to: 1) advance the development of Ni/cermet material by introducing more interface oxygen vacancies, and promoting CO desorption rate; 2) perform Ni and Mn co-doping in LSF cathode material.

Further investigation of cathode materials with high catalytic activity and stability. Conventional Ni/YSZ or Ni/SDC cathodes are still facing carbon deposition and Ni oxidation; also, there are currently no effective ways to solve these problems without losing catalytic activity. A new perovskite catalysts can resist carbon deposition but have lower catalytic activity and faces the problem of segregation of alkaline earth elements. Detrimental effects of such segregation on electrode performance or stability have been experimentally observed, particularly in many Sr-containing materials. Therefore, exploring new electrocatalysts with both high catalytic activity and stability is still a long-term research, e.g. perovskite oxides with B-site metal *in situ* exsolution.

Copyright Permissions

References

[1] M. Aresta, A. Dibenedetto, E. Quaranta, J. Catal., 343 (2016) 2-45.

[2] S.D. Ebbesen, S.H. Jensen, A. Hauch, M.B. Mogensen, Chem. Rev., 114 (2014) 10697-10734.

[3] Y. Li, W. Zhang, Y. Zheng, J. Chen, B. Yu, Y. Chen, M. Liu, Chem. Soc. Rev., 46 (2017) 6345-6378.

[4] D.S. Simakov, Springer, 2017.

[5] Y. Yuan, H. You, L. Ricardez-Sandoval, Chin. J. Chem. Eng., 27 (2019) 1554-1565.

[6] A. Hauch, R. Kungas, P. Blennow, A.B. Hansen, J.B. Hansen, B.V. Mathiesen, M.B. Mogensen, Science, 370 (2020) eaba6118.

[7] J. Qiao, Y. Liu, F. Hong, J. Zhang, Chem. Soc. Rev., 43 (2014) 631-675.

[8] Y. Wang, T. Liu, L. Lei, F. Chen, Fuel Process. Technol., 161 (2017) 248-258.

[9] G. Wen, D.U. Lee, B. Ren, F.M. Hassan, G. Jiang, Z.P. Cano, J. Gostick, E. Croiset, Z. Bai, L. Yang, Z. Chen, Adv. Energy Mater., 8 (2018) 1802427.

[10] M. Li, J. Lu, Z. Chen, K. Amine, Adv. Mater., 30 (2018) e1800561.

[11] Z.P. Cano, D. Banham, S. Ye, A. Hintennach, J. Lu, M. Fowler, Z. Chen, Nat. Energy, 3 (2018) 279-289.

[12] D.H. Liu, Z. Bai, M. Li, A. Yu, D. Luo, W. Liu, L. Yang, J. Lu, K. Amine, Z. Chen, Chem. Soc. Rev., 49 (2020) 5407-5445.

[13] L. Zhang, S. Hu, X. Zhu, W. Yang, J. Energ. Chem., 26 (2017) 593-601.

[14] X.G. Cao, H.Y. Zhang, in: Adv. Mater. Res., Trans Tech Publ, 2012, pp. 1802-1805.

[15] N. Kumari, P.K. Tiwari, M.A. Haider, S. Basu, ECS Trans., 78 (2017) 3329-3337.

[16] N. Kumari, M.A. Haider, S. Basu, J. Chem. Sci., 129 (2017) 1735-1740.

[17] X. Zhang, Y. Song, F. Guan, Y. Zhou, H. Lv, G. Wang, X. Bao, J. Catal., 359 (2018) 8-16.

[18] J.T. Irvine, D. Neagu, M.C. Verbraeken, C. Chatzichristodoulou, C. Graves, M.B. Mogensen, Nat. Energy, 1 (2016) 15014.

[19] Y. Zheng, J. Wang, B. Yu, W. Zhang, J. Chen, J. Qiao, J. Zhang, Chem. Soc. Rev., 46 (2017) 1427-1463.

[20] S.Y. Gómez, D. Hotza, Renew. Sust. Energ. Rev., 61 (2016) 155-174.

[21] G. Schiller, A. Ansar, M. Lang, O. Patz, J. Appl. Electrochem., 39 (2009) 293-301.

[22] Z. Wang, M. Mori, T. Araki, Int. J. Hydrog. Energy, 35 (2010) 4451-4458.

[23] S.H. Jensen, P.H. Larsen, M. Mogensen, Int. J. Hydrog. Energy, 32 (2007) 3253-3257.

[24] M.H. Sahraei, L. Ricardez-Sandoval, 2017.

[25] S.S. Bahakim, L. Ricardez-Sandoval, Ind. Eng. Chem. Res., 54 (2015) 3879-3892.

[26] X. Sun, M. Chen, Y.-L. Liu, P. Hjalmarsson, S.D. Ebbesen, S.H. Jensen, M.B. Mogensen, P.V. Hendriksen, J. Electrochem. Soc., 160 (2013) F1074-F1080.

[27] J. Yan, H. Chen, E. Dogdibegovic, J.W. Stevenson, M. Cheng, X.-D. Zhou, J. Power Sources, 252 (2014) 79-84.

[28] A. Ideris, E. Croiset, M. Pritzker, Int. J. Hydrog. Energy, 42 (2017) 9180-9187.

[29] A. Yan, M. Phongaksorn, D. Nativel, E. Croiset, J. Power Sources, 210 (2012) 374-380.

[30] C.T. Campbell, C.H. Peden, Science, 309 (2005) 713-714.

[31] S. Liu, Q. Liu, J.-L. Luo, ACS Catal., 6 (2016) 6219-6228.

[32] A. Tomita, K. Tsunekawa, T. Hibino, S. Teranishi, Y. Tachi, M. Sano, Solid State Ion., 177 (2006) 2951-2956.

[33] M. Li, B. Hua, J.-l. Luo, S.P. Jiang, J. Pu, B. Chi, L. Jian, J. Mater. Chem. A, 3 (2015) 21609-21617.

[34] J. Ma, C. Jiang, P.A. Connor, M. Cassidy, J.T. Irvine, J. Mater. Chem. A, 3 (2015) 19068-19076.

[35] S. Liu, Q. Liu, J.-L. Luo, J. Mater. Chem. A, 5 (2017) 2673-2680.

[36] T. Ishihara, S. Wang, K.-T. Wu, Solid State Ion., 299 (2017) 60-63.

[37] L. Ye, M. Zhang, P. Huang, G. Guo, M. Hong, C. Li, J.T. Irvine, K. Xie, Nat. Commun., 8 (2017) 1-10.

[38] L. Ricardez-Sandoval, Can. J. Chem. Eng., 89 (2011) 1324-1341.

[39] D. Maroudas, American Institute of Chemical Engineers. AIChE Journal, 46 (2000) 878.

[40] Y. Chen, Y. Huang, T. Cheng, W.A. Goddard, 3rd, J. Am. Chem. Soc., 141 (2019) 11651-11657.

[41] D. Chaffart, L. Ricardez-Sandoval, J. Process Control, 60 (2017) 128-140.

[42] D. Chaffart, L. Ricardez-Sandoval, Can. J. Chem. Eng., 96 (2018) 113-131.

[43] M.R. Singh, J.D. Goodpaster, A.Z. Weber, M. Head-Gordon, A.T. Bell, Proc. Natl. Acad. Sci. U. S. A., 114 (2017) E8812-E8821.

[44] F. Che, J.T. Gray, S. Ha, N. Kruse, S.L. Scott, J.-S. McEwen, ACS Catal., 8 (2018) 5153-5174.

[45] H. You, Y. Yuan, J. Li, L. Ricardez-Sandoval, IFAC-PapersOnLine, 51 (2018) 97-102.

[46] J.K. Nørskov, F. Abild-Pedersen, F. Studt, T. Bligaard, Proc. Natl. Acad. Sci. U. S. A., 108 (2011) 937-943.

[47] Z.W. Ulissi, A.J. Medford, T. Bligaard, J.K. Nørskov, Nat. Commun., 8 (2017) 1-7.

[48] F. Che, J.T. Gray, S. Ha, J.-S. McEwen, ACS Catal., 7 (2017) 551-562.

[49] B. Ren, E. Croiset, L. Ricardez-Sandoval, J. Catal., 383 (2020) 273-282.

[50] X. Nie, W. Luo, M.J. Janik, A. Asthagiri, J. Catal., 312 (2014) 108-122.

[51] L.D. Chen, M. Urushihara, K. Chan, J.K. Nørskov, ACS Catal., 6 (2016) 7133-7139.

[52] B. Ren, J. Li, G. Wen, L. Ricardez-Sandoval, E. Croiset, J. Phys. Chem. C, 122 (2018) 21151-21161.

[53] J. Ye, C.-j. Liu, D. Mei, Q. Ge, J. Catal., 317 (2014) 44-53.

[54] C. Fan, Y.-A. Zhu, M.-L. Yang, Z.-J. Sui, X.-G. Zhou, D. Chen, Ind. Eng. Chem. Res., 54 (2015) 5901-5913.

[55] F. Che, J.T. Gray, S. Ha, J.-S. McEwen, ACS Catal., 7 (2017) 6957-6968.

[56] V. Menon, Q. Fu, V.M. Janardhanan, O. Deutschmann, J. Power Sources, 274 (2015) 768-781.

[57] J. Li, Z. Bai, E. Croiset, J. Power Sources, 333 (2016) 164-172.

[58] Y. Shi, Y. Luo, N. Cai, J. Qian, S. Wang, W. Li, H. Wang, Electrochim. Acta, 88 (2013) 644-653.

[59] H. Xu, B. Chen, J. Irvine, M. Ni, Int. J. Hydrog. Energy, 41 (2016) 21839-21849.

[60] C. Ren, Y. Gan, C. Yang, M. Lee, R.D. Green, X. Xue, J. Appl. Electrochem., 48 (2018) 959-971.

[61] A. Jun, J. Kim, J. Shin, G. Kim, ChemElectroChem, 3 (2016) 511-530.

[62] Z. Wu, M. Liu, Solid State Ion., 93 (1996) 65-84.

[63] A. Chroneos, B. Yildiz, A. Tarancón, D. Parfitt, J.A. Kilner, Energy Environ. Sci., 4 (2011) 2774-2789.

[64] D. Neagu, J.T. Irvine, Chem. Mater., 23 (2011) 1607-1617.

[65] A. Atkinson, S. Barnett, R.J. Gorte, J. Irvine, A.J. McEvoy, M. Mogensen, S.C. Singhal, J. Vohs, Nat. Mater., 3 (2004) 17.

[66] M. Alaydrus, M. Sakaue, S.M. Aspera, T.D. Wungu, T.P. Linh, H. Kasai, T. Ishihara, T. Mohri, J. Phys. Condens Matter., 25 (2013) 225401.

[67] P.P. Dholabhai, S. Anwar, J.B. Adams, P.A. Crozier, R. Sharma, Model Simul. Mat. Sci. Eng., 20 (2012) 015004.

[68] P.P. Dholabhai, J.B. Adams, P. Crozier, R. Sharma, Phys. Chem. Chem. Phys., 12 (2010) 7904-7910.

[69] H. Yoshida, Solid State Ion., 160 (2003) 109-116.

[70] A. Ismail, J. Hooper, J.B. Giorgi, T.K. Woo, Phys. Chem. Chem. Phys., 13 (2011) 6116-6124.

[71] T. Ishihara, Springer Science & Business Media, 2009.

[72] M.A. Henderson, W.S. Epling, C.L. Perkins, C.H. Peden, U. Diebold, J. Phys. Chem. B, 103 (1999) 5328-5337.

[73] M.H. Weng, H.T. Chen, Y.C. Wang, S.P. Ju, J.G. Chang, M.C. Lin, Langmuir, 28 (2012) 5596-5605.

[74] Y. Zhang, Z. Yang, M. Wang, J. Power Sources, 279 (2015) 759-765.

[75] Y. Zhang, Z. Fu, M. Wang, Z. Yang, J. Power Sources, 261 (2014) 136-140.

[76] J.-h. Myung, S.-D. Kim, T.H. Shin, D. Lee, J.T. Irvine, J. Moon, S.-H. Hyun, J. Mater. Chem. A, 3 (2015) 13801-13806.

[77] M. Gong, X. Liu, J. Trembly, C. Johnson, J. Power Sources, 168 (2007) 289-298.

[78] R.J. Gorte, H. Kim, J.M. Vohs, J. Power Sources, 106 (2002) 10-15.

[79] H. Devianto, S.P. Yoon, S.W. Nam, J. Han, T.-H. Lim, J. Power Sources, 159 (2006) 1147-1152.

[80] S. Lee, J.-M. Kim, H.S. Hong, S.-K. Woo, J. Alloys Compd., 467 (2009) 614-621.

[81] S. Park, J.M. Vohs, R.J. Gorte, Nature, 404 (2000) 265-267.

[82] K. Sasaki, K. Susuki, A. Iyoshi, M. Uchimura, N. Imamura, H. Kusaba, Y. Teraoka, H. Fuchino, K. Tsujimoto, Y. Uchida, N. Jingo, J. Electrochem. Soc., 153 (2006) A2023.

[83] A. Fuerte, R. Valenzuela, M. Escudero, L. Daza, Int. J. Hydrog. Energy, 39 (2014) 4060-4066.

[84] J.P. Trembly, A.I. Marquez, T.R. Ohrn, D.J. Bayless, J. Power Sources, 158 (2006) 263-273.

[85] T. Ishihara, Solid State Ion., 132 (2000) 209-216.

[86] D.K. Niakolas, M. Athanasiou, S.G. Neophytides, S. Bebelis, ECS Trans., 35 (2011) 1329-1336.

[87] A. Babaei, L. Zhang, E. Liu, S.P. Jiang, Int. J. Hydrog. Energy, 37 (2012) 15301-15310.

[88] T. Hibino, A. Hashimoto, M. Yano, M. Suzuki, M. Sano, Electrochim. Acta, 48 (2003) 2531-2537.

[89] Y. Zhang, R. Knibbe, J. Sunarso, Y. Zhong, W. Zhou, Z. Shao, Z. Zhu, Adv. Mater., 29 (2017) 1700132.

[90] A. Atkinson, S. Barnett, R.J. Gorte, J.T. Irvine, A.J. McEvoy, M. Mogensen, S.C. Singhal, J. Vohs, Nat. Mater., 3 (2004) 17-27.

[91] S. Xu, S. Li, W. Yao, D. Dong, K. Xie, J. Power Sources, 230 (2013) 115-121.

[92] P. Addo, B. Molero‑Sanchez, M. Chen, S. Paulson, V. Birss, Fuel cells, 15 (2015) 689-696.

[93] Z. Cao, B. Wei, J. Miao, Z. Wang, Z. Lü, W. Li, Y. Zhang, X. Huang, X. Zhu, Q. Feng, Y. Sui, Electrochem. Commun., 69 (2016) 80-83.

[94] W. Qi, Y. Gan, D. Yin, Z. Li, G. Wu, K. Xie, Y. Wu, J. Mater. Chem. A, 2 (2014) 6904-6915.

[95] Y.Q. Zhang, J.H. Li, Y.F. Sun, B. Hua, J.L. Luo, ACS Appl. Mater. Interfaces, 8 (2016) 6457-6463.

[96] Y. Li, X. Chen, Y. Yang, Y. Jiang, C. Xia, ACS Sustain. Chem. Eng., 5 (2017) 11403-11412.

[97] B. Zhao, B. Yan, S. Yao, Z. Xie, Q. Wu, R. Ran, D. Weng, C. Zhang, J.G. Chen, J. Catal., 358 (2018) 168-178.

[98] M.A. Green, A. Ho-Baillie, H.J. Snaith, Nat. Photonics, 8 (2014) 506-514.

[99] T. Ishihara, K.-T. Wu, S. Wang, ECS Trans., 66 (2015) 197-205.

[100] H. Kleinke, Chem. Mater., 22 (2010) 604-611.

[101] Y. Li, P. Sonar, L. Murphy, W. Hong, Energy Environ. Sci., 6 (2013) 1684-1710.

[102] L.M. Kozycz, C. Guo, J.G. Manion, A.J. Tilley, A.J. Lough, Y. Li, D.S. Seferos, J. Mater. Chem. C, 3 (2015) 11505-11515.

[103] S. Baig, P. Kumar, J. Ngai, Y. Li, S. Ahmed, ChemPhysChem, 21 (2020) 895-907.

[104] P. Slater, J. Irvine, T. Ishihara, Y. Takita, J. Solid State Chem., 139 (1998) 135-143.

[105] M. Escudero, J. Irvine, L. Daza, J. Power Sources, 192 (2009) 43-50.

[106] M.S. Islam, R.A. Davies, J. Mater. Chem., 14 (2004) 86-93.

[107] B.A. Kuropatwa, A. Assoud, H. Kleinke, Z. Anorg. Allg. Chem., 639 (2013) 2411-2420.

[108] S.P. Jiang, J. Mater. Sci., 43 (2008) 6799-6833.

[109] J. Mizusaki, N. Mori, H. Takai, Y. Yonemura, H. Minamiue, H. Tagawa, M. Dokiya, H. Inaba, K. Naraya, T. Sasamoto, Solid State Ion., 129 (2000) 163-177.

[110] T. Montini, M. Bevilacqua, E. Fonda, M.F. Casula, S. Lee, C. Tavagnacco, R. Gorte, P. Fornasiero, Chem. Mater., 21 (2009) 1768-1774.

[111] R. Chiba, F. Yoshimura, Y. Sakurai, Solid State Ion., 152 (2002) 575-582.

[112] Y. Li, B. Hu, C. Xia, W.Q. Xu, J.P. Lemmon, F. Chen, J. Mater. Chem. A, 5 (2017) 20833-20842.

[113] Y. Tian, H. Zheng, L. Zhang, B. Chi, J. Pu, J. Li, J. Electrochem. Soc., 165 (2018) F17-F23.

[114] Y. Nishihata, J. Mizuki, T. Akao, H. Tanaka, M. Uenishi, M. Kimura, T. Okamoto, N. Hamada, Nature, 418 (2002) 164-167.

[115] H. Tanaka, M. Uenishi, M. Taniguchi, I. Tan, K. Narita, M. Kimura, K. Kaneko, Y. Nishihata, J.i. Mizuki, Catal. Today, 117 (2006) 321-328.

[116] D. Neagu, T.S. Oh, D.N. Miller, H. Menard, S.M. Bukhari, S.R. Gamble, R.J. Gorte, J.M. Vohs, J.T.S. Irvine, Nat. Commun., 6 (2015) 8120.

[117] Y. Sun, J. Li, Y. Zeng, B.S. Amirkhiz, M. Wang, Y. Behnamian, J. Luo, J. Mater. Chem. A, 3 (2015) 11048-11056.

[118] Z. Du, H. Zhao, S. Yi, Q. Xia, Y. Gong, Y. Zhang, X. Cheng, Y. Li, L. Gu, K. Świerczek, ACS Nano, 10 (2016) 8660-8669.

[119] J.H. Myung, D. Neagu, D.N. Miller, J.T. Irvine, Nature, 537 (2016) 528-531.

[120] J. Zhou, T.-H. Shin, C. Ni, G. Chen, K. Wu, Y. Cheng, J.T. Irvine, Chem. Mater., 28 (2016) 2981-2993.

[121] D. Chaffart, S. Rasoulian, L. Ricardez-Sandoval, AIChE J., 62 (2016) 2374-2390.

[122] K.E. Gubbins, J.D. Moore, Ind. Eng. Chem. Res., 49 (2010) 3026-3046.

[123] S.O. Nielsen, C.F. Lopez, G. Srinivas, M.L. Klein, J. Phys.: Condens. Matter, 16 (2004) R481.

[124] G. Kimaev, L. Ricardez-Sandoval, Chem. Eng. Res. Des., 140 (2018) 33-43.

[125] J. Li, E. Croiset, L. Ricardez-Sandoval, J. Catal., 326 (2015) 15-25.

[126] J. Li, G. Liu, B. Ren, E. Croiset, Y. Zhang, L. Ricardez-Sandoval, J. Catal., 378 (2019) 176-183.

[127] S. Rasoulian, L. Ricardez-Sandoval, Chem. Eng. Sci., 116 (2014) 590-600.

[128] R.E. Rudd, J.Q. Broughton, Phys. Status Solidi B, 217 (2000) 251-291.

[129] G. Kimaev, L. Ricardez-Sandoval, J. Phys. Chem. C, 124 (2020) 18615-18627.

[130] D. Chaffart, L. Ricardez-Sandoval, Comput. Chem. Eng., 119 (2018) 465-479.

[131] V. Ramadesigan, P.W. Northrop, S. De, S. Santhanagopalan, R.D. Braatz, V.R. Subramanian, J. Electrochem. Soc., 159 (2012) R31.

[132] G. Kimaev, D. Chaffart, L. Ricardez-Sandoval, AIChE J., 66 (2020) e16262.

[133] R.D. Braatz, R.C. Alkire, E. Rusli, T.O. Drews, Chem. Eng. Sci., 59 (2004) 5623-5628.

[134] J.S.-I. Kwon, M. Nayhouse, G. Orkoulas, P.D. Christofides, Chem. Eng. Sci., 119 (2014) 30-39.

[135] Y. Chen, Y. Huang, T. Cheng, W.A. Goddard III, J. Am. Chem. Soc., 141 (2019) 11651-11657.

[136] D. Kopač, B. Likozar, M. Huš, Appl. Surf. Sci., 497 (2019) 143783.

[137] D. Sholl, J.A. Steckel, John Wiley & Sons, 2011.

[138] X. Liu, J. Xiao, H. Peng, X. Hong, K. Chan, J.K. Norskov, Nat. Commun., 8 (2017) 15438.

[139] Z.W. Ulissi, M.T. Tang, J. Xiao, X. Liu, D.A. Torelli, M. Karamad, K. Cummins, C. Hahn, N.S. Lewis, T.F. Jaramillo, K. Chan, J.K. Nørskov, ACS Catal., 7 (2017) 6600-6608.

[140] G. Wen, B. Ren, M.G. Park, J. Yang, H. Dou, Z. Zhang, Y.P. Deng, Z. Bai, L. Yang, J. Gostick, G.A. Botton, Y. Hu, Z. Chen, Angew. Chem. Int. Ed., 59 (2020) 12860-12867.

[141] X. Liu, J. Xiao, H. Peng, X. Hong, K. Chan, J.K. Norskov, Nat. Commun., 8 (2017) 15438.

[142] A.M. Ritzmann, J.M. Dieterich, E.A. Carter, Phys. Chem. Chem. Phys., 18 (2016) 12260-12269.

[143] A.M. Ritzmann, A.B. Muñoz-García, M. Pavone, J.A. Keith, E.A. Carter, Chem. Mater., 25 (2013) 3011-3019.

[144] A.M. Ritzmann, A.B. Muñoz-García, M. Pavone, J.A. Keith, E.A. Carter, MRS Communications, 3 (2013) 161-166.

[145] A.B. Muñoz-García, D.E. Bugaris, M. Pavone, J.P. Hodges, A. Huq, F. Chen, H.-C. zur Loye, E.A. Carter, J. Am. Chem. Soc., 134 (2012) 6826-6833.

[146] A.B. Muñoz‐García, M. Pavone, Int. J. Quantum Chem., 116 (2016) 1501-1506.

[147] A.B. Muñoz-García, M. Pavone, Chem. Mater., 28 (2016) 490-500.

[148] A.B. Munoz-Garcia, A.M. Ritzmann, M. Pavone, J.A. Keith, E.A. Carter, Acc. Chem. Res., 47 (2014) 3340-3348.

[149] A.M. Ritzmann, M. Pavone, A.B. Muñoz-García, J.A. Keith, E.A. Carter, J. Mater. Chem. A, 2 (2014) 8060-8074.

[150] M. Shishkin, T. Ziegler, J. Phys. Chem. C, 114 (2010) 21411-21416.

[151] M. Shishkin, T. Ziegler, ECS Trans., 35 (2011) 1611-1619.

[152] M. Shishkin, T. Ziegler, J. Phys. Chem. C, 117 (2013) 7086-7096.

[153] M. Shishkin, T. Ziegler, Phys. Chem. Chem. Phys., 16 (2014) 1798-1808.

[154] F. Che, S. Ha, J.S. McEwen, Angew. Chem. Int. Ed., 129 (2017) 3611-3615.

[155] X.-K. Gu, E. Nikolla, J. Phys. Chem. C, 119 (2015) 26980-26988.

[156] F. Che, S. Ha, J.-S. McEwen, Ind. Eng. Chem. Res., 56 (2017) 1201-1213.

[157] L. Ye, C. Pan, M. Zhang, C. Li, F. Chen, L. Gan, K. Xie, ACS Appl. Mater. Interfaces, 9 (2017) 25350-25357.

[158] H. Lv, T. Liu, X. Zhang, Y. Song, H. Matsumoto, N. Ta, C. Zeng, G. Wang, X. Bao, Angew. Chem. Int. Ed., 59 (2020) 15968-15973.

[159] G. Henkelman, B.P. Uberuaga, H. Jónsson, J. Chem. Phys., 113 (2000) 9901-9904.

[160] Q. Guo, A. Assoud, H. Kleinke, Adv. Energy Mater., 4 (2014) 1400348.

[161] J.A. Dumesic, An American Chemical Society Publication, 1993.

[162] M. Besora, F. Maseras, Wiley Interdisciplinary Reviews: Computational Molecular Science, 8 (2018) e1372.

[163] G.R. Wittreich, K. Alexopoulos, D.G. Vlachos, Handbook of Materials Modeling: Applications: Current and Emerging Materials, (2020) 1377-1404.

[164] S. Suthirakun, S.C. Ammal, A.B. Muñoz-García, G. Xiao, F. Chen, H.-C. zur Loye, E.A. Carter, A. Heyden, J. Am. Chem. Soc., 136 (2014) 8374-8386.

[165] D.Y. Jo, M.W. Lee, H.C. Ham, K.-Y. Lee, J. Catal., 373 (2019) 336-350.

[166] S.C. Ammal, A. Heyden, J. Phys. Chem. Lett., 3 (2012) 2767-2772.

[167] G. Allaire, G. Allaire, Oxford university press, 2007.

[168] Z.L. Liu, in: Multiphysics in Porous Materials, Springer, 2018, pp. 29-34.

[169] R.W. Pryor, Jones & Bartlett Publishers, 2009.

[170] E.J.F. Dickinson, H. Ekström, E. Fontes, Electrochem. Commun., 40 (2014) 71-74.

[171] G. Wen, S. Rehman, T.G. Tranter, D. Ghosh, Z. Chen, J.T. Gostick, M.A. Pope, Chem. Mater., 32 (2020) 4518-4526.

[172] S. Suter, S. Haussener, Energy Environ. Sci., 12 (2019) 1668-1678.

[173] M.R. Singh, E.L. Clark, A.T. Bell, Phys. Chem. Chem. Phys., 17 (2015) 18924-18936.

[174] L.-C. Weng, A.T. Bell, A.Z. Weber, Energy Environ. Sci., 13 (2020) 3592-3606.

[175] M. Liu, Y. Pang, B. Zhang, P. De Luna, O. Voznyy, J. Xu, X. Zheng, C.T. Dinh, F. Fan, C. Cao, F.P. de Arquer, T.S. Safaei, A. Mepham, A. Klinkova, E. Kumacheva, T. Filleter, D. Sinton, S.O. Kelley, E.H. Sargent, Nature, 537 (2016) 382-386.

[176] P.P. Yang, X.L. Zhang, F.Y. Gao, Y.R. Zheng, Z.Z. Niu, X. Yu, R. Liu, Z.Z. Wu, S. Qin, L.P. Chi, Y. Duan, T. Ma, X.S. Zheng, J.F. Zhu, H.J. Wang, M.R. Gao, S.H. Yu, J. Am. Chem. Soc., 142 (2020) 6400-6408.

[177] J.P. Stempien, Q. Sun, S.H. Chan, J. Power Technol., 93 (2013) 216-246.

[178] M. Ni, Chem. Eng. J., 164 (2010) 246-254.

[179] J. Zhang, Y. Shi, N. Cai, Electrochim. Acta, 139 (2014) 190-200.

[180] H. Xu, M.M. Maroto-Valer, M. Ni, J. Cao, J. Xuan, Appl. Energy, 242 (2019) 911-918.

[181] J. Dragsbaek Duhn, A. Degn Jensen, S. Wedel, C. Wix, Fuel Cells, 17 (2017) 442-456.

[182] K. Wu, E. Birgersson, B. Kim, P.J. Kenis, I.A. Karimi, J. Electrochem. Soc., 162 (2014) F23.

[183] Y. Xie, X. Xue, Solid State Ion., 224 (2012) 64-73.

[184] W. Li, Y. Shi, Y. Luo, N. Cai, J. Power Sources, 243 (2013) 118-130.

[185] J. Li, G. Liu, E. Croiset, Electrochim. Acta, 249 (2017) 216-226.

[186] V. Yurkiv, D. Starukhin, H.-R. Volpp, W.G. Bessler, J. Electrochem. Soc., 158 (2011) B5-B10.

[187] C.M. Stoots, J.E. O'Brien, J.S. Herring, J.J. Hartvigsen, J. Fuel Cell Sci. Technol., 6 (2009).

[188] Y. Luo, Y. Shi, W. Li, N. Cai, J. Power Sources, 379 (2018) 298-308.

[189] Y. Luo, Y. Shi, W. Li, N. Cai, Energy, 70 (2014) 420-434.

[190] Y. Luo, W. Li, Y. Shi, T. Cao, X. Ye, S. Wang, N. Cai, J. Electrochem. Soc., 162 (2015) F1129.

[191] M. Ni, Int. J. Hydrog. Energy, 37 (2012) 6389-6399.

[192] M. Navasa, C. Graves, C. Chatzichristodoulou, T. Løye Skafte, B. Sundén, H. Lund Frandsen, Int. J. Hydrog. Energy, 43 (2018) 11913-11931.

[193] M. Navasa, H.L. Frandsen, T.L. Skafte, B. Sundén, C. Graves, J. Power Sources, 394 (2018) 102-113.

[194] N. Kumari, M.A. Haider, M. Agarwal, N. Sinha, S. Basu, J. Phys. Chem. C, 120 (2016) 16626-16635.

[195] S. Ackermann, L. Sauvin, R. Castiglioni, J.L. Rupp, J.R. Scheffe, A. Steinfeld, J. Phys. Chem. C Nanomater Interfaces, 119 (2015) 16452-16461.

[196] Z. Cheng, B.J. Sherman, C.S. Lo, J. Chem. Phys., 138 (2013) 014702.

[197] Z. Yang, T.K. Woo, M. Baudin, K. Hermansson, J. Chem. Phys., 120 (2004) 7741-7749.

[198] Y.M. Choi, H. Abernathy, H.T. Chen, M.C. Lin, M. Liu, ChemPhysChem, 7 (2006) 1957-1963.

[199] D. Knapp, T. Ziegler, J. Phys. Chem. C, 112 (2008) 17311-17318.

[200] V. Singh, H. Muroyama, T. Matsui, S. Hashigami, T. Inagaki, K. Eguchi, J. Power Sources, 293 (2015) 642-648.

[201] H. Yahiro, K. Eguchi, H. Arai, Solid State Ion., 36 (1989) 71-75.

[202] G. Kresse, J. Furthmüller, Phys. Rev. B, 54 (1996) 11169.

[203] G. Kresse, J. Furthmüller, Comput. Mater. Sci., 6 (1996) 15-50.

[204] G. Kresse, D. Joubert, Phys. Rev. B, 59 (1999) 1758.

[205] J.A. White, D.M. Bird, Phys. Rev. B: Condens. Matter, 50 (1994) 4954-4957.

[206] J.P. Perdew, K. Burke, M. Ernzerhof, Phys. Rev. Lett., 77 (1996) 3865.

[207] M. Shishkin, T. Ziegler, J. Phys. Chem. C, 112 (2008) 19662-19669.

[208] B. Ren, X. Dong, Y. Yu, G. Wen, M. Zhang, Appl. Surf. Sci., 412 (2017) 374-384.

[209] B. Ren, X. Dong, Y. Yu, M. Zhang, Surf. Sci., 664 (2017) 147-154.

[210] U. von Barth, L. Hedin, J. Phys. C: Solid State Phys., 5 (1972) 1629.

[211] P.P. Dholabhai, J.B. Adams, P. Crozier, R. Sharma, The Journal of chemical physics, 132 (2010) 094104.

[212] C. Stegelmann, A. Andreasen, C.T. Campbell, J. Am. Chem. Soc., 131 (2009) 8077-8082.

[213] K. Ahn, Y.-C. Chung, K.J. Yoon, J.-W. Son, B.-K. Kim, H.-W. Lee, J.-H. Lee, J. Electroceram., 32 (2014) 72-77.

[214] D.A. Andersson, S.I. Simak, N.V. Skorodumova, I.A. Abrikosov, B. Johansson, Proc. Natl. Acad. Sci. U. S. A., 103 (2006) 3518-3521.

[215] M. Shishkin, T. Ziegler, J. Phys. Chem. C, 114 (2010) 11209-11214.

[216] R.C. Catapan, A.A. Oliveira, Y. Chen, D.G. Vlachos, J. Phys. Chem. C, 116 (2012) 20281-20291.

[217] D.W. Blaylock, T. Ogura, W.H. Green, G.J. Beran, J. Phys. Chem. C, 113 (2009) 4898-4908.

[218] Y.-A. Zhu, D. Chen, X.-G. Zhou, W.-K. Yuan, Catal. Today, 148 (2009) 260-267.

[219] C.T. Campbell, L. Árnadóttir, J.R. Sellers, Z. Phys. Chem. (Muenchen, Ger.), 227 (2013).

[220] H.P. Koch, P. Singnurkar, R. Schennach, A. Stroppa, F. Mittendorfer, J. Phys. Chem. C, 112 (2008) 806-812.

[221] A. Stroppa, F. Mittendorfer, J. Phys. Chem. C, 115 (2011) 21320-21323.

[222] A. Stroppa, F. Mittendorfer, J.N. Andersen, G. Parteder, F. Allegretti, S. Surnev, F. Netzer, J. Phys. Chem. C, 113 (2008) 942-949.

[223] Z.-J. Zhao, Z. Li, Y. Cui, H. Zhu, W.F. Schneider, W.N. Delgass, F. Ribeiro, J. Greeley, J. Catal., 345 (2017) 157-169.

[224] X. Yue, J.T. Irvine, Solid State Ion., 225 (2012) 131-135.

[225] C. Graves, S.D. Ebbesen, M. Mogensen, Solid State Ion., 192 (2011) 398-403.

[226] J. Mukherjee, S. Linic, J. Electrochem. Soc., 154 (2007) B919-B924.

[227] F. Che, S. Ha, J.-S. McEwen, J. Phys. Chem. C, 120 (2016) 14608-14620.

[228] J. Neugebauer, M. Scheffler, Phys. Rev. B: Condens. Matter, 46 (1992) 16067-16080.

[229] K.P. Kuhl, T. Hatsukade, E.R. Cave, D.N. Abram, J. Kibsgaard, T.F. Jaramillo, J. Am. Chem. Soc., 136 (2014) 14107-14113.

[230] X. Yue, J.T. Irvine, J. Electrochem. Soc., 159 (2012) F442-F448.

[231] X. Yue, J.T. Irvine, ECS Trans., 68 (2015) 3535-3551.

[232] V.M. Janardhanan, O. Deutschmann, J. Power Sources, 162 (2006) 1192-1202.

[233] E. Shustorovich, H. Sellers, Surf. Sci. Rep., 31 (1998) 1-119.

[234] W. Yao, E. Croiset, J. Power Sources, 248 (2014) 777-788.

[235] N. Al-Sarraf, J. Stuckless, C. Wartnaby, D. King, Surf. Sci., 283 (1993) 427-437.

[236] Y. Xie, X. Xue, J. Power Sources, 209 (2012) 81-89.

[237] J. Kong, K. Sun, D. Zhou, N. Zhang, J. Mu, J. Qiao, J. Power Sources, 166 (2007) 337-342.

[238] T.L. Skafte, P. Blennow, J. Hjelm, C. Graves, J. Power Sources, 373 (2018) 54-60.

[239] J. Carrasco, L. Barrio, P. Liu, J.A. Rodriguez, M.V. Ganduglia-Pirovano, J. Phys. Chem. C, 117 (2013) 8241-8250.

[240] K. Hou, R. Hughes, Chem. Eng. J., 82 (2001) 311-328.

[241] W.J. Fleming, J. Electrochem. Soc., 124 (1977) 21.

[242] J.P. Stempien, Q. Liu, M. Ni, Q. Sun, S.H. Chan, Electrochim. Acta, 147 (2014) 490-497.

[243] S.D. Ebbesen, M. Mogensen, J. Power Sources, 193 (2009) 349-358.

[244] Y. Li, P. Li, B. Hu, C. Xia, J. Mater. Chem. A, 4 (2016) 9236-9243.

[245] S.-D. Kim, D.-W. Seo, A.K. Dorai, S.-K. Woo, Int. J. Hydrog. Energy, 38 (2013) 6569-6576.

[246] K. Sasaki, Y. Teraoka, J. Electrochem. Soc., 150 (2003) A878.

[247] L. Zhu, X. Liu, F. Han, J. Sun, H. Bi, H. Wang, S. Yu, L. Pei, Solid State Ion., 288 (2016) 115-119.

[248] S. Wang, H. Tsuruta, M. Asanuma, T. Ishihara, Adv. Energy Mater., 5 (2015) 1401003.

[249] P. Kim-Lohsoontorn, J. Bae, J. Power Sources, 196 (2011) 7161-7168.

[250] H. Ding, Z. Tao, S. Liu, J. Zhang, Sci. Rep., 5 (2015) 18129.

[251] A. Jun, J. Kim, J. Shin, G. Kim, ChemElectroChem, 3 (2016) 511-530.

[252] S. Kattel, P. Liu, J.G. Chen, J. Am. Chem. Soc., 139 (2017) 9739-9754.

[253] K. Chakrapani, G. Bendt, H. Hajiyani, T. Lunkenbein, M.T. Greiner, L. Masliuk, S. Salamon, J. Landers, R. Schlögl, H. Wende, ACS Catal., 8 (2018) 1259-1267.

[254] W. Koehler, E. Wollan, J. Phys. Chem. Solids, 2 (1957) 100-106.

[255] Y.-L. Lee, J. Kleis, J. Rossmeisl, D. Morgan, Phys. Rev. B, 80 (2009) 224101.

[256] B. Ren, L. Ricardez-Sandoval, E. Croiset, ECS Trans., 91 (2019) 2673.

[257] J. Druce, H. Tellez, M. Burriel, M. Sharp, L. Fawcett, S. Cook, D. McPhail, T. Ishihara, H. Brongersma, J. Kilner, Energy Environ. Sci., 7 (2014) 3593-3599.

[258] S. Grimme, J. Comput. Chem., 27 (2006) 1787-1799.

[259] J. Mizusaki, M. Yoshihiro, S. Yamauchi, K. Fueki, J. Solid State Chem., 58 (1985) 257-266.

[260] L. Wang, T. Maxisch, G. Ceder, Phys. Rev. B, 73 (2006) 195107.

[261] P. Linstrom, W. Mallard, in, MD, 2003.

[262] M. Kuhn, S. Hashimoto, K. Sato, K. Yashiro, J. Mizusaki, Solid State Ion., 195 (2011) 7-15.

[263] Y. Yang, Y. Li, Y. Jiang, M. Zheng, T. Hong, X. Wu, C. Xia, Electrochim. Acta, 284 (2018) 159-167.

[264] A. Nenning, A.K. Opitz, C. Rameshan, R. Rameshan, R. Blume, M. Havecker, A. Knop-Gericke, G. Rupprechter, B. Klotzer, J. Fleig, J. Phys. Chem. C Nanomater Interfaces, 120 (2016) 1461-1471.

[265] K. Nomura, Y. Ujihira, T. Hayakawa, K. Takehira, Appl. Catal., A-Gen, 137 (1996) 25-36.

[266] T. Sakpal, L. Lefferts, J. Catal., 367 (2018) 171-180.

[267] W.L. Huang, Q. Zhu, W. Ge, H. Li, Comput. Mater. Sci., 50 (2011) 1800-1805.

[268] F. Zhou, M. Cococcioni, C.A. Marianetti, D. Morgan, G. Ceder, Phys. Rev. B, 70 (2004) 235121.

[269] S. Piskunov, E. Heifets, T. Jacob, E.A. Kotomin, D.E. Ellis, E. Spohr, Phys. Rev. B, 78 (2008) 121406.

[270] M. Zhong, K. Tran, Y. Min, C. Wang, Z. Wang, C.-T. Dinh, P. De Luna, Z. Yu, A.S. Rasouli, P. Brodersen, Nature, 581 (2020) 178-183.

Appendix A: Supporting Information for Chapter 3

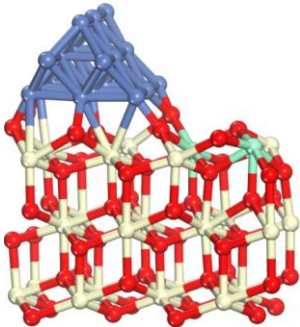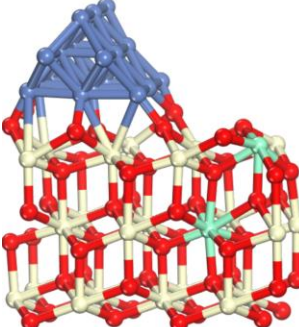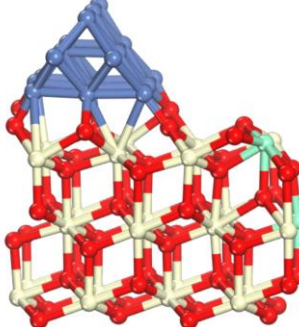Table S3-1. Free energy of Ni (111)/SDC with different Sm substitution positions

Energy (eV)	-661.8089	-661.8377	-661.6978
Different Sm substitution positions			

Table S3-2. The frequencies of all involved specie (IS: initial state; TS: transition state; FS: final state).

Model	Elementary step	frequencies (cm^{-1})
	R2IS (R1FS)	[1829 1182 629 521 239 152 131 95 54];
	R2TS	[1769 532 411 368 353 245 167 79];
	R2FS	[1766 530 503 369 340 299 283 171 118];
	R3IS	[1765 398 378 316 159 124];
	R4IS	[537 487 263];
	R4TS	[627 154];
Model 1	R4FS	[544 222 194];
	R5IS	[457 385 267];
	R5TS	[640 197];
	R5FS	[431 334 300];
	R6IS	[460 296 246];
	R6TS	[666 173];
	R6FS	[487 401 290];

	R2IS	[1580 819 667 452 339 270 235 144 112];
	R2TS	[1743 535 467 402 300 258 183 118];
	R2FS	[1766 479 399 361 289 261 213 155 128];
	R3IS	[1729 422 372 264 176 112];
	R4IS	[457 385 267];
Model 2	R4TS	[640 197];
	R4FS	[431 334 300];
	R5IS	[465 321 175];
	R5TS	[585 305];
	R5FS	[456 411 296];

Table S3-3. Adsorption energies (E_{ads} /eV) for CO_2 and CO adsorption.

Model	Adsorption position and species	E_{ads}/eV
Model 1	CO_2 on top of Ni cluster	-0.52
	CO_2 at the interface of Ni and SDC	-0.15
	CO on top of Ni cluster	-1.78
	CO at the interface of Ni and SDC	-1.82
Model 2	CO_2 on top of Ni cluster	-0.69
	CO_2 at the interface of Ni and SDC	-1.01
	CO on top of Ni cluster	-2.01
	CO at the interface of Ni and SDC	-2.19

Table S3-4. The transition states of R4-R6 on model 1

TS of R4 on model 1	TS of R5 on model 1	TS of R6 on model 1
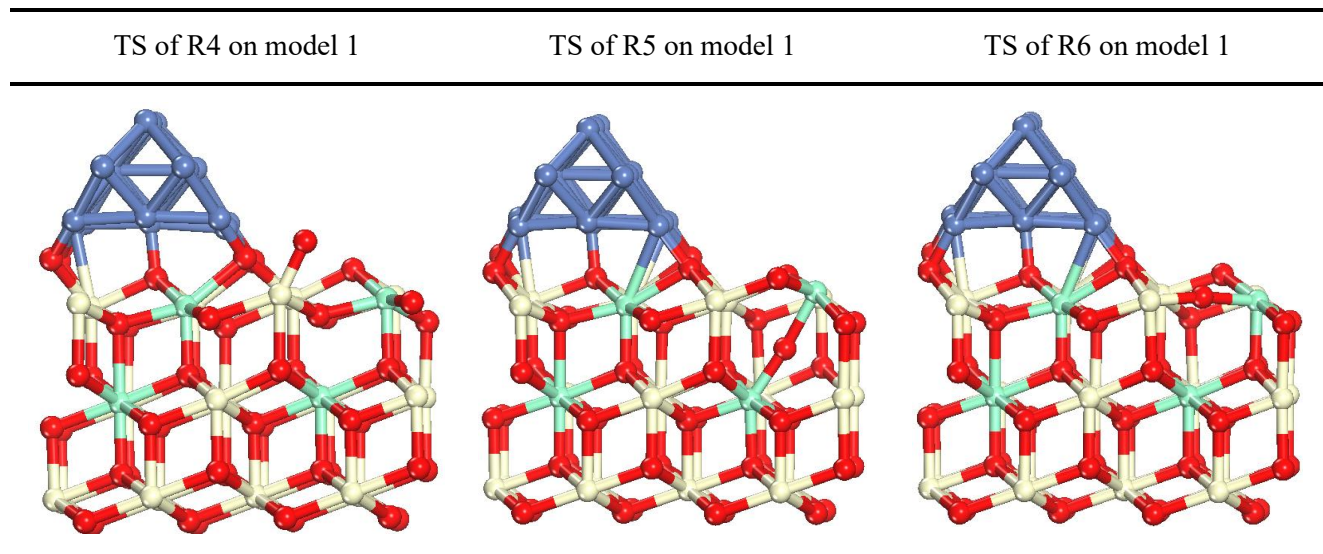
Table S3-5. The transition states of R4, R5 on model 2

TS of R4 on model 1	TS of R5 on model 1
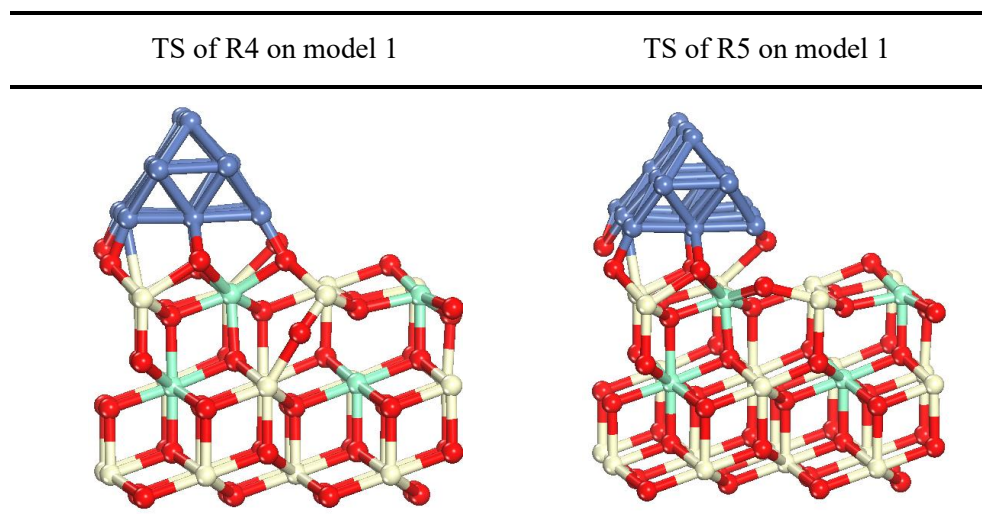
Table S3-6. The calculated rate constants and equilibrium constants for all the possibilities of charge transfer steps at a representative electrode overpotential of 0.3V (1000 K) (P_{CO_2}=0.7 atm, P_{CO}= 0.3 atm and P_{O_2}=0.21 atm (in air)).

Model	Charge transfer step	One-electron charge transfer		Two-electron charge transfer	
		k_{for} (s^{-1})	K	k_{for} (s^{-1})	K
Model 1	R2	6.58×10^9	3.85×10^2	3.75×10^{10}	1.25×10^4
	R4	6.73×10^6	5.42×10^1	3.83×10^7	1.76×10^3
Model 2	R2	5.61×10^{12}	6.81×10^6	3.19×10^{13}	2.21×10^8

Table S3-7 shown below lists the CO adsorption energies at the interface of Model 2 using HSE06 and GGA+U functional, and the corresponding $E_{absorbates/slab}$, $E_{adsorbates}$ and E_{slab} used to calculate CO adsorption energy. As shown in Table S7, the difference in CO adsorption energy is 0.09 eV, or 4% of the value determined from the normal GGA functional (-2.19 eV).

Table S3-7. CO adsorption energies using HSE06 and GGA+U functional

CO adsorption energy/eV (GGA+U)			CO adsorption energy/eV (HSE06)		
-2.19			-2.10		
$E_{adsorbates}$/eV	E_{slab}/eV	$E_{absorbates/slab}$/eV	$E_{adsorbates}$/eV	E_{slab}/eV	$E_{absorbates/slab}$/eV
-14.79	-650.39	-667.37	-20.48	-972.92	-995.50

By substituting the corresponding CO adsorption energy value calculated by hybrid functional HSE06 into our micro-kinetic model, it was found that the values of the corresponding X_{RC} ("degree of rate control") for every elementary steps remain the same as using CO adsorption energy by GGA +U functional. Similar calculations were done for Model 1, and the same conclusion was reached, i.e. no impact on the values of X_{RC}. Thus, the small difference of CO adsorption energy obtained by hybrid functional HSE06 does not change the outcomes of the present study.
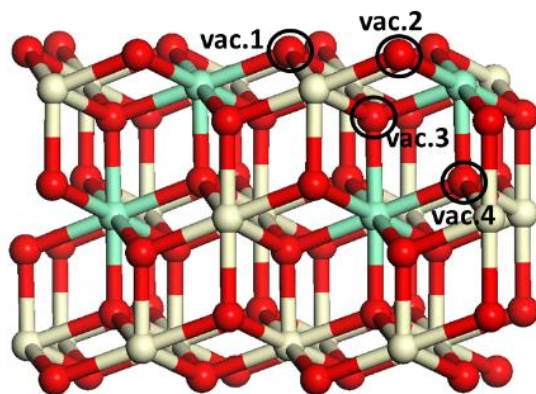
Vacancy	vac-1	vac-2	vac-3	vac-4
O_{vac} formation energy(eV)	-0.8684	-0.7815	-1.1251	-0.8296

Figure S3-1. Configurations of SDC with different oxygen vacancies and their corresponding oxygen vacancy formation energies.
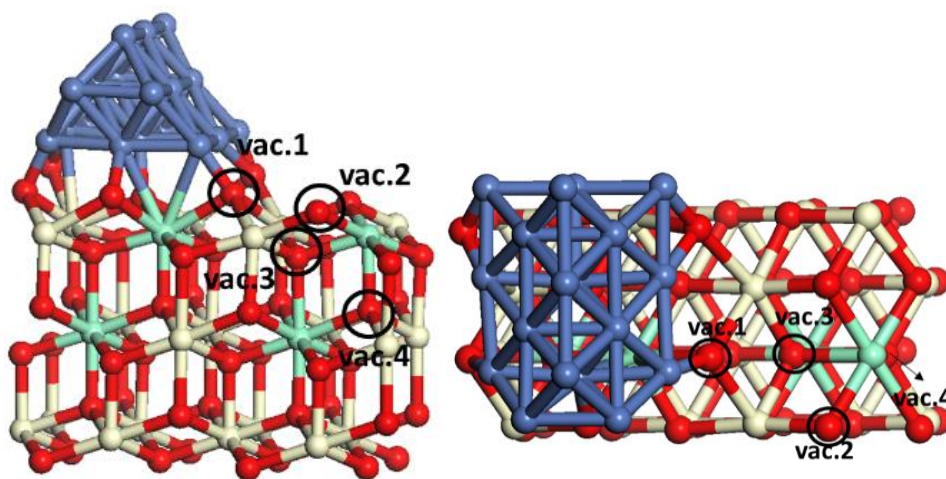
Vacancy	Ni-SDC-vac-1	Ni-SDC-vac-2	Ni-SDC-vac-3	Ni-SDC-vac-4
O_{vac} formation energy(eV)	3.6673	2.2797	2.6596	2.983

Figure S3-2. Configurations of Ni-SDC with different oxygen vacancies and their corresponding oxygen vacancy formation energies.
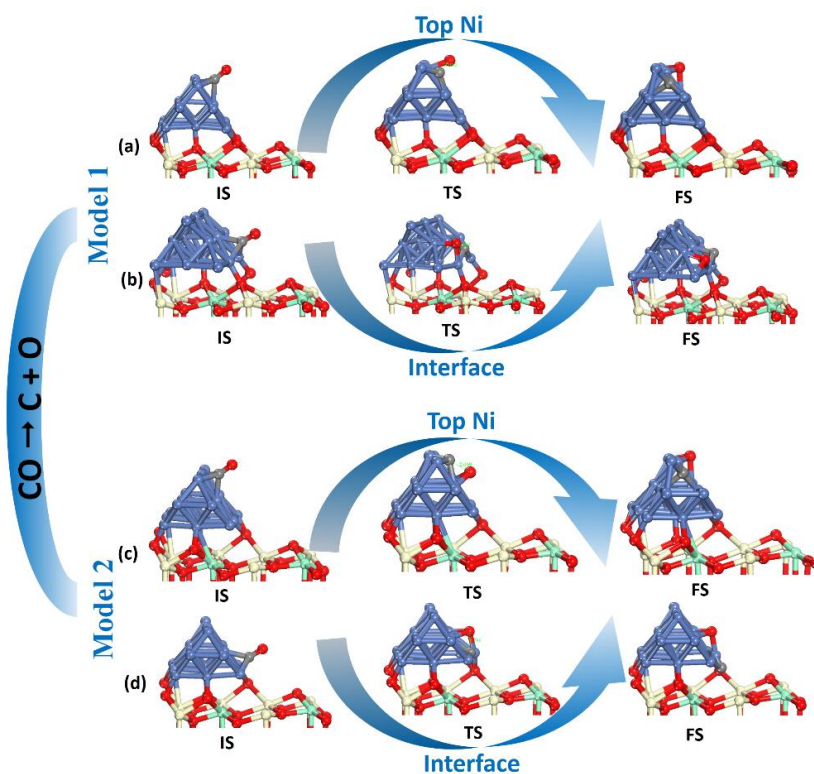
Figure S3-3. Configurations of the initial states (IS), the transition states (TS) and the final states (FS) of the CO dissociation reaction on Ni-SDC with non-interface oxygen vacancy (Model 1) with interface oxygen vacancy (Model 2). CO dissociation a) on top of Ni cluster of model 1; b) at the interface of Ni cluster and SDC of model 1; c) on top of Ni cluster of model 2; d) at the interface of Ni/SDC of model 2.

CO decomposition reaction is also investigated on the two models (Figure S3-3a-d). The results indicate that, on Model 1, CO decomposition has a lower energy barrier at the interface (3.08 eV) than that of the top of Ni cluster (3.84 eV), see Table 1 in the manuscript. This lower energy barrier for CO decomposition at the interface indicates that interface may accelerate the carbon deposition. This DFT result is consistent with experimental observations that carbon deposition at the cathode/electrolyte interface is more serious than that at the electrode surface during the SOEC operation mode. On Model 2, the energy barrier for CO dissociation on the interface (2.67 eV) and the top (2.91 eV) are lower than that of Model 1. The adsorption of CO at the Ni/SDC interface is stronger (-2.19 eV) than the Ni cluster site. This indicates that both CO adsorption and decomposition are more favorable at interface oxygen vacancy site of Ni/SDC.
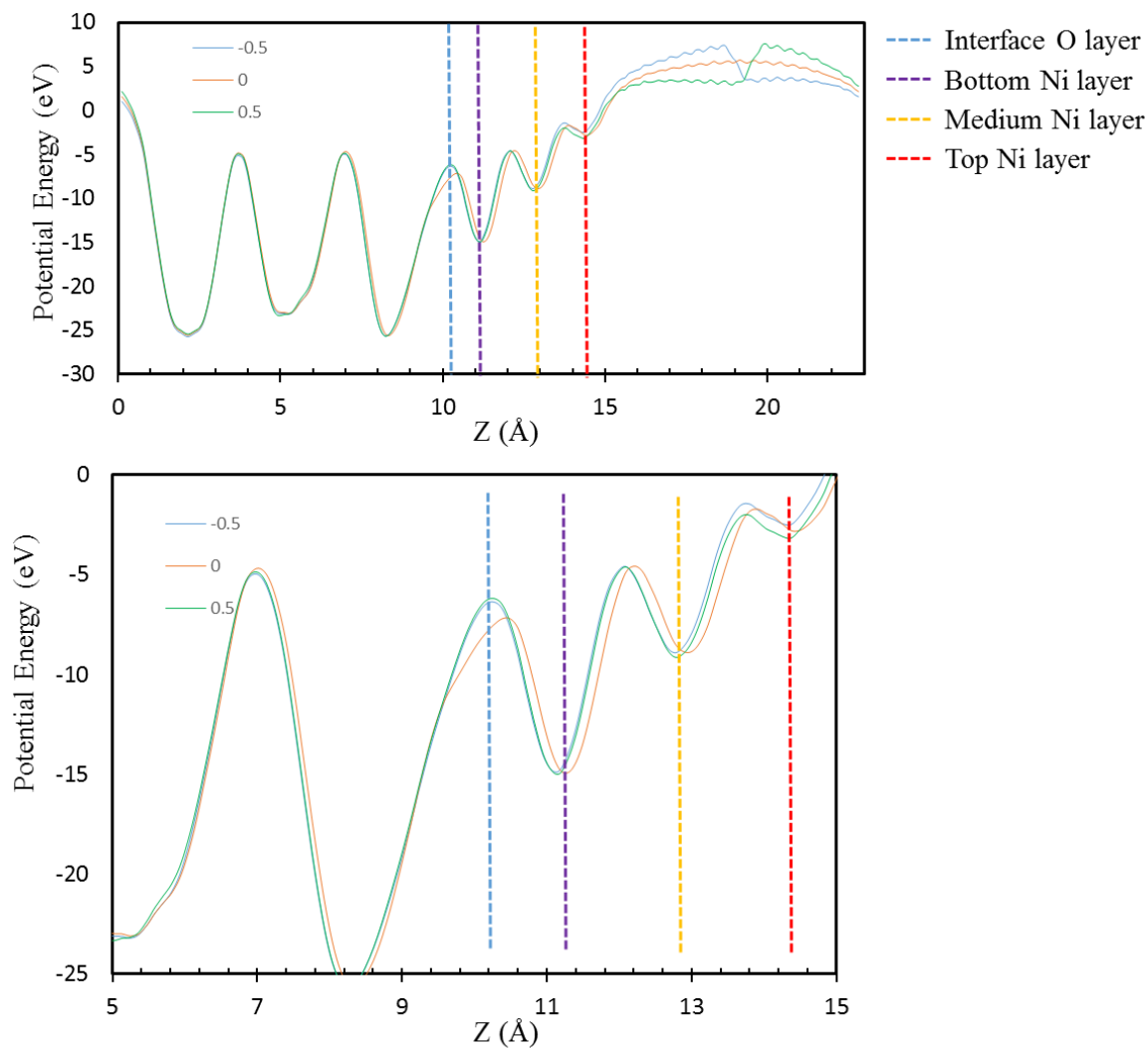
Figure S3-4. The x-y plane average potential energies of the Ni/SDC model at different Z-direction positions as a function of the electric field strength. The green, red and blue solid lines represent the potential energies under a positive electric field (0.5 V/Å), in the absence of a field and a negative electric field (-0.5 V/Å), respectively. The second figure is the enlargement of the first figure in the range of 5-15 Å in order to make the difference of these three lines clear.
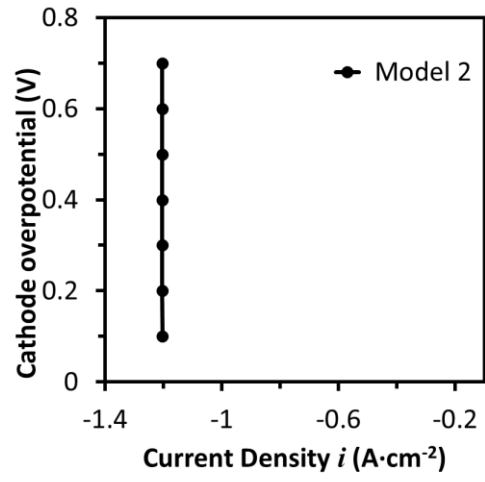
Figure S3-5. Simulated polarization curves of Model 2 (1000 K).

Appendix B: Supporting Information for Chapter 5

Table S5-1. Arrangements of La and Sr within the LaFeO$_3$ lattice considered in this study.
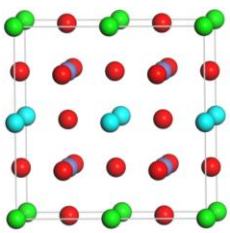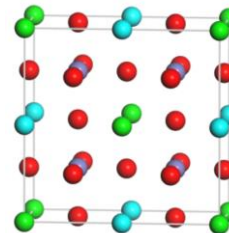
	Sr substitution	
	1	2
Configurations considered in this study		
Gibbs free energy / eV	-141.64	-141.53

Table S5-2. The frequencies of all involved specie (IS: initial state; TS: transition state; FS: final state).

Model	Elementary step	Frequencies (cm^{-1})
	R2IS (R1FS)	[1899 1214 624 522 226 184 132 83 25];
	R2TS	[2163 578 279 254 225 195 160 27];
	R2FS	[2189 434 263 258 242 215 99 39 31];
	R3IS	[2198 269 248 163 57 49];
	R4IS	[457 385 267];
Fe$_4$-3O$_{vac}$-1	R4TS	[640 197];
	R4FS	[431 334 300];
	R5IS	[493 335 242];
	R5TS	[601 440];
	R5FS	[526 327 285];

Ni$_1$Fe$_3$-2O$_{vac}$	R2IS (R1FS)	[1829 1213 664 553 240 219 181 131 66];
	R2TS	[2123 474 433 402 284 194 158 81];
	R2FS	[2196 569 342 330 283 251 203 64 48];
	R3IS	[2196 342 331 251 64 48];
	R4IS	[457 385 267];
	R4TS	[640 197];
	R4FS	[431 334 300];
	R5IS	[536 408 252];
	R5TS	[623 504];
	R5FS	[507 332 292];
Mn$_1$Fe$_3$-2O$_{vac}$	R2IS (R1FS)	[1884 1218 656 469 222 179 168 149 52];
	R2TS	[2013 500 373 359 268 218 87 41];
	R2FS	[2120 440 296 278 259 234 212 51 29];
	R3IS	[2118 266 250 209 45 31];
	R4IS	[457 385 267];
	R4TS	[640 197];
	R4FS	[431 334 300];
	R5IS	[492 392 262];
	R5TS	[560 499];
	R5FS	[440 316 278];
Ni$_1$Mn$_1$Fe$_2$-2O$_{vac}$	R2IS (R1FS)	[1851 1225 685 540 238 222 153 116 57];
	R2TS	[2083 623 390 345 219 161 146 64];
	R2FS	[2160 723 454 401 366 241 196 68 54];
	R3IS	[2160 453 401 367 71 63];
	R4IS	[457 385 267];

R4TS	[640 197];
R4FS	[431 334 300];
R5IS	[429 375 284];
R5TS	[593 521];
R5FS	[539 337 291];

Table S5-3. The most stable structures for cases of 1-5 oxygen vacancies and the possibilities considered in this study.
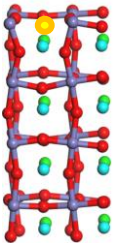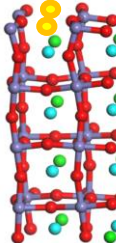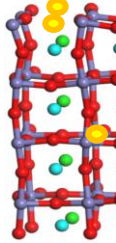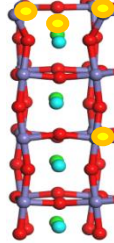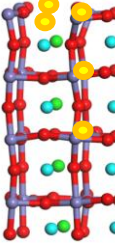
	Oxygen vacancy				
	1	2	3	4	5
Configurations considered in this study					
Gibbs free energy / eV	-554.0392	-548.1569	-541.7768	-535.6326	-528.8474
Possibilities considered	2	14	12	9	10

Table S5-4. Gibbs energy change of creating different oxygen vacancies (3, 4, and 5) for Ni, Mn doped and NiMn co-doped LSF models under typical SOEC conditions: T = 1,073 K and $PO_2 = 10^{-20}$ atm.

Models	ΔG at typical SOEC conditions		
	3 Ovac	4 Ovac	5 Ovac
Ni doped LSF	-3.82	-4.06	-3.79
Mn doped LSF	-1.83	-2.42	-1.96
NiMn co-doped LSF	-3.25	-4.13	-3.61

We can observe that the ΔG for the models with Ni and NiMn dopants are all lower than that of the Mn doped model. This further proves our conclusion that, Ni or NiMn dopants can make the oxygen vacancy easier to form compared with the Mn dopant.

Table S5-5. Different possible locations of Ni/Mn doping cations and their energies.
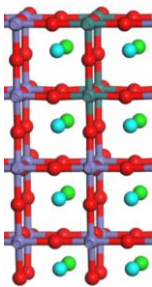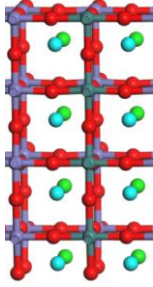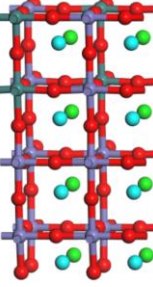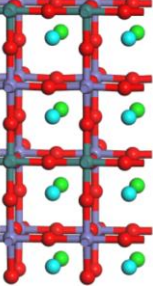
	Ni or Mn substitution			
	1	2	3	4
Configurations considered in this study				
Ni doping Energy / eV	-541.77	-542.82	-541.63	-542.29
Mn doping Energy / eV	-567.11	-567.72	-567.04	-566.94

Table S5-6. CO_2 adsorption energy and reduction reaction energy on the models investigated in this study.

Models	E_{ads} /eV	ΔE /eV
Fe_4-$1O_{vac}$	-1.15	3.31
Fe_4-$2O_{vac}$-1	-0.57	1.75
Fe_4-$2O_{vac}$-2	-1.24	2.97
Fe_4-$3O_{vac}$-1	-0.15	1.30
Fe_4-$3O_{vac}$-2	-2.28	3.42
Fe_4-No O_{vac}	-1.21	5.44
Ni_1Fe_3-$2O_{vac}$	-0.22	1.43
Mn_1Fe_3-$2O_{vac}$	-0.17	1.28
Ni_2Fe_2-$2O_{vac}$	-0.12	2.29
Mn_2Fe_2-$2O_{vac}$	0.22	1.05
$Ni_1Mn_1Fe_2$-$2O_{vac}$	-0.05	0.69
$Ni_1Mn_1Fe_2$-$3O_{vac}$	-1.76	2.84
Ni_1Fe_3-$3O_{vac}$	-2.33	4.27
Mn_1Fe_3-$3O_{vac}$	-1.84	3.49
Ni_2Fe_2-$3O_{vac}$	-2.36	3.23
Mn_2Fe_2-$3O_{vac}$	-1.50	2.46

As shown in Table S5-7, for the models with 2 surface oxygen vacancies and 25% Ni / Mn doping alone, the distance of Fe-Ovac-Ni is 4.121 Å while Mn-Ovac-Fe is 4.153 Å. Doping more Ni / Mn elements (50%) on the surface or creating 3 surface oxygen vacancies give rise to the increase of the distance between the two surface metal cations connected with the oxygen vacancy. This will further cause weak CO_2 binding (physical adsorption). For the models with Ni-Mn co-doping, we also considered other arrangements of Ni and Mn position on surface and the CO_2 adsorption configuration on these models were listed in Table S5-

6. It is found that there are no existences of CO_2 adsorption configuration 3 (most favorable for CO_2 reduction reaction) also due to the increase of the distance between the two surface metal cations connected with the oxygen vacancy.

Table S5-7. Other possible CO_2 configurations on LSF models with Ni, Mn and Ni-Mn co-doping with 3 surface oxygen vacancies and 2 surface oxygen vacancies respectively.

	Other CO2 adsorption configurations	
	3 oxygen vacancies on surface	2 oxygen vacancies on surface
Ni doping		
Mn doping		
Ni and Mn co-doping		

As shown in Table S5-8 and Table S5-9, because of lower adsorption energy (stronger binding), Mn prefers to bind with O of CO_2 while Ni is more likely to bind with C of CO_2 during CO_2 adsorption process.

Table S5-8. Different CO_2 adsorption configurations and the corresponding adsorption energies on Ni_1Fe_3-2Ovac model.
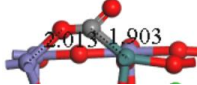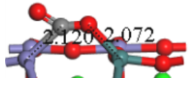
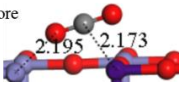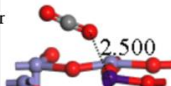|	CO₂ adsorption on Ni₁Fe₃-2Ovac	
	1 putting C of CO_2 close to Ni	2 putting O of CO_2 close to Ni
Configurations considered in this study		
CO_2 adsorption energy(eV)	-0.22	0.17

Table S5-9. Different CO_2 adsorption configurations and the corresponding adsorption energies on Mn_1Fe_3-2Ovac model.
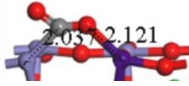
	CO₂ adsorption on Mn₁Fe₃-2Ovac	
	1 putting C of CO_2 close to Mn	2 putting O of CO_2 close to Mn
Configurations considered in this study		
CO_2 adsorption energy(eV)	0.096	-0.167

Table S5-10. Forward rate (s^{-1}) of every elementary step and overall rates (s^{-1}) calculated in the microkinetic models for the selected models of pure LSF, Ni doping, Mn doping and Ni-Mn co-doping.

Reactions	Forward rate (s^{-1}) of every step and overall rates (s^{-1})			
	Fe_4-$3O_{vac}$-1	Ni_1Fe_3-$2O_{vac}$	Mn_1Fe_3-$2O_{vac}$	$Ni_1Mn_1Fe_2$-$2O_{vac}$
R1	3.73×10^8	3.73×10^8	3.73×10^8	3.73×10^8
R2	1.95×10^1	3.96×10^0	2.22×10^2	1.47×10^2
R3	9.36×10^6	9.36×10^6	9.37×10^6	9.36×10^6
R4	1.86×10^8	1.86×10^8	1.86×10^8	1.86×10^8
R5	3.86×10^6	1.17×10^6	2.42×10^7	1.97×10^5
$R_{overall}$	1.95×10^1	3.96×10^0	2.22×10^2	1.47×10^2
R2(0.3V)	5.01×10^2	1.01×10^2	5.70×10^3	3.76×10^3
R3(0.3V)	9.36×10^6	9.36×10^6	9.37×10^6	9.36×10^6
$R_{overall}$(0.3V)	5.01×10^2	1.01×10^2	5.70×10^3	3.76×10^3

The sensitivity analysis of current density as shown in Figure S5-3 was conducted through changing the energy barriers of CO_2 reduction reaction by -5%-5% on LSF model with Mn doping. The reaction energy was kept as constant during these calculations. The current density would change by almost 1 order of magnitude when changing the energy barrier of CO_2 reduction by ± 5%, which proves that it is very sensitive to the absolute value of energy barriers of CO_2 reduction reaction (rate-limiting step).
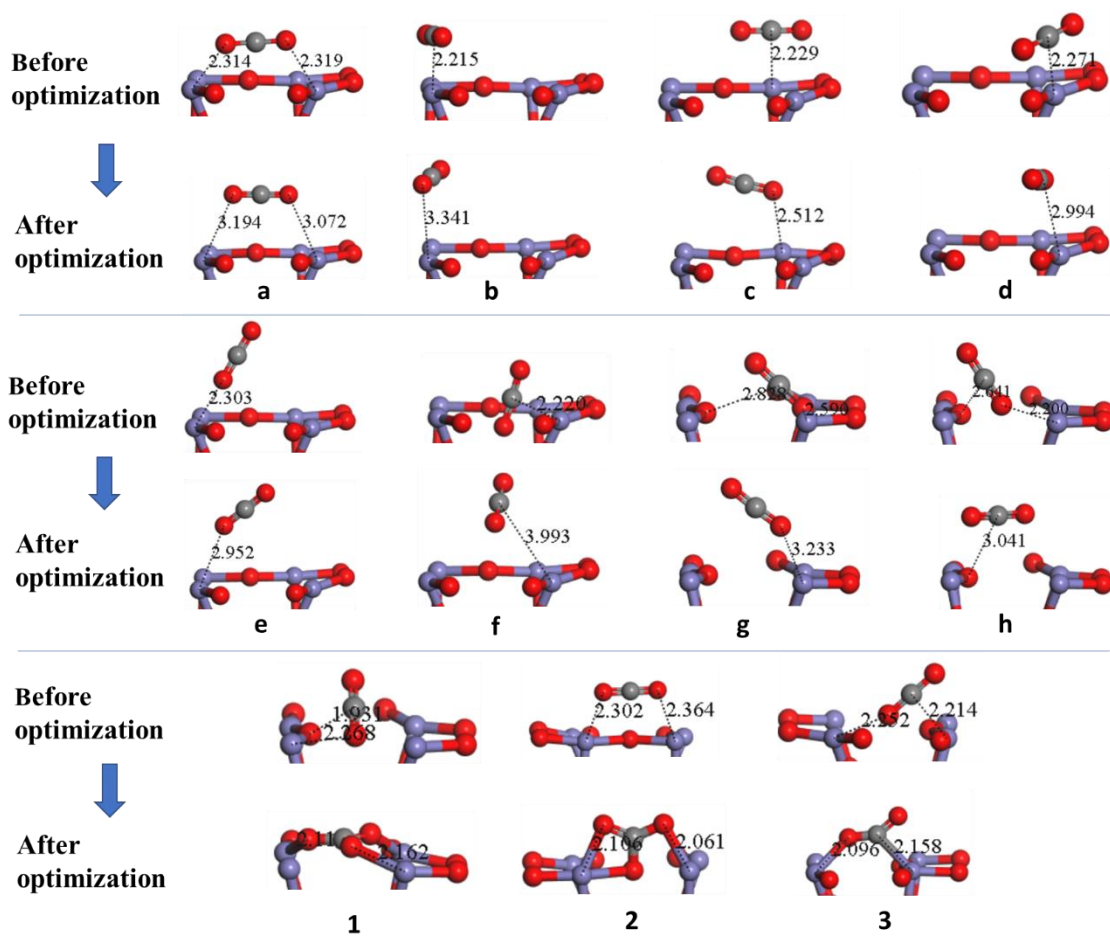
Figure S5-1. Physical adsorption configurations (a-h) and chemical adsorption configurations (1-3) of CO_2 on $La_{0.5}Sr_{0.5}FeO_{2.75}$ (001) surface before and after DFT structural optimization.
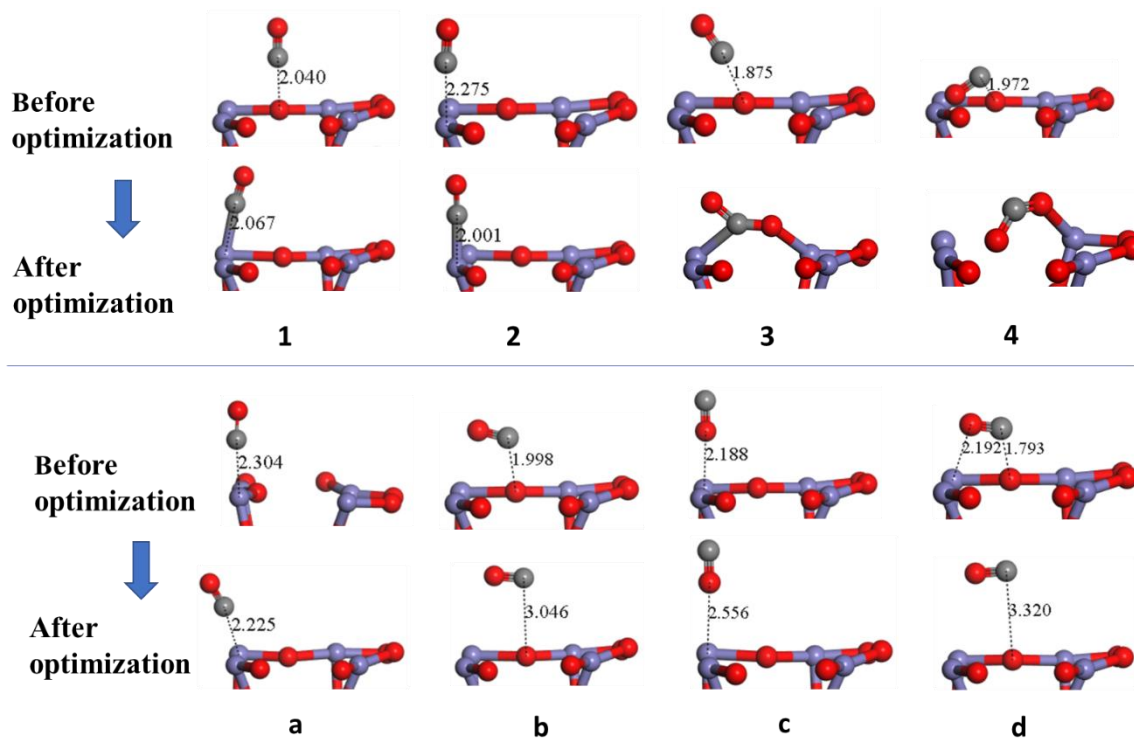
Figure S5-2. Physical (a-d) and chemical (1-4) adsorption configurations of CO on $La_{0.5}Sr_{0.5}FeO_{2.75}$ (001) surface before and after DFT structural optimization.
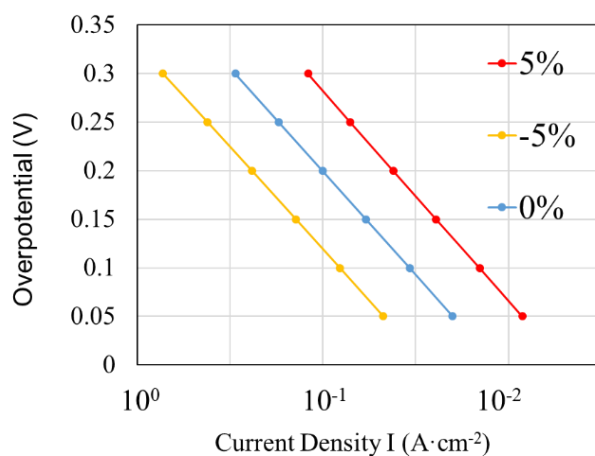

Figure S5-3. Sensitivity analysis of current density based on changing the energy barriers of CO_2 reduction reaction by -5%-5% on LSF model with Mn doping.